

# **An inter-comparison of line-by-line models using different molecular databases.**

*Marco Matricardi<sup>1</sup>, Guido Masiello<sup>2</sup> and Carmine Serio<sup>2</sup>*

*<sup>1</sup>ECMWF, Shinfield Park, Reading, UK*

*<sup>2</sup>DIFA, Università della Basilicata, Potenza, Italy*

## Introduction

A prerequisite for exploiting satellite radiance data for Numerical Weather prediction (NWP) by use of a variational analysis scheme (for example, 1D-Var described by Eyre et al. (1993) for a single profile retrieval or 4D-Var described by Rabier et al. (1998) for a global NWP analysis) is the ability to simulate radiances from an input atmospheric profile. To achieve this, a radiative transfer (RT) model is used. The computation of the radiances from the NWP model profile and surface parameters is commonly referred to as the “forward model”. The variational approach to assimilation of data into a NWP system involves the definition of the observation-error covariance matrix that is used to specify errors associated with radiance data. The observation-error covariance matrix is the sum of the instrumental-error covariance matrix and the forward-model-error covariance matrix, the latter being based on the estimate of errors associated with RT models. For radiance assimilation in NWP, fast RT models are used that are generated from accurate transmittances computed using line-by-line models. In principle fast RT models should not add significantly to the errors generated by uncertainties in the spectroscopic data used by the line-by-line model so that these errors make most of the contribution to the forward-model-error matrix.

The Infrared Atmospheric Sounding Interferometer (IASI) (Cayla 2003) on the METOP-A (Klaes et al. 2000) operational meteorological polar orbiter will provide high spectral resolution allowing improved extraction of temperature, moisture, and some minor constituents. NWP centers are not expected to use the thousands of IASI channels. This means that a subset, or appropriate combination, of channels should be defined for assimilation purposes so that the information content present in the whole spectrum is not significantly degraded. RT errors are an important consideration in channel selection. In fact guidance is needed priori to the channel selection as to which procedure to adopt for the retrieval to minimize the effects of system errors, and of forward model errors in particular.

The fast RT model, RTTOV (Matricardi et al. 2004), used operationally at ECMWF is based on accurate transmittances generated by the GENLN2 (Edwards 1992) line-by-line model. GENLN2 was adopted for use at ECMWF more than ten years ago and since then no major new versions of the code have been released. The long term maintenance of GENLN2 has now become an issue and it is apparent that there is no commitment to further develop the code. Consequently we have considered the possibility of a different choice of line-by-line model for the training of RTTOV. This choice would be mainly based on accuracy, computational efficiency and long term commitment to the maintenance of the code, with portability and user friendliness and also playing a role, albeit minor, in the choice. To this end we have compared the GENLN2 model with the LBLRTM (Clough et al. 1992) and the RFM (<http://www.atm.ox.ac.uk/RFM/>) line-by-line models with the objective to quantify differences between the forward models and to assess the quality of the spectroscopic data used in the forward model computations by using molecular parameters from different databases. Five test cases have been studied by comparing simulated spectra with spectra measured during the first Convection and Moisture Experiment (CAMEX-1) campaign (Griffin et al. 1994), the third Convection and Moisture Experiment (CAMEX-3) campaign (<http://ghrc.msfc.nasa.gov/camex3/>), the EAQUATE campaign (Cuomo et al. 2005), the MOTH campaign (Taylor et al. 2003) and with spectra measured at the Atmospheric Radiation Measurement (ARM) site (Stokes et al. 1994).

## Line-by-line codes

### GENLN2

GENLN2 is a general-purpose line-by-line atmospheric transmittance and radiance model. The line-by-line calculation involves calculating transmittances in several atmospheric layers for each of the gases that are spectroscopically active over the spectral range of interest in wave-number space. The atmosphere is subdivided into a number of layers within which the gas is considered homogeneous and is represented by appropriate Curtis-Godson absorber weighted mean parameters. Mean temperature, pressure and gas amount are defined for each gas along the actual ray trajectory within the layer (gas path) and since within a path the gas is considered homogeneous, the line-by-line computation of the absorption coefficient proceeds for each gas path at each point of the wave-number grid. In principle one could choose a wave-number grid fine enough that the narrowest line is adequately sampled to evaluate the absorption coefficient for every line at every wave-number grid point. Given the excessive amount of computer time and storage required by such approach, the GENLN2 algorithm is based on the assumption that a wider wave-number grid can be reasonably used in the wings of lines whereas a fine grid is required over the line center where the line profile is changing rapidly. In the GENLN2 computations performed at ECMWF the wave-number range is divided into a number of  $1 \text{ cm}^{-1}$  constant spacing intervals (wide mesh) as shown in Fig.1.

The line-by-line computation then proceeds in two stages. The first stage involves the computation of the absorption due to the wings of lines whose centers fall within the range  $1 \text{ cm}^{-1}$  to  $25 \text{ cm}^{-1}$  from the wide mesh boundaries. For these lines, absorption is computed at the lower boundary, center, and upper boundary of the wide mesh interval. For the lines whose centers are further than  $25 \text{ cm}^{-1}$  from the wide mesh boundary, the absorption contribution of the line wing is included by means of a continuum for  $\text{H}_2\text{O}$  and  $\text{CO}_2$  as explained below. Once the contributions from all far-off lines wings have been considered, a quadratic interpolation between the three values at the wide mesh points gives the total line wing absorption at intermediate points. The second stage of the computation involves the absorption calculation over a fine grid obtained by dividing the wide mesh interval into 1000 points. All the lines whose centers lie within  $1 \text{ cm}^{-1}$  of the wide mesh boundaries are included. The interpolated absorption due to the wings of the lines further than  $1 \text{ cm}^{-1}$  from the wide mesh boundary are then added to the fine-pass absorption to give the total line absorption at each fine grid point within the wide mesh.

Therefore, there is no spectral integration involved in the GENLN2 calculation of quantities in the fine mesh. These will be truly monochromatic values on the fine mesh of either a spectral function such as the absorption coefficient or a spectral density (by wave number) proportional to a distribution function such as the spectral intensity of a line e.g. the Lorentzian. GENLN2 calculations were not performed for very weak lines. The minimum line strength is determined by considering an Elsasser distribution of lines to represent the extreme case of a tight absorption band of low optical depth. The lines have half width  $0.1 \text{ cm}^{-1}$ , peak separation  $0.01 \text{ cm}^{-1}$  and constant strength  $S$ . For a given path  $j$  the lines are considered not to be significant if the transmission of such a line distribution is greater than 0.99999. This means that for a line to be used,  $S_j u_j$  ( $u_j$  is the gas path amount) must be greater than a minimum value. In the wide mesh calculations we rejected lines for which  $S_j u_j < 10^{-7}$  and in the fine mesh calculations we rejected lines for which  $S_j u_j < 10^{-8}$ . The accuracy of the line-by-line computations should not be affected by the rejection of very weak lines. For this paper we found that the inclusion of all the lines in the GENLN2 computations had no significant impact on the computed spectra (when compared with the baseline spectra differences were never greater than 0.001 K) whereas the

computational time was reduced six-fold. Note that the condition used for  $S_j u_j$  is relevant for lower and middle atmosphere studies only, for other applications different values should be used. Heavy molecules were modelled by using high-resolution cross-sectional data. The line strengths and half-widths are adjusted to the path pressure and temperature and Doppler broadening of the spectral lines is taken into account. The Voigt (Armstrong 1967) line shape was adopted for most cases to describe the effects of both pressure and Doppler line broadening. For some gases the Voigt line shape is not adequate and effects such as line mixing and non-Lorentzian line wing effects must be considered. In GENLN2 there is a CO<sub>2</sub> line shape option that includes the effects of line mixing and sub-Lorentzian line wings. If data is available, CO<sub>2</sub> Q-branch line mixing can be included out to an arbitrary 10 cm<sup>-1</sup> from line center. At greater distances from line center, a sub-Lorentzian line shape is used (Cousin et al. 1985). If no line-mixing data is available then the sub-Lorentzian line shape is used everywhere. CO<sub>2</sub> line mixing was fully accounted for in the computations by using line mixing coefficients from Strow et. al (1994). Note that since the line mixing coefficients depend on the line strengths and widths, they must be used in conjunction with the lines for which mixing coefficients have been calculated. The water vapor continuum is computed using the semi-empirical approach of Clough et al. (1989), (CKD version 2.1 ) and in addition to H<sub>2</sub>O, a CO<sub>2</sub> continuum type absorption is also included. The CO<sub>2</sub> continuum is computed using the GENLN2 line shape and is stored in the code at temperatures of 230K, 250K and 296K. For a given wave number, the continuum at a particular path temperature is obtained by interpolation between these values. Finally the pressure-broadened band of N<sub>2</sub> at 2350 cm<sup>-1</sup> (Menoux et al. 1993) and that of O<sub>2</sub> at 1550 cm<sup>-1</sup> (Timofeyev et al. 1978, Rinsland et al. 1989 ) are also included as broadband continuum contributions to the absorption.

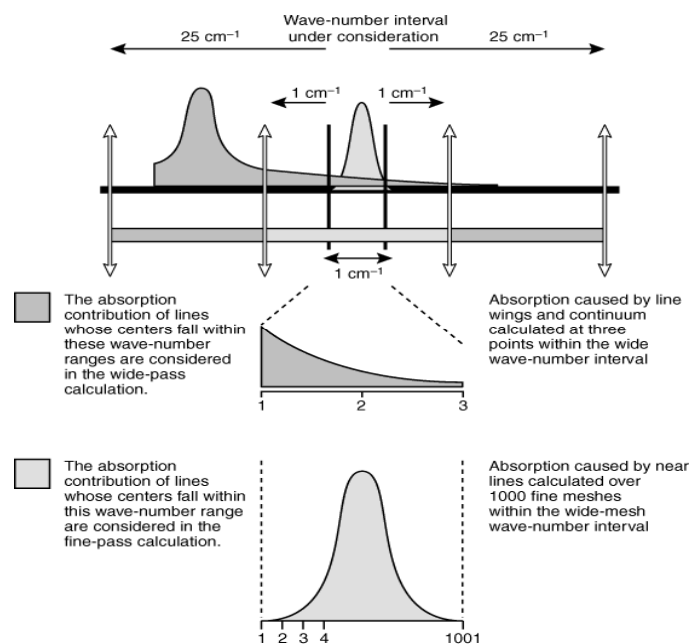


Fig 1 :The spectral calculation scheme for GENLN2.

## RFM

The Reference Forward Model (RFM) is based on GENLN2 and was developed at Oxford University to be used to perform radiance computation for the MIPAS. RFM shares many features in common with GENLN2: the line-by-line computations proceed in the wide mesh/fine mesh stages described in the

previous section; the effects of pressure and velocity line broadening are described by the Voigt line shape and a sub-Lorentzian line shape can be optionally used in the wings of the CO<sub>2</sub> lines using the same scheme utilized in GENLN2; line coupling for the CO<sub>2</sub> Q branches in the u2 and u3 regions is treated using the same first order coupling parameters from Strow et al. (1994). However, significant differences exist in the treatment of water vapour, oxygen and nitrogen continua. For water vapour RFM incorporates the self- and foreign-broadened water vapor continuum model MT\_CKD\_1.1 (Mlawer et. al. 2004), whereas for the collision induced bands of oxygen at 1600 cm<sup>-1</sup> and nitrogen at 2350 cm<sup>-1</sup> it incorporates the models by Thibault et al. (1997) and Lafferty et al. (1996) respectively. In RFM computations can be performed for atmospheric layers which are not in local thermodynamical equilibrium using user-supplied vibrational temperatures. Radiance calculations for down looking scenes are performed assuming a specular surface (for flux calculations the reflection is treated as diffuse) and, as in GENLN2, there is no solar term.

It should be noted that GENLN2 and RFM have been designed to use a constant value of the surface emissivity. Since realistic values of the surface emissivity are wavenumber dependent, we have re-designed the codes to perform radiance computations for variable emissivities. A feature of RFM that is absent in GENLN2 is the capability of performing the computation of Jacobians for pressure, temperature, humidity, surface temperature and emissivity. Temperature dependent cross section data can be used by RFM to model the absorption due to heavy molecules. For the data tabulated as a function of pressure ( $p$ ) and temperature ( $T$ ) instead of just temperature (e.g. as supplied with HITRAN96), the RFM interpolates a value from the 3 surrounding ( $p, T$ ) points using a fairly sophisticated triangulation scheme. Points outside the boundary of the tabulated ( $p, T$ ) space are assigned a value at the closest boundary point. The RFM then applies the GENLN2 heavy-molecule partition function temperature correction.

## LBLRTM

The LBLRTM line-by-line model has been developed at AER and is derived from the Fast Atmospheric Signature Code (FASCODE) (Clough et al. 1981). To describe the effects of pressure and Doppler line broadening the Voigt line shape is used at all atmospheric levels with an algorithm based on a linear combination of approximating functions. LBLRTM incorporates the self- and foreign-broadened water vapor continuum model MT\_CKD\_1.3 (Mlawer et. al. 2004) as well as continua for carbon dioxide and for the collision induced bands of oxygen at 1600 cm<sup>-1</sup> (Thibault et. al 1996) and nitrogen at 2350 cm<sup>-1</sup> (Lafferty et al. 1996).

The effects of line coupling for the CO<sub>2</sub> Q branches in the u2 region (600-800 cm<sup>-1</sup>) are treated using first and second order coupling parameters from Hoke et al. (1989). These line coupling parameters have been updated to be consistent with the HITRAN2000 line parameters. They may be used in conjunction with other line files but it should be noted that the required constraints on the line coupled bands have not been checked. For the 1932, 2076, 2093 and 2193 cm<sup>-1</sup> CO<sub>2</sub> Q branches of the u3 region line coupling is treated using first order coupling parameters from Strow et al. (1994). Also available for the LBLRTM calculations are additional first order coupling parameters for the 618, 667, 720 and 740 cm<sup>-1</sup> CO<sub>2</sub> P/R branches in the u2 region (Niro et. al 2005). It should be noted that the use of the line parameters for the P/R branches has to be accompanied by a change in the line shape for carbon dioxide. So far the P-R line coupling file has only been tested with the TES spectroscopic line parameter database and its use with other line files (e.g. HITRAN2000 (Rothman et al. 2003), HITRAN2004 (Rothman et al. 2005), GEISA2003 (Husson et al. 2004)) may create difficulties.

LBLRTM can use temperature dependent cross section data to model the absorption due to heavy molecules. The pressure dependence of the cross sections is treated by performing a convolution of the cross section spectrum with an appropriate Lorentz function. LBLRTM has the capability to perform radiative transfer calculations for down looking scenes with a Lambertian surface by obtaining the downwelling flux from a radiance calculation at the diffusivity angle of 53.21 degrees. An algorithm (linear in tau) is used for the treatment of the variations of the Planck function within a vertically inhomogeneous atmosphere. Finally, computations can be performed for atmospheric layers which are not in local thermodynamical equilibrium, a solar term can be included and a recently added feature is the capability of performing the computation of analytic derivatives/jacobians.

As discussed previously, the Voigt line shape incorporates the effects of both Doppler (velocity) and collisional line broadening; collisional broadening dominates from the surface to a certain altitude and velocity broadening dominates above that altitude with an intervening transition region. As a consequence, for a given temperature profile, one could devise an optimal sampling of the spectrum that is dependent on wave number and layer pressure, i.e. a sampling interval larger at the surface and smaller at the top of the atmosphere. In LBLRTM a spectral sampling is used that is optimal for the atmospheric layer and the spectral regime under consideration. To achieve a monochromatic accuracy of better than 0.5% this sampling interval has been chosen to be 1/4 of the line halfwidth based on an analysis of the errors in the reconstruction of the Lorentz line as a function of the sampling interval using the four point interpolation scheme utilized in LBLRTM. The sampling interval  $DV$  is defined as

$$DV = \bar{\alpha}_v / SAMPLE \quad (1)$$

where  $\bar{\alpha}_v$  is the average value of the Voigt halfwidth for the layer and  $SAMPLE$  is set by default to 4 as stated previously. The average value of the Voigt halfwidth  $\bar{\alpha}_v$  can be written as:

$$\bar{\alpha}_v = \frac{\bar{\alpha}_L}{2} + \left[ \left( \frac{\bar{\alpha}_L}{2} \right)^2 + \bar{\alpha}_D^2 \right]^{1/2} \quad (2)$$

where  $\bar{\alpha}_L$  and  $\bar{\alpha}_D$  are the average layer values of the Lorentz and Doppler halfwidths respectively. The mean Doppler halfwidth can be written in the form

$$\bar{\alpha}_D = \frac{\bar{\nu}}{c} + \left[ 2 \ln 2 \frac{kT}{\bar{M} / N_o} \right]^{1/2} \quad (3)$$

where  $\bar{\nu}$  is the average of the beginning and ending wavenumber values for the problem,  $N_o$  is the Avogadro's number and  $\bar{M}$  is a representative gram molecular weight for the constituents in the path. Since the sampling interval is based on the average of the beginning and ending frequencies, the accuracy of the code depends on the spectral domain used in the calculations. For this reason LBLRTM has been structured in such a way as that the maximum value of  $\bar{\nu}$  is set so 2000  $\text{cm}^{-1}$ , a trade off value with respect to core size, disk space and computational time. The implication of this choice is that is not possible to perform a single run computation that covers the whole near infrared spectrum (e.g. 600 to 3000  $\text{cm}^{-1}$ ). Our approach is to perform multiple runs using a shell script with appropriate naming conventions. It should be stressed that the optimal sampling used in LBLRTM makes the code more computationally efficient than GENLN2 and RFM where the spectral sampling is

defined by the fixed fine mesh grid interval (although a wide mesh interval boundary wavenumber grid can be supplied by the user that covers the total spectral range of interest).

Details of the water vapour continua models and the CO<sub>2</sub> line mixing schemes used by the various codes are given in Table 1.

Table 1 : Details of line-by-line models

Model	Water vapour Continuum	Line mixing CO <sub>2</sub> u2 (600-800 cm <sup>-1</sup> )	Line mixing CO <sub>2</sub> u3 (2150-2450 cm <sup>-1</sup> )
GENLN2	CKD_2.1	Q branch: 1 <sup>st</sup> order	Q branch: 1 <sup>st</sup> order
LBLRTM	MT_CKD_v1.3	P branch : 1 <sup>st</sup> order Q branch: 1 <sup>st</sup> and 2 <sup>nd</sup> order R branch: 1 <sup>st</sup> order	Q branch: 1 <sup>st</sup> order
RFM	MT_CKD_v1.1	Q: 1 <sup>st</sup> order	Q branch: 1 <sup>st</sup> order

Note that although the naming of the water continua models used in RFM and LBLRTM is different, in the spectral regions of interest to us they are identical.

For the water vapour continuum model adopted in GENLN2, RFM and LBLRTM (Clough et al. 1989) the total continuum contribution to the absorption coefficient,  $k_c(\nu)$ , at wavenumber  $\nu$  can be written in the form

$$k_c(\nu) = \nu \tanh\left(\frac{h\nu}{2kT}\right) \left(\frac{T_o}{T}\right) \left(\frac{p_s}{p_o} C_s^o(\nu, T) + \frac{(p - p_s)}{p_o} C_f^o(\nu, T)\right) \quad (4)$$

where  $T$  is temperature,  $p$  is pressure,  $p_s$  is water vapour partial pressure,  $T_o$  and  $p_o$  are reference temperature (296K) and pressure (1013 hPa) values and  $h$ ,  $c$  and  $k$  are the Planck constant, speed of light and Boltzmann constant respectively.  $C_s^o$  and  $C_f^o$  are the self-broadening coefficients and the foreign-broadening coefficients defined at the reference temperature and pressure. To illustrate the differences between the models used in GENLN2 and RFM/LBLRTM we have plotted  $C_s^o$  in Figure 2 and  $C_f^o$  in Figure 3. Water vapour continuum plays an essential role in the absorption process. In the 10  $\mu\text{m}$  window region between the water vapor 6.3  $\mu\text{m}$  band and the water vapor rotation band the continuum absorption is stronger than the line absorption. The dominant source of continuum in this region is the self broadening (H<sub>2</sub>O-H<sub>2</sub>O collisions) continuum whereas the dominant source of continuum in the 6.3  $\mu\text{m}$  water vapor band is the foreign broadening (H<sub>2</sub>O-N<sub>2</sub> collisions) continuum. The foreign broadening continuum is particularly important between 1350 and 2100 cm<sup>-1</sup>. From Figure 2 it can be seen that in the window region, self broadening coefficients for CKD\_2.1 are larger than MT\_CKD\_v2.1 coefficients. Figure 3 shows that foreign broadening coefficients for CKD-2.1 are smaller than CKD.2.4 coefficients between 1400 and about 1900 cm<sup>-1</sup> and larger between 1900 and 2200 cm<sup>-1</sup>.

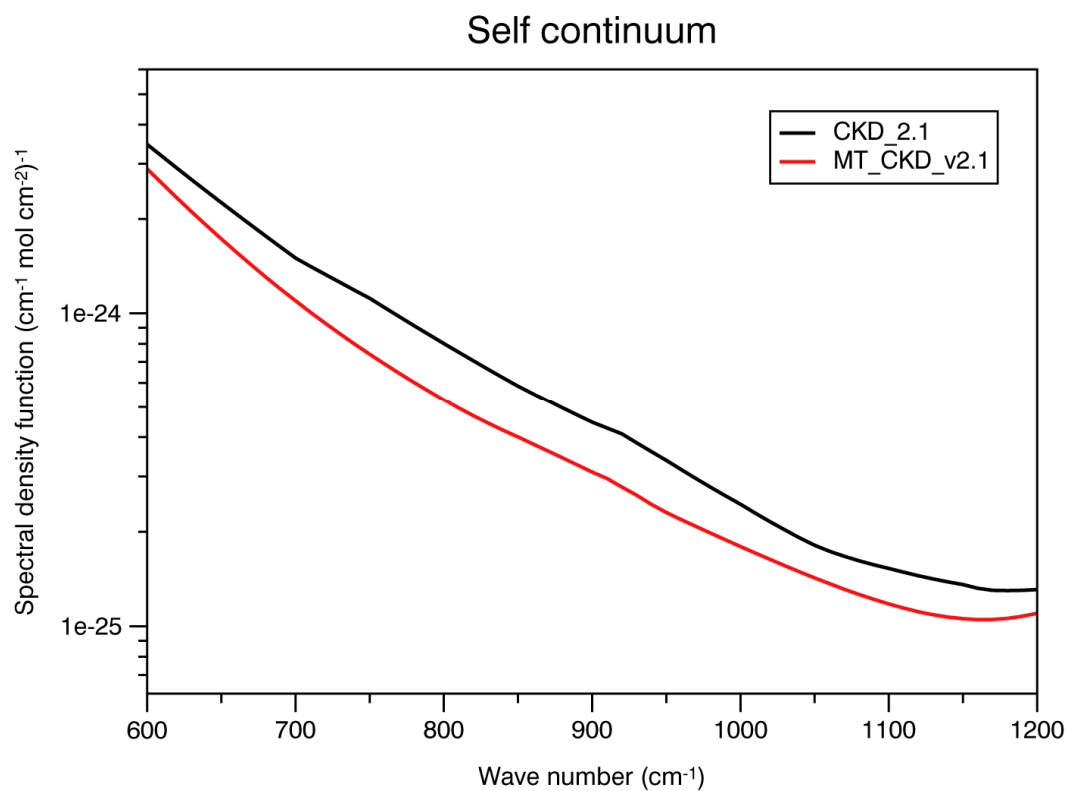


Figure 2: Spectral density function for the water vapor self broadening coefficients at 296K and 1013hPa.

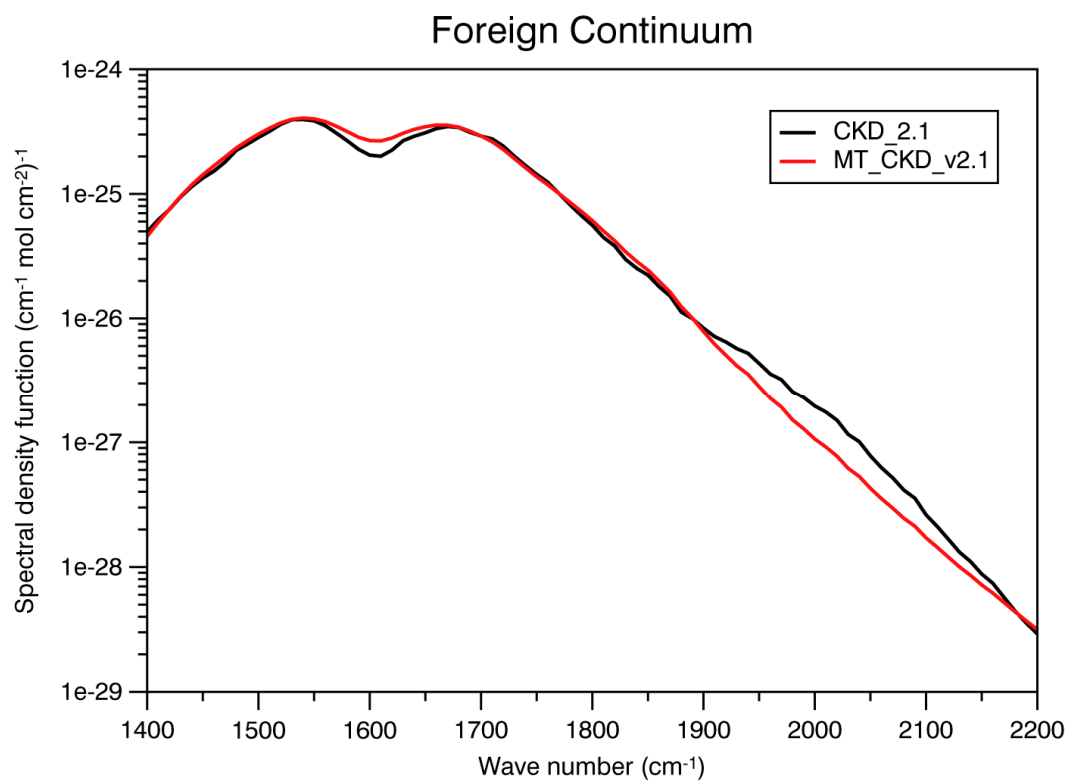


Figure 3: Spectral density function for the water vapor foreign broadening coefficients at 296K and 1013hPa

## Measurements

### The CAMEX-1 case

The data used for this case study belongs to the first Convection and Moisture Experiment CAMEX-1 field campaign and consists of the up-welling radiance spectrum measured by the HIS (Smith et al. 1983) during the third northbound pass of the ER-2 aircraft along the Virginia/Maryland coast on 29 Sept 1993, from an altitude of approximately 20 km. The distribution files contain the mean and an estimate of uncertainty around the mean for each wave-number sample of the calibrated radiance obtained during the period 03:47:40 UT to 03:54:59 UT. Details of the methodology used to process the HIS data and the in-situ observations were also provided. Some of the information is reported here for convenience.

The HIS data is nadir viewing with a sample time of 6 seconds, without motion compensation, yielding a 2x3 km footprint for every 6 second sample. The spectrum is recorded simultaneously as three independent bands, and is provided as unapodised radiances with the finite field-of-view effect removed. Only data within the optical filter band-pass is included in the data set. Each calibration cycle contains 12 earth views, 4 hot blackbody views, and 4 cold blackbody views in a repeating sequence. The 12 earth views overlap along the flight track to give a continuous strip 2km wide and 12km long. The data provided contain an average of data from four consecutive calibration cycles. This sample average views a strip of ocean about 2km wide and 48 km long. The actual linear distance along the flight track is more than 48 km since no earth data is collected during views of the calibration blackbodies at the end of each calibration cycle. Basic information on HIS quantities referred to in the text are provided in Table 2.

Table 2 : HIS Parameters

Band	Band 1		Band 2		Band 3	
Free Spectral Range (cm <sup>-1</sup> )	564.2500	1128.5000	987.4375	1974.8750	1974.8750	2962.3125
Optical Filter Range (cm <sup>-1</sup> )	600	1080	1080	1800	2050	2600
Spectral Spacing (cm <sup>-1</sup> )	.2755127		.4821472		.4821472	
Maximum Delay (cm)	1.550731		.683588		.518514	
Unapodised Resolution (cm <sup>-1</sup> )	0.322429		.731435		.964294	

The estimate of the uncertainty of the averaged radiances is computed as the standard deviation of the 48 earth views around their mean divided by the square root of the number of samples. The standard deviation is spectrally highly variable and is likely to contain both signal variability due to random instrument noise and that caused by the changing atmospheric conditions during the flight. As there is no independent information on instrument noise, it is not possible to separate the various contributions. There are large spectral regions where the S/N is particularly low since the averaged signal is low or the atmospheric signal variability is large and this is valuable information to interpret correctly the differences with the simulated data.

The in-situ data, called the CAMEX Validation Atmosphere for 29 Sept 1993 04:00 UT, contains altitude, pressure, temperature, relative humidity and ozone concentration from 1003 hPa to 5 hPa, obtained from blending of measurements from different radiosondes. A special surface level at 1018

hPa is included, designed to represent the ocean environment consistent with the HIS aircraft data. The sea surface (skin) temperature was set to 293K which is close to the temperature at the peak of the inversion layer in the Wallops 4:00 UT radiosonde observation and to the temperature obtained by comparing line-by-line FASCODE (Clough et al. 1981) simulations with HIS data (Knuteson, CIMSS, personal communication). There are no direct measurements of the near surface air temperature offshore. The dataset contains also estimates of extreme relative humidity values, obtained primarily from comparing the sonde profile to the lidar profiles (Griffin et al. 1994).

## The CAMEX-III case

The CAMEX-III (<http://ghrc.msfc.nasa.gov/camex3/>) is the third in the series of CAMEX field experiments and was carried out during August-September 1998. It was devoted to the study of hurricane tracking and intensification using NASA-funded remote sensing instruments installed on the NASA ER-2 and DC-8 aircraft platforms. Data used in this paper are from the NAST-I interferometer (Cousin and Gazarick 1999) flown on the ER-2 aircraft. The NAST-I is a high resolution Michelson interferometer that derives his heritage from the non-scanning HIS. It scans the earth beneath the ER-2 with a spatial resolution of approximately 2.5 km with 13 Earth view observations in the cross-track direction. The spectral response and resolution of the NAST-I data used in this paper is that of an ideal Michelson interferometer with maximum optical path difference of 2.00372 cm yielding a resolution of  $0.249536 \text{ cm}^{-1}$ . The data are re-sampled (and slightly oversampled) into a wavenumber grid of  $\approx 0.2410736 \text{ cm}^{-1}$ . Self-apodization effects due to the finite field-of-view of the interferometer are removed. Data within appropriate spectral regions are then extracted for each of the three spectral bands shown in Table 2.

Table 3 : NAST-I Parameters

Band	Band 1		Band 2		Band 3	
Spectral Range ( $\text{cm}^{-1}$ )	645.113	1300.110	1289.985	1999.947	1984.759	2700.024
Spectral Spacing ( $\text{cm}^{-1}$ )	0.2410736		0.2410736		0.2410736	
Maximum Delay (cm)	2.00372		2.00372		2.00372	
Unapodised Resolution ( $\text{cm}^{-1}$ )	0.249536		0.249536		0.249536	

The spectrum used in this paper was recorded during a flight along the east coast of Andros island, The Bahamas, on the 14 September 1998 at 00:30:13 UTC. The in-situ data, contains altitude, pressure, temperature and relative humidity from 1011.8 hPa to 22.75 hPa, obtained from radiosondes. In addition to temperature and water profiles from collocated radiosondes, temperature and water vapor profiles obtained from the inversion of NAST-I spectra were available (Masiello, University of Basilicata, personal communication). They were derived using the inversion scheme incorporated in the  $\delta$ -IASI package that utilizes a scheme based on a data constrained optimization which generalizes the standard Statistical Regularization estimator to the class of ridge regression estimator as described in Carissimo et al. (2005). Since the use of the retrieved profiles resulted in a better agreement with observations they were used to specify the atmospheric state in our simulations alongside with the retrieved value of the skin temperature.

## **The EAQUATE case**

The Italian campaign of the European AQUA Thermodynamic Experiment (EAQUATE) (Cuomo et al. 2005) was carried out during the period 6-10 September 2004. The main objective of the campaign was the validation of products from the AQUA polar orbiter, mainly AIRS radiances. During the campaign the characterization of semitransparent clouds and the study of radiative balance were also performed to demonstrate the role played by ground-based and airborne systems in validation studies. The Italian phase of the campaign was the result of cooperation between the NASA Langley Research Center, the University of Wisconsin, the Istituto di Metodologie per l'Analisi Ambientale (CNR-IMAA), the Mediterranean Agency for Remote Sensing (MARS) and the Universities of Basilicata, Bologna and Napoli. During the campaign four flights of the Scaled Composites Proteus aircraft were successfully completed with two different AQUA overpasses. The suite of microwave and thermal infrared instrumentation installed on the Proteus aircraft included the NAST-I interferometer, the NAST-MTS microwave spectrometer, the Scanning HIS interferometer and the FIRSC far-infrared interferometer. The campaign involved the use of an Earth Observing System-Direct Readout Station and several ground based instruments including four LIDAR systems, a microwave radiometer, two infrared spectrometers, and a ceilometer. The spectrum used in this paper was recorded by NAST-I during a flight in clear sky at a cruise altitude of 15-16 km over the ground station of Tito Scalo in southern Italy. During the NAST-I overpasses, atmospheric temperature and humidity profiles were recorded by several Vaisala RS90 and RS92 sondes with a time sampling rate of approximately 2 hours. In addition, a microwave radiometer was operated continuously with a time sampling rate of 5 minutes. Finally, a Ceilometer (Vaisala CT25K) was used to detect the presence of clouds with a time sampling rate of 20 seconds. The spectrum was recorded at a viewing angle of  $7.5^\circ$  over a deciduous and conifer plant canopy. The spectral emissivity of this kind surface is difficult to model and can be significantly modified by variations in temperature, soil moisture and vegetation cover (the emissivity can change on time scales from seasonal to a few hours). However, a realistic characterization of the spectral emissivity was made possible by the availability of the results obtained by Masiello et al. (2006) that have fitted the surface emissivity to the NAST-I spectra under consideration. As for the CAMEX-III case, to specify the atmospheric state in our simulation we have used profiles of temperature and humidity retrieved from NAST-I spectra.

## **The MOTH case**

In the period April-December 1999 the Met Office carried out two campaigns named Measurement of Tropospheric Humidity (MOTH) (Taylor et. al 2003) with the main objective to assess the spectroscopy in the spectral range used by IASI. Measurements were made using the Microwave Airborne Radiometer Scanning System (MARSS) and the Airborne Research Interferometer Evaluation System (ARIES) installed on the Meteorological Research Flight (MRF) C130 Aircraft. The ARIES instrument is a modified Bomem instrument that can measure thermal radiation between 600 and  $3000\text{ cm}^{-1}$  with a maximum optical path difference of 1 cm. Spectra can be recorded at a range of angles between nadir and 60 degrees off nadir across track. In this study we used an ARIES spectrum measured during the MOTH-Tropic campaign flown during the spring of 1999 based on Ascension Island in the tropical South Atlantic (MOTH-Tropic). Measurements were made looking at nadir in clear sky conditions over ocean on 28 April 1999 during flight A670 at an altitude of ~8km. Since the flight was made during daytime, not only the thermal emission of the atmosphere was measured but also the surface reflection of solar radiation.

The impact of the instrument noise on the measurements can be reduced by averaging the ARIES spectra. However, it should be kept in mind that during the measurements the scene variability can introduce variability in the radiance and consequently the averaging of the spectra has to be balanced against the variability in the radiance resulting from the changing scene. The ARIES data used in this study are produced from 10 co-added interferograms measured during a time interval of 3 seconds (or, alternatively, 300 m of horizontal flight). Since the instrument noise is inversely proportional to the square root of the number of interferograms that have been co-averaged, the laboratory derived noise has been scaled by  $\sqrt{10}$  and used as a guide to the fundamental accuracy limit of the instrument. To record the radiance spectrum ARIES uses two detectors that intersect in the region of  $1750\text{ cm}^{-1}$ . As a result the noise tends to increase towards the edge of the detectors' sensitivity ranges. Another thing to note is that the strong water vapour lines in the band between  $1200$  and  $2100\text{ cm}^{-1}$  cause particular problems in the calibration of the interferometer. Because the instrument was operating in a relatively moist atmosphere, a considerable absorption can occur in the path between the external calibration target and the interferometer. This effect cannot be corrected during the calibration process and since this absorption can change with time the result is that spikes can be observed in the radiance spectra.

The in-situ profile is the results of an analysis that combines the closest dropsonde measurements, with quality control using microwave sounder data recorded looking at the zenith during a low level flight. Additionally, the profile has been checked by analyzing some infrared frequencies. The temperature of the sea surface was measured with an Heinman broadband infrared radiometer and was estimated to be  $301.4\text{ K}$ . Profiles of carbon monoxide and ozone were measured using aircraft core chemistry instrumentation. Since the ARIES spectral response function is not an ideal sinc function (the optical path inside the instrument makes the line shape slightly asymmetric), an apodisation has been applied in order to compare line-by-line and measured spectra. To this end the line-by-line spectra have been firstly degraded to the ARIES resolution using Fourier transform techniques and then a Barcilon-Temes apodising function has been applied to the spectra. This apodisation is also applied to the ARIES data for a direct comparison. The simulated spectrum has also been applied a modulation transfer function (MTF) to reproduce the slight self-apodisation that results from non-parallel rays inside the interferometer, although this is a relatively minor effect.

## **The ARM case**

The data used for this study belongs to the Department of Energy (DOE) Atmospheric Radiation Measurement (ARM) Program (Stokes and Schwartz 1994) and were measured at the Cloud and Radiation Testbed (CART) Southern Great Plains (SGP) Central Facility. The case belongs to a Water Vapor Intensive Observing Period (WVIOP) and contains the averaged radiances from two coincident observations of the down-welling atmospheric infrared spectra at the surface for a zenith view from 05 to 07 UT of 26 September 1997. The number of spectra in the averaging period was 15 for both instruments. The radiation measurements were complemented with best estimate atmospheric temperature and water vapor profiles.

The radiometric observations were made with two interferometers, called Atmospheric Emitted Radiance Interferometer (Revercomb et al. 1993) - AERI-00 and AERI-01. AERI-01 was the CART operational instrument while AERI-00 was a prototype. The data used in the exercise are the unapodised values at a spectral resolution of approximately  $0.48\text{ cm}^{-1}$ , corresponding to a maximum optical delay of about  $1.037\text{ cm}$ . A finite-field-of-view correction was applied to remove the effect of instrument self-apodisation. The data from both instruments was complemented with uncertainty estimates determined from the standard deviation of the spectra over the averaging period. The latter

includes also true atmospheric variability during the averaging period, but the time period from 05 to 07 UT was chosen because it was a relatively stationary situation, characterized by clear sky and relatively low water vapor level. The comparison of the measurements from the two instruments showed excellent agreement with water vapor amounts down by a factor of three with respect to earlier comparisons.

The best estimate profiles are the results of an effort by the data provider to merge information from different water vapor measurement techniques from instruments assembled at the SGP CART site (Knuteson, CIMSS, personal communication). These included sondes, tower sensors, microwave radiometers, raman lidars, solar observations and others. The profiles are complemented with error profiles.

## Results for CAMEX-1 case

Several simulated data sets were prepared using the LBL codes described previously. Each set served a different objective. The most important objectives of the exercise were to shed light in the differences produced by the different codes when applied to the same atmospheric profile and to identify spectral regions where forward model errors are smallest.

The upwelling radiances at flight altitude were computed assuming a predefined atmospheric layering defined by corresponding pressure and altitude levels using temperature, and level concentrations for 14 selected gaseous species ( $\text{H}_2\text{O}$ ,  $\text{CO}_2$ ,  $\text{O}_3$ ,  $\text{N}_2\text{O}$ ,  $\text{CO}$ ,  $\text{CH}_4$ ,  $\text{O}_2$ ,  $\text{NO}$ ,  $\text{SO}_2$ ,  $\text{NO}_2$ ,  $\text{N}_2$ ,  $\text{CCl}_3\text{F}$ ,  $\text{CCl}_2\text{F}_2$  and  $\text{CCl}_4$ ). The calculation of the sea surface emissivity was performed adopting the model of Masuda *et al.* (1988). The refractive index of pure water based on Hale and Querry (1973) was adjusted (Friedman (1969)) to the seawater value and then interpolated to each fine grid point to be given as an input with surface wind speed and the zenith angle to compute the rough sea surface emissivity. Since there are no direct measurements of the surface wind speed offshore, we assumed a reference value of  $7 \text{ m s}^{-1}$ . The choice of this parameter is not critical in that for a nadir view the dependence of the surface emissivity on the wind speed is only marginal. The original value of the skin temperature (293 K) was adjusted to 293.3 K since it was found that this value resulted in a better agreement with the observations. For the trace gases we have used AFGL atmospheric constituent profiles. For some of the species we retained the altitudinal gradient but scaled the absolute values at all levels to reflect more recent estimates of the surface values made at the stations of the Climate Monitoring and Diagnostic Laboratory (CMDL) and at the stations of the Advanced Global Atmospheric Gas Experiment (AGAGE) (for further information see <http://www.cmdl.noaa.gov> and <http://www.cdiac.esd.ornl.gov/ndps/alegacy.html>). The values used for these species are tabulated in table 4.

Table 4 : Volume mixing ratio for selected gaseous species

Specie	ppmv
CO2	358
CH4	1.7
N2O	0.32
CFC-11	$2.74 \text{ E}^{-4}$
CFC-12	$5.195 \text{ E}^{-4}$
CCL4	$1.07 \text{ E}^{-4}$

The sampling and resolution of the high spectral resolution computations were code dependent, based on the intrinsically different methodologies and definitions adopted by the three codes to compute the spectra, as it was discussed previously. The spacing of the monochromatic GENLN2 and RFM radiance computations is  $0.001\text{ cm}^{-1}$  while LBLRTM uses a variable spacing as discussed previously.

The methodology used to simulate the HIS measurements, in each of the three bands, involves the computation of the high resolution spectra for the spectral range from  $500\text{ to }3500\text{ cm}^{-1}$ , much larger than the total interval covered by the free spectral range of the three HIS bands. The spectra are then interpolated to an interval which is a power-of-2 sub-multiple of the HIS spectral spacing  $\Delta s$  (given in Table 2). The interpolated spectrum is tapered smoothly to zero outside the optical filter range and an interferogram is computed using Fast Fourier Transform (FFT) techniques. The interferogram is truncated beyond the maximum delay given for each band and zero filled to the number of intervals of the final convoluted spectrum. Finally, the truncated and zero-filled interferogram is inverse Fourier transformed to produce the simulated spectra that can be compared directly with the HIS data. The above processing was performed on all radiance sets using exactly the same code.

Improvements in the line parameter databases have been significant in the recent years. Of particular importance is the improvement of the water vapour lines in the infrared (Toth 1998). Consequently, in our computations we have utilized several databases to study the differences produced by different line parameters. In this study we have adopted the HITRAN database (HITRAN-2000 (Rothman et al. 2003) and HITRAN-2004 (Rothman et al. 2005) with updates from year 2001 and year 2006 respectively) and the GEISA-2003 (Husson et al. 2004) molecular databases.

The difference between the simulated and measured radiances for the three HIS bands is plotted in Figure 4 through Figure 9. Results are shown in units of equivalent brightness temperature for all the molecular databases used in the simulations. A number of broad features can be observed from the plots. In general a good agreement with observations is achieved by all models in the window region between  $800\text{ and }1000\text{ cm}^{-1}$ . Larger differences are found in the  $\text{CO}_2$   $\nu_2$  region ( $600\text{--}800\text{ cm}^{-1}$ ) and in the ozone band ( $1040\text{ cm}^{-1}$ ) where all models overestimate the measured radiances. In HIS band 2 a local maximum can be observed in the region where methane and water vapour lines are present (around  $1350\text{ cm}^{-1}$ ) and there is a marked tendency for the residuals to increase with wavenumber. HIS band 3 is characterized by the  $\text{CO}_2$   $\nu_3$  absorption band at  $2325\text{ cm}^{-1}$  where the behaviour of the lines is markedly sub-Lorentzian, hence difficult to model, and by the collision induced band of nitrogen at  $2350\text{ cm}^{-1}$ . Residuals in the  $2000\text{ cm}^{-1}$  region are most likely to be the result of the formulation of the line mixing for the  $\text{CO}_2$  Q branches at  $1932$ ,  $2076$ ,  $2093$  and  $2193\text{ cm}^{-1}$  and the water vapour continuum absorption. A noticeable feature of this region is the high level of measurement noise around  $2350\text{ cm}^{-1}$ .

Residuals for the three line-by-line models are very similar. Noticeable features are differences in the  $\text{CO}_2$   $\nu_2$  band around  $720\text{ cm}^{-1}$  where residuals for LBLRTM have an opposite sign to GENLN2 and RFM probably attributable to the different formulation of the Q branch line mixing, a slight different behaviour of GENLN2 in the  $1350\text{ cm}^{-1}$  region where residuals appear to be shifted towards larger negative values. A similar behaviour is observed for GENLN2 around  $2000\text{ cm}^{-1}$ . In the latter region this behaviour is consistent with the larger absorption due to the GENLN2 water vapour continuum model. It should be stressed however that, in general, where differences exist, they are of the order of a fraction of degree. The same conclusions can be drawn looking at differences between residuals obtained from the use of different molecular databases. Different line parameters appear to have a small impact on the residuals.

Because some spectral intervals are important in atmospheric temperature and humidity sounding problems we have performed an in-depth study of the absorption by comparing the residuals spectra to the HIS measured radiance spectrum and to the position of single absorption lines from CO<sub>2</sub> and H<sub>2</sub>O. The spectral regions we have selected are located between 740 and 800 cm<sup>-1</sup> (Figure 10) and between 2080 and 2200 cm<sup>-1</sup> (Figure 11). Note that these regions have also been chosen because the measurement error is lower than the difference between simulation and measurement. In the 740 to 760 cm<sup>-1</sup> spectral region all codes in general underestimate the measurement in proximity of the center of the CO<sub>2</sub> lines while overestimate the measurements in the weak absorbing regions between the lines. The distribution of strongest absorption in this region also shows very clearly that the main absorption features are sometimes due to single lines but most of the time it is the result of complex interaction between many lines and gaseous species. For example in the 780 to 800 cm<sup>-1</sup> region there are negative differences around 791.6 cm<sup>-1</sup> that are due to several closely spaced CO<sub>2</sub> lines of the Q-branch, a single strong (water vapour) line is responsible for the complex error structure at 784.5, 793.8 and 795.8 cm<sup>-1</sup> whereas three strong lines are responsible for the feature around 799 cm<sup>-1</sup>. It is well known that the situation is most complicated in regions where water vapour is the major absorber (i.e. HIS band 2). Here complex absorption is taking place from a multitude of intense water vapour lines.

A discussion on the results for band 3 is made more difficult because of the magnitude of experimental errors which is smaller than the difference with measurements only in a small interval from 2080-2200 cm<sup>-1</sup>. The strongest discrepancies (at 2090, 2115, 2136, 2181 cm<sup>-1</sup>) are due to interaction of several intense water vapour lines. The presence of CO absorption produces an alternating error structure with the negative maxima in phase with CO line centers, whose amplitude is comparable to the measurement error. No correlation is apparent between the differences and the highly regular N<sub>2</sub>O line structure that is not resolved by the measurements, and with the very complex but weaker line structure of ozone. Due to the high correlation between the simulations, one can infer that some of the "measurement noise" is in fact due to actual atmospheric variability.

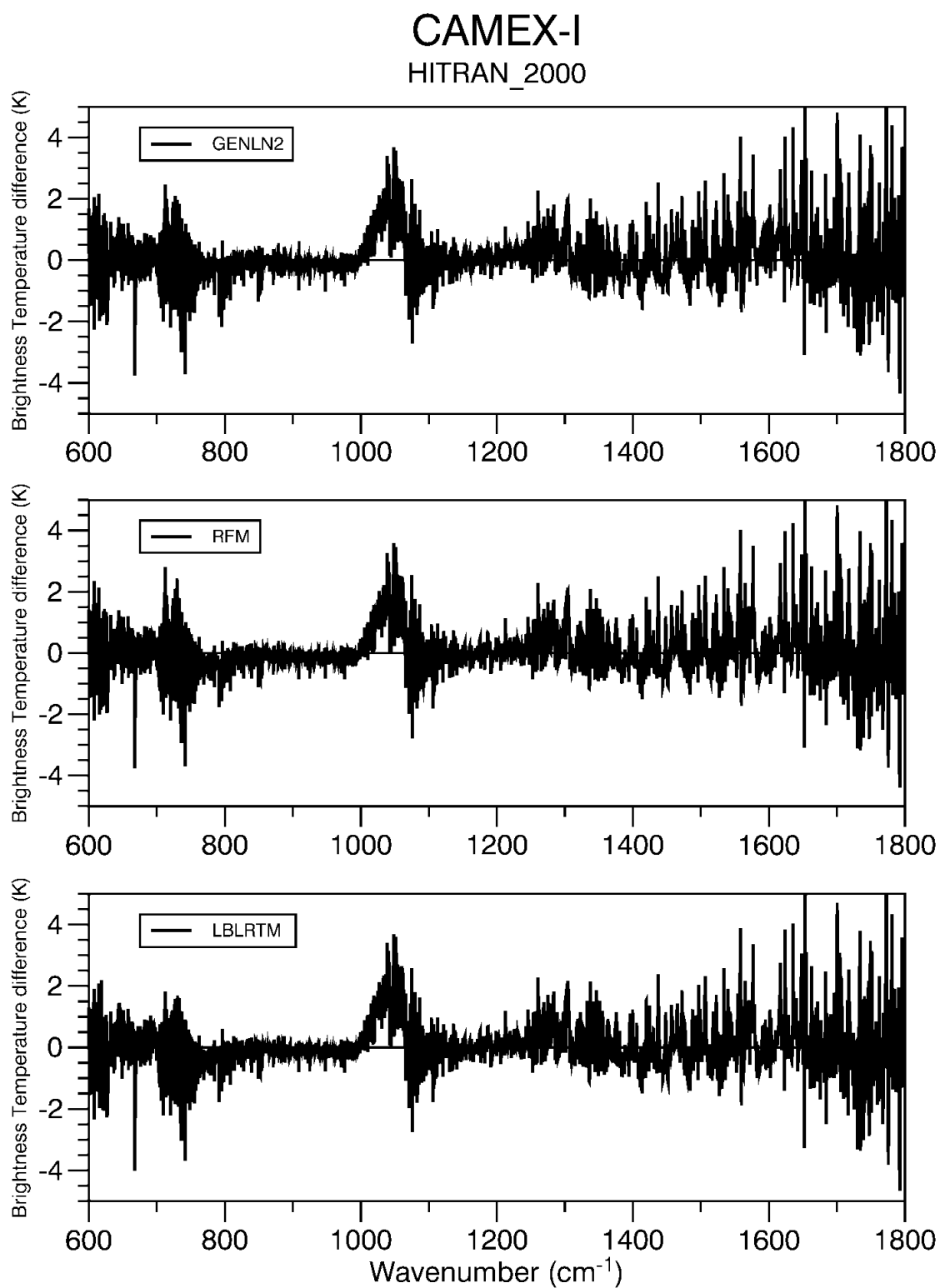


Figure 4: Radiance residuals between calculated and measured radiance for HIS band 1 and HIS band2. Calculated radiances were obtained using the HITRAN2000 molecular database.

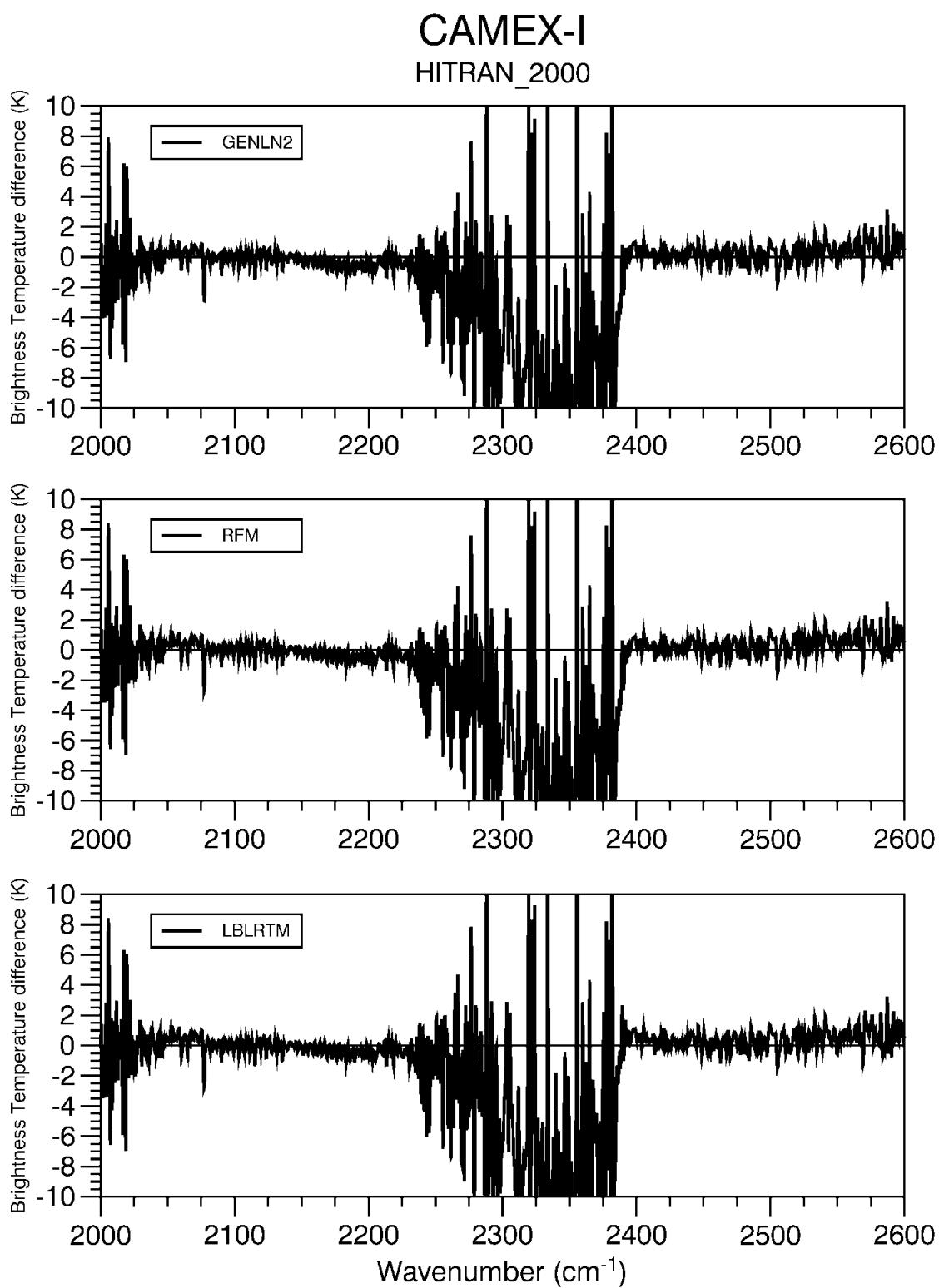


Figure 5: Radiance residuals between calculated and measured radiance for HIS band 3. Calculated radiances were obtained using the HITRAN2000 molecular database.

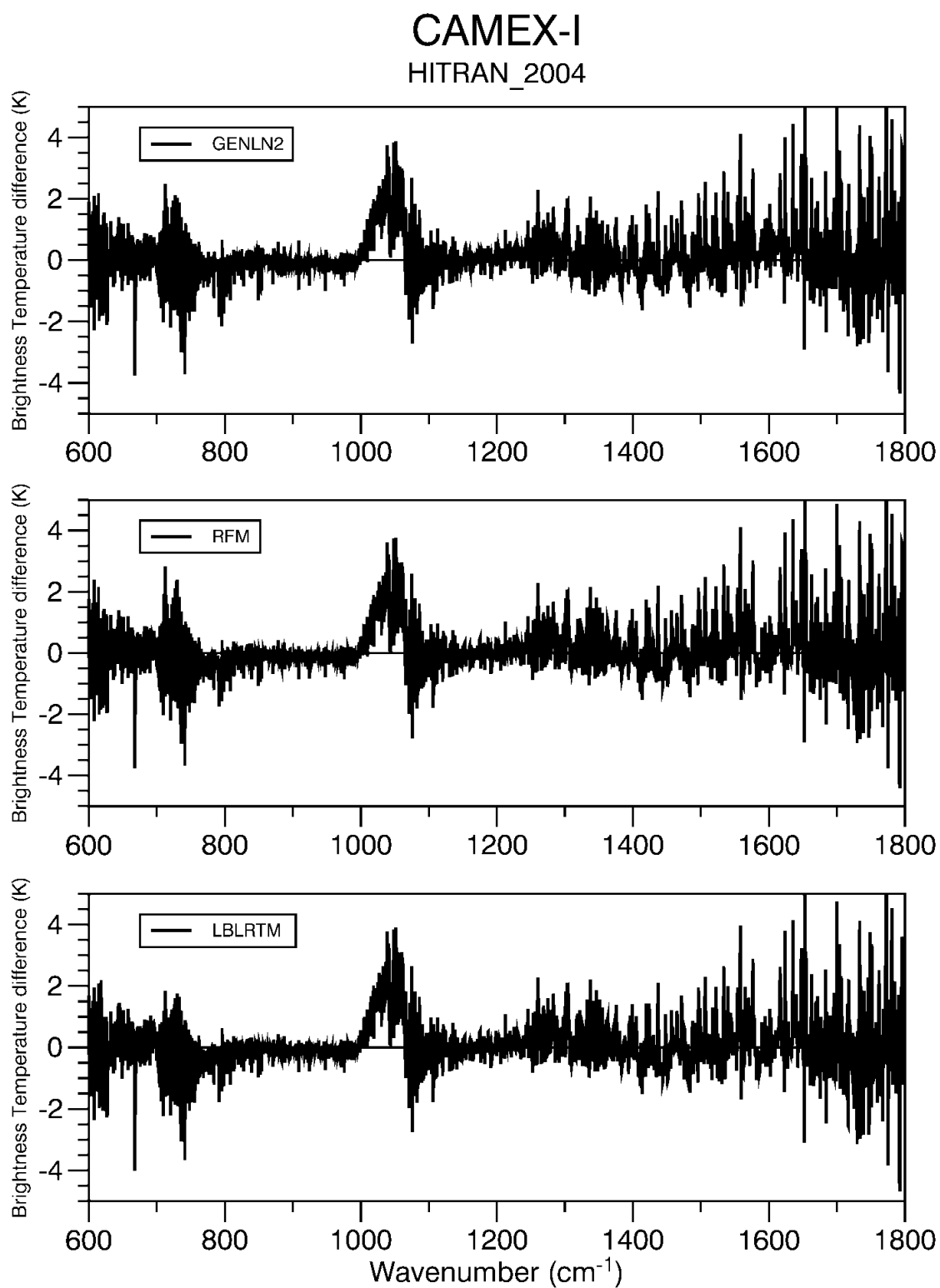


Figure 6: Radiance residuals between calculated and measured radiance for HIS band 1 and HIS band2. Calculated radiances were obtained using the HITRAN2004 molecular database.

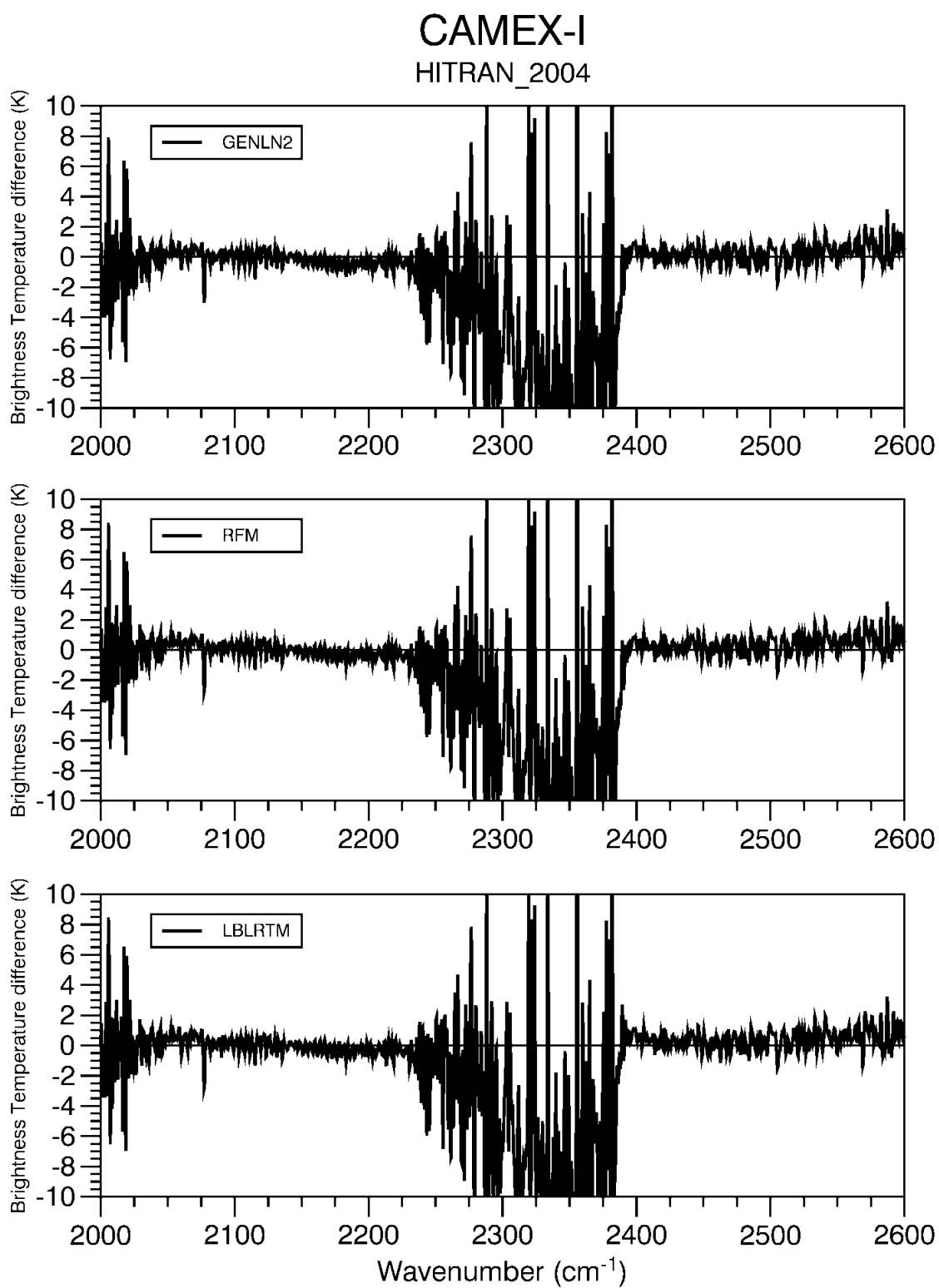


Figure 7: Radiance residuals between calculated and measured radiance for HIS band3. Calculated radiances were obtained using the HITRAN2004 molecular database.

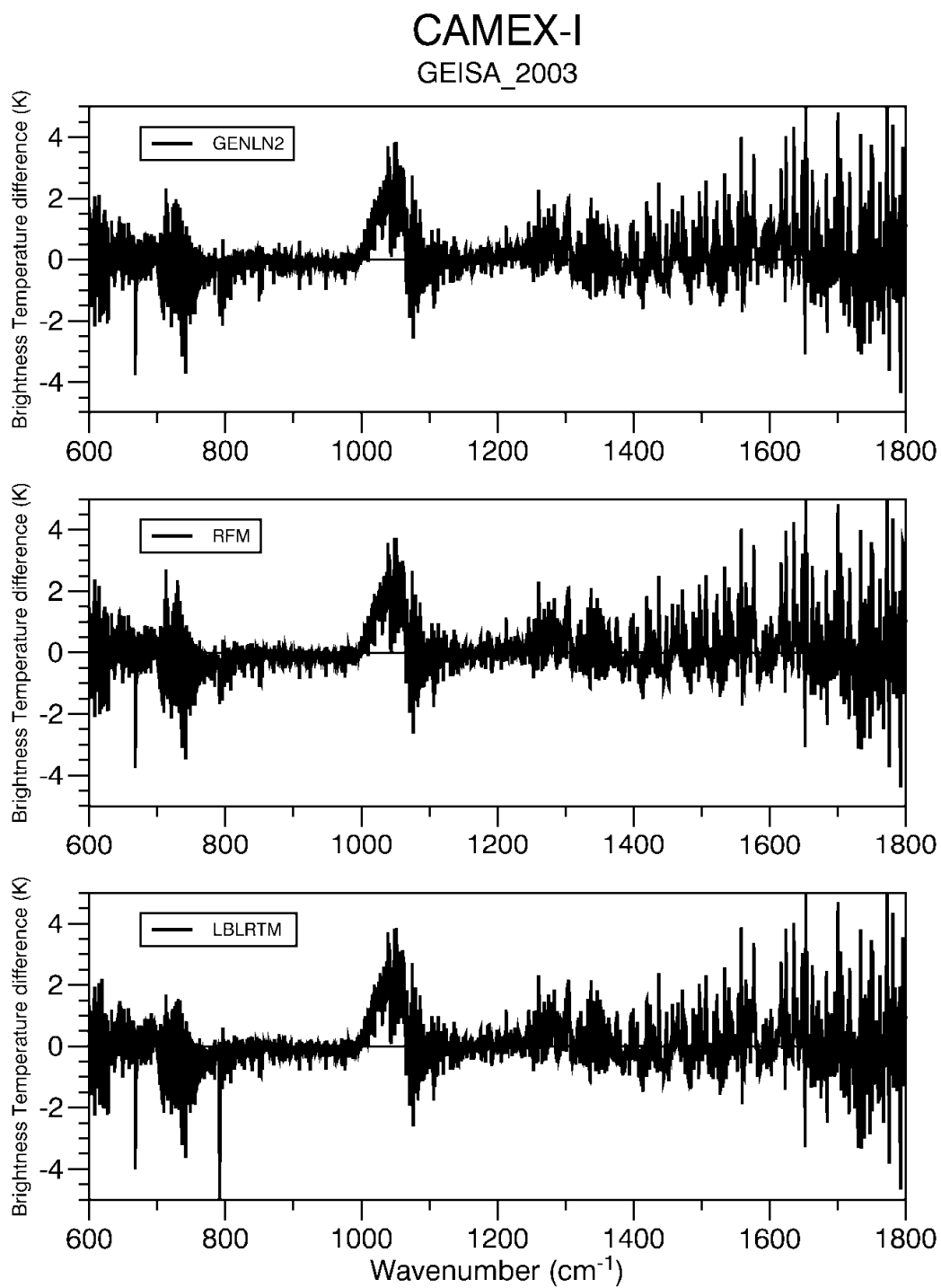


Figure 8: Radiance residuals between calculated and measured radiance for HIS band 1 and HIS band2. Calculated radiances were obtained using the GEISA2003 molecular database.

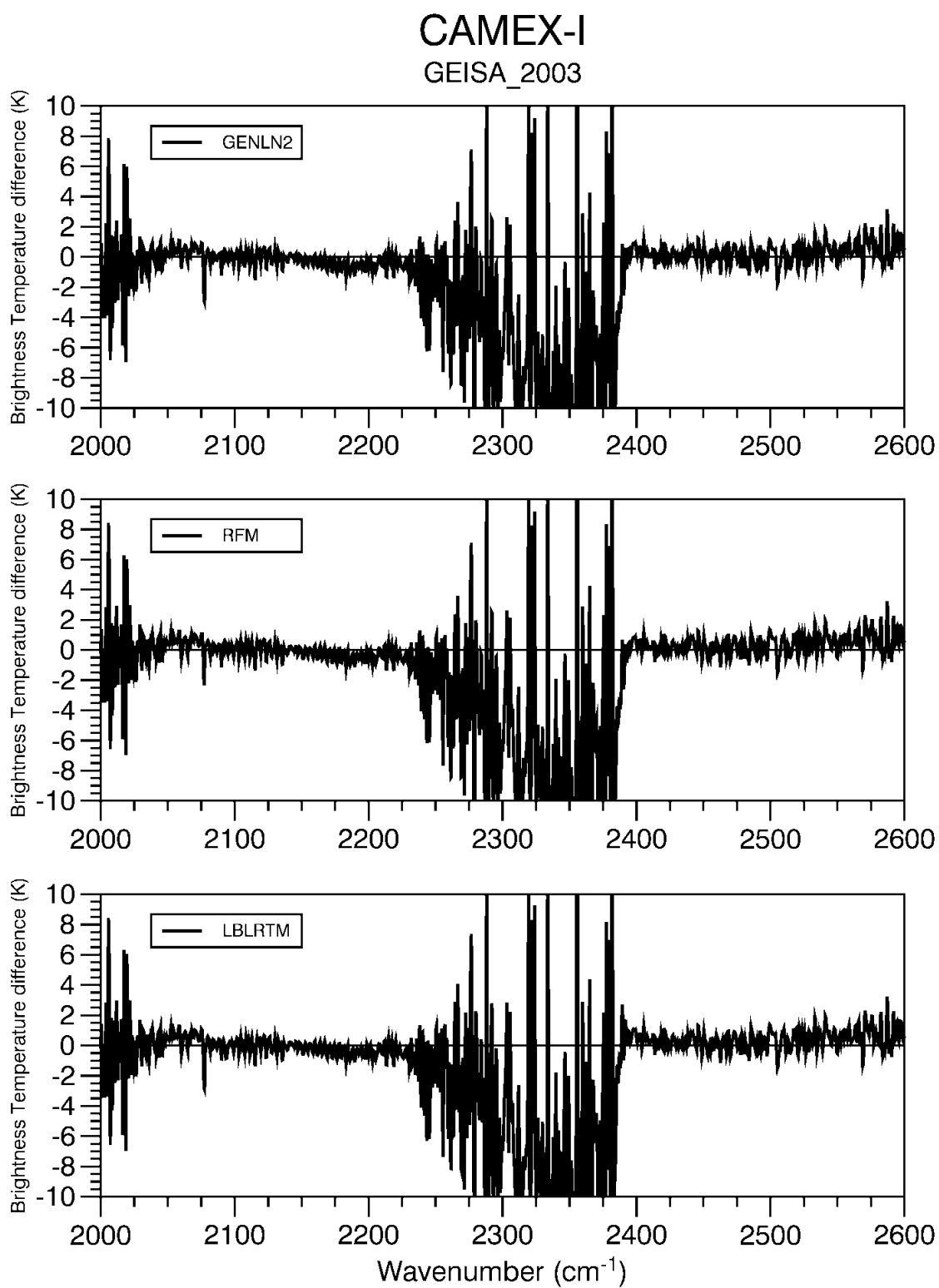


Figure 9: Radiance residuals between calculated and measured radiance for HIS band 3. Calculated radiances were obtained using the GEISA2003 molecular database.

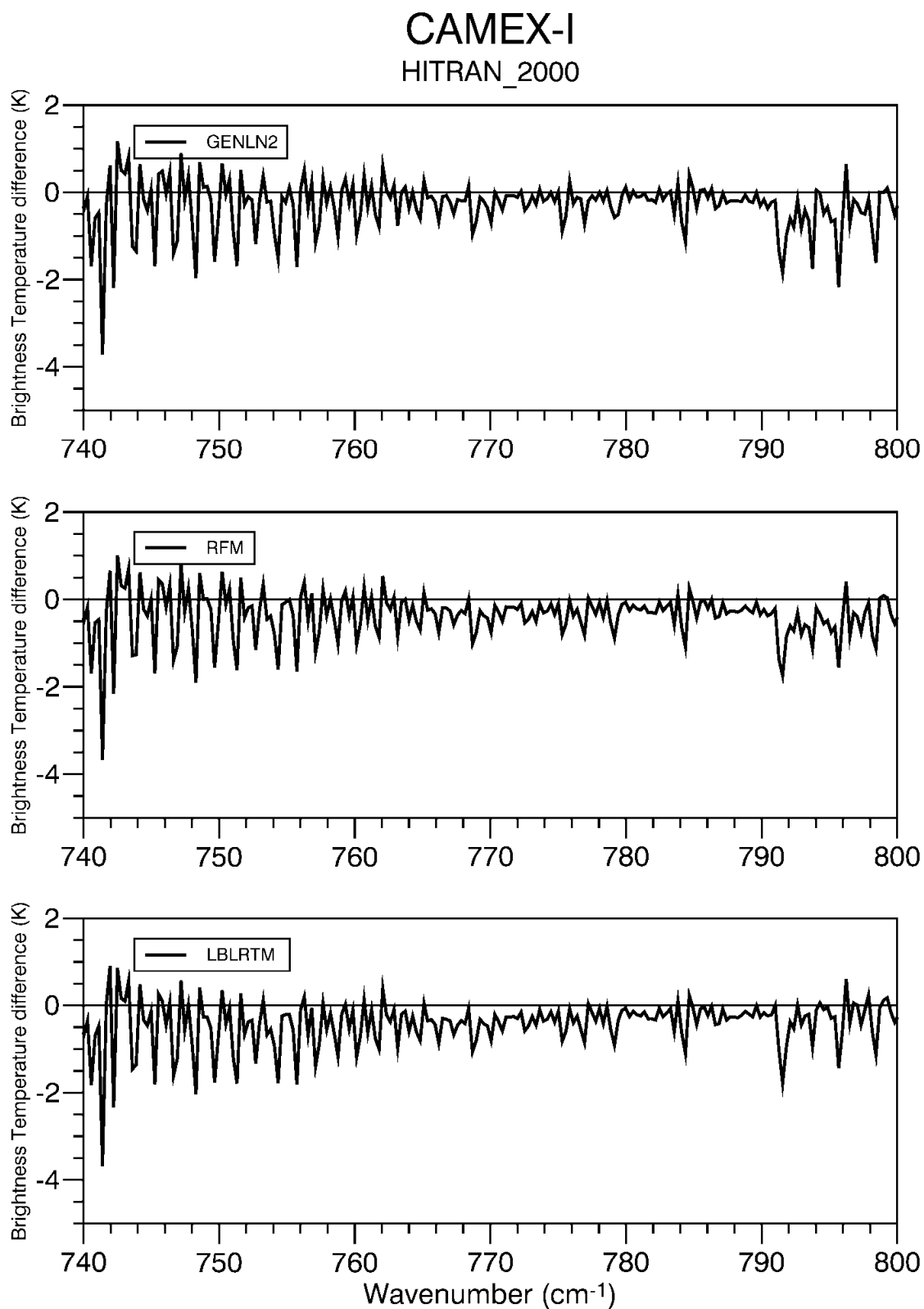


Figure 10: Radiance residuals between calculated and measured radiance for a selected spectral region in HIS band 1. Calculated radiances were obtained using the HITRAN2000 molecular database.

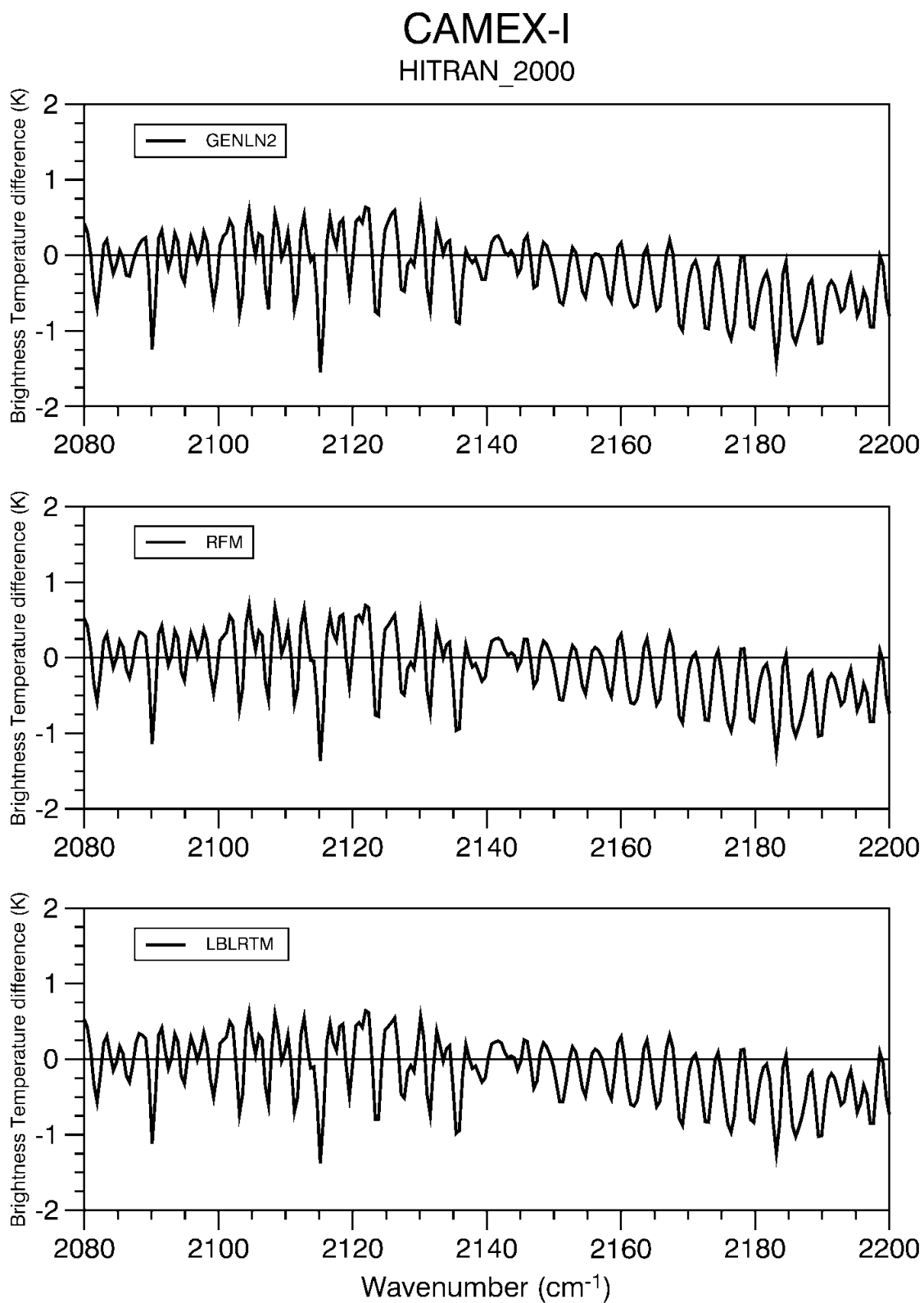


Figure 11: Radiance residuals between calculated and measured radiance for a selected spectral region in HIS band 3. Calculated radiances were obtained using the HITRAN2000 molecular database.

To gain a better insight into the performance of the three codes we have plotted the average (bias) and root-mean-square-error (rms) of the difference between the simulated and measured radiance over intervals of width  $50 \text{ cm}^{-1}$  (except at the extremes of bands where it may be larger: for example, the last interval for band 1 is 1000-1080).

In Figures 12 and 13 we have plotted the bias and rms for the three codes using the HITRAN2000 database in HIS band1-2 and HIS band 3 respectively, results for the HITRAN2004 database are plotted in Figures 14 and 15 and finally, results for the GEISA2003 database are plotted in Figures 16 and 17.

Results in band 1 indicate that the line-by-line codes considered in this study produce very similar results. The peak in the rms curves around  $740 \text{ cm}^{-1}$  shows that there are problems in simulating the high frequency branch of  $\text{CO}_2 \nu_2$  band. In this region LBLRTM appears to have a larger negative bias. The increase in bias in the  $950\text{-}1040 \text{ cm}^{-1}$  reflects a poor performance in simulating the ozone band, possibly caused by an inadequate representation of the ozone vertical distribution. In the centre of the ozone band RFM has a lower bias than GENLN2 and LBLRTM. Beyond  $1050 \text{ cm}^{-1}$  the increase in bias is most likely linked with the rapid increase of measurement error, defined by the standard deviation discussed previously and shown in the figures under consideration with a blue line (the measurement error is expressed in terms of noise-equivalent-delta-temperature (NEDT) at a blackbody temperature equal to the actual temperature of the scene). The rms error is generally below 1K and is slightly lower than the measurement standard deviation from  $820$  to  $980 \text{ cm}^{-1}$ . In this band RFM has a lower rms error beyond  $1000 \text{ cm}^{-1}$  whereas LBLRTM is performing slightly better in the  $800$  to  $1000 \text{ cm}^{-1}$  window region.

In band 2, a local rms maximum is seen around  $1320 \text{ cm}^{-1}$ , a spectral region where a large number of water vapour and methane lines are present. In terms of bias, slightly better results are obtained by each code in different spectral ranges across the water vapour band. However, beyond  $1400 \text{ cm}^{-1}$  the values of the bias and rms for LBLRTM are consistently lower than those for GENLN2 and LBLRTM. The sharp increase in rms above  $1500 \text{ cm}^{-1}$  occurs in a region where the measurement error is sharply increasing and significantly larger than the rms.

In band 3 one notes that between  $2250$  to  $2340 \text{ cm}^{-1}$  a region of high scatter is observed in correspondence with large values of the measurement error. The largest (negative) bias is found around  $2330 \text{ cm}^{-1}$ . The rms errors are almost identical for the three codes. It can be seen that in this band GENLN2 has a larger negative bias in the  $2000$  to  $2100 \text{ cm}^{-1}$  region and a smaller positive bias beyond  $2400 \text{ cm}^{-1}$ .

The larger positive bias of GENLN2 around  $1600 \text{ cm}^{-1}$  and the larger negative bias of GENLN2 around  $2000 \text{ cm}^{-1}$  is consistent with the continuum coefficients used in GENLN2. From figure 3 it can be seen that coefficients used in GENLN2 are smaller in the former region and larger in the latter region. The result is that when compared to RFM and LBLRTM, GENLN2 overestimates radiances in the  $1600 \text{ cm}^{-1}$  region and underestimates radiances in the  $2000 \text{ cm}^{-1}$  region. However, given the high level of noise in these regions is difficult to conclude which model is performing better.

If we compare results obtained from different line parameters we see that the impact is generally small with three noticeable exceptions. Firstly, the use of the HITRAN2004 and GEISA2003 line parameters produces larger errors in the ozone band; secondly, the use of the GEISA2003 database results in a larger bias and rms error for LBLRTM between  $700$  and  $800 \text{ cm}^{-1}$ . As discussed previously, this feature

is likely to be a result of a mismatch between the GEISA2003 line parameters and the CO<sub>2</sub> u2 Q branch line mixing coefficient implemented in LBLRTM. Finally, in the region between 1500 and 1600 cm<sup>-1</sup> the use of HITRAN2004 results, for all models, in a bias that is larger than the bias obtained by using the HITRAN2000 and GEISA2003 databases. In this region results for HITRAN2000 and GEISA2003 are almost identical. However is difficult to draw conclusions since the level of noise is very high.

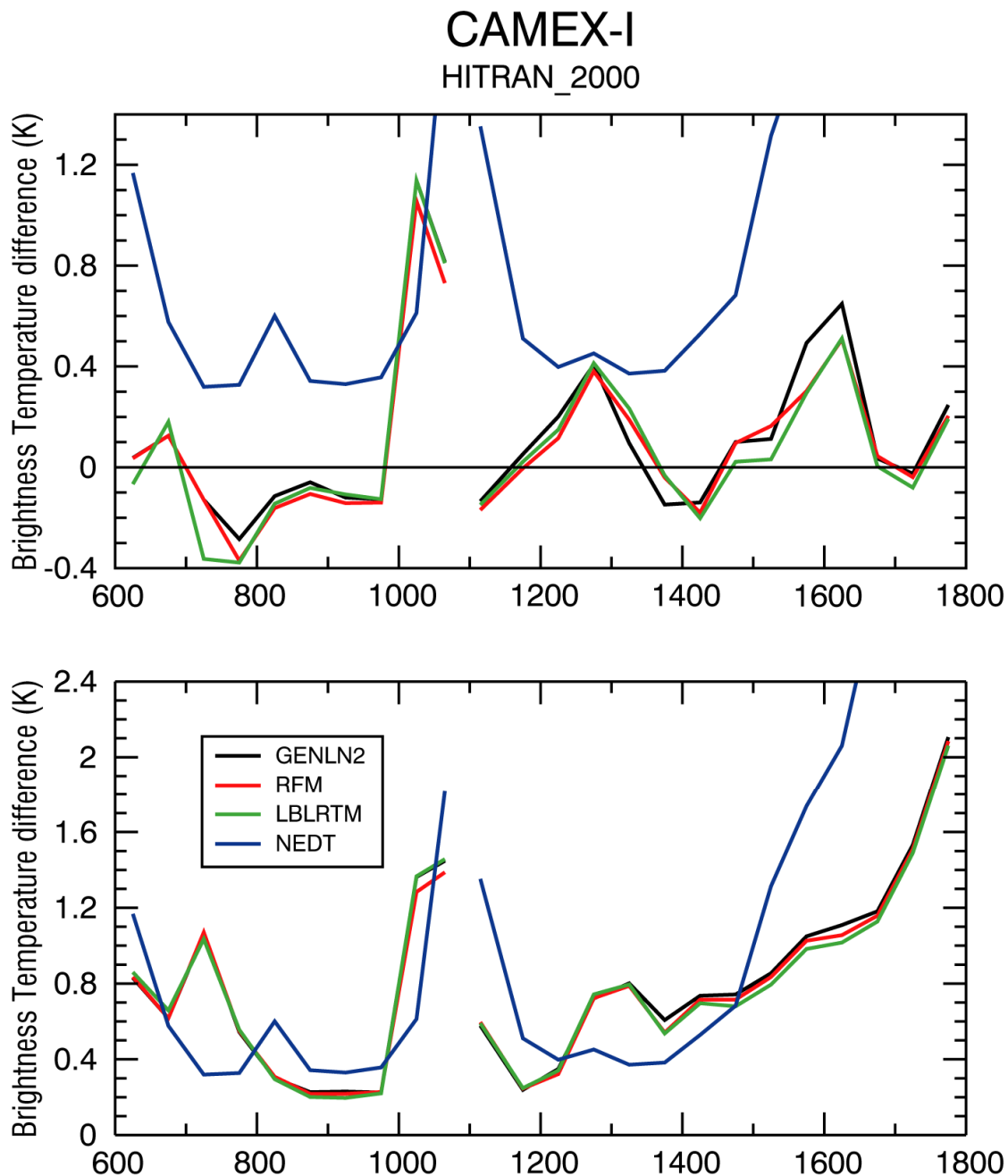


Figure 12: Bias (upper panel) and root-mean-square-error (lower panel) of the difference between simulated and measured spectra for the CAMEX-I case. Values for HIS band 1 and band 2 are computed over intervals of 50 cm<sup>-1</sup> using the HITRAN2000 molecular database.

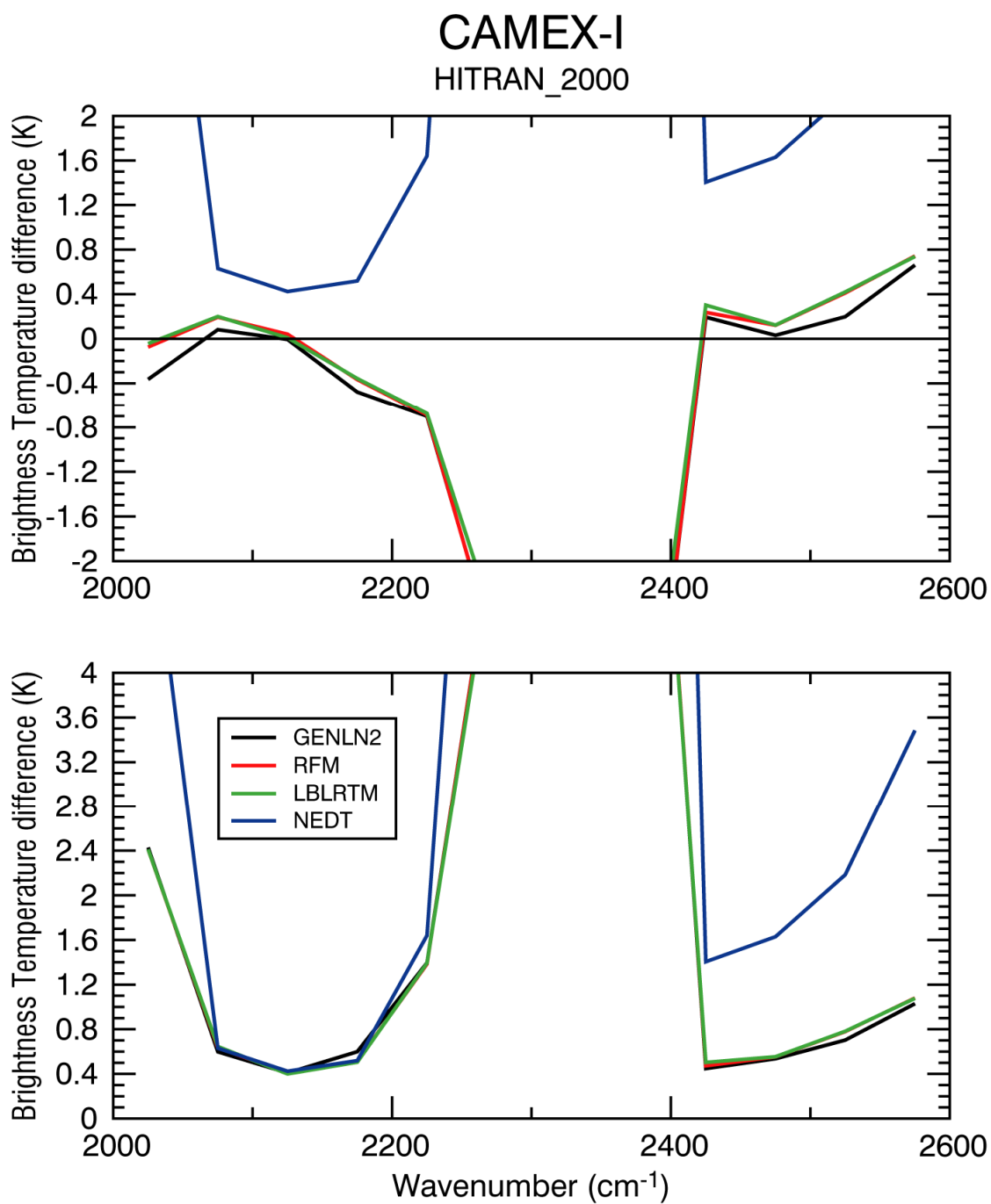


Figure 13: Bias (upper panel) and root-mean-square-error (lower panel) of the difference between simulated and measured spectra for the CAMEX-I case. Values for HIS band 3 are computed over intervals of  $50 \text{ cm}^{-1}$  using the HITRAN2000 molecular database.

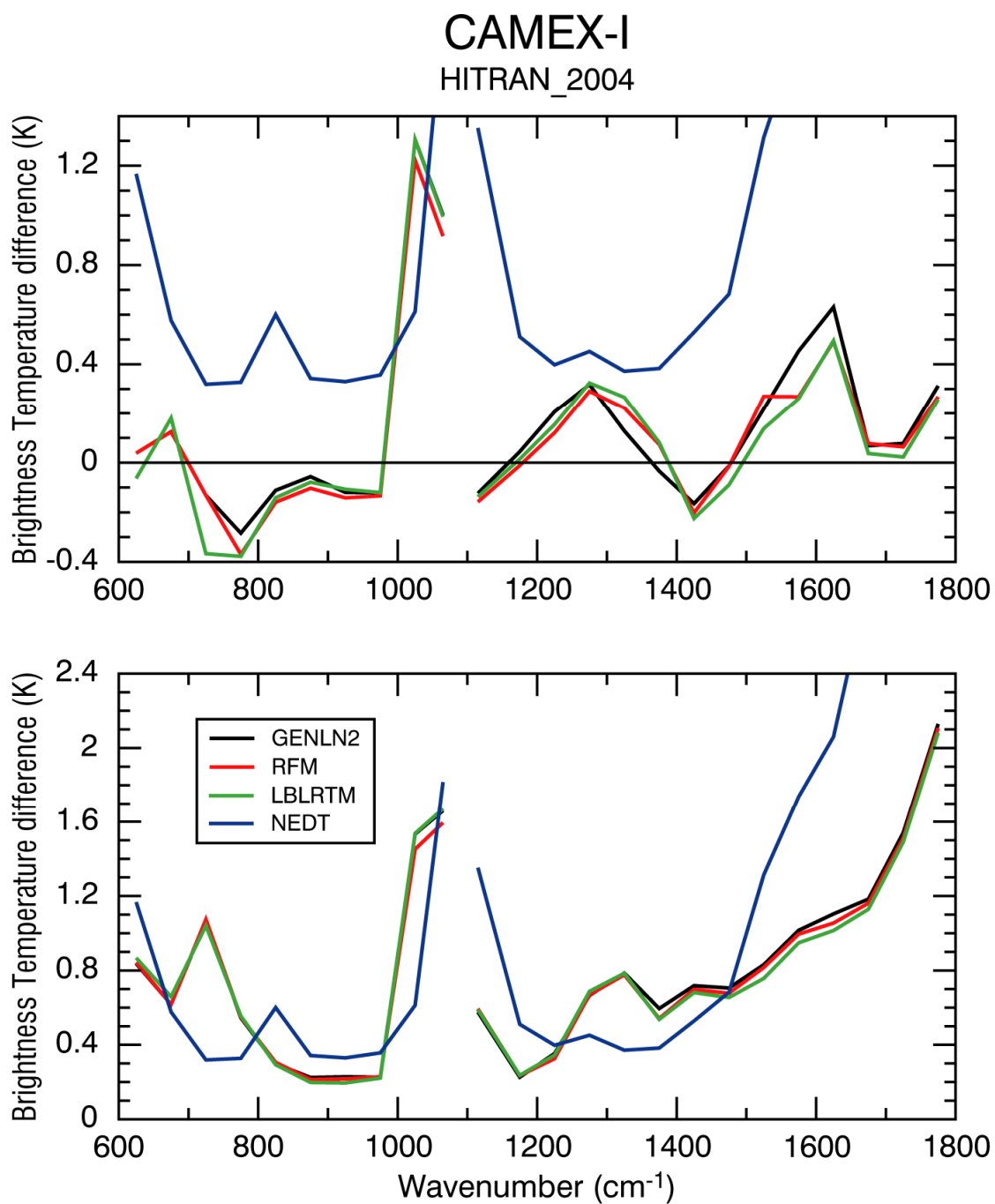


Figure 14: Bias (upper panel) and root-mean-square-error (lower panel) of the difference between simulated and measured spectra for the CAMEX-I case. Values for HIS band 1 and band 2 are computed over intervals of  $50 \text{ cm}^{-1}$  using the HITRAN2004 molecular database.

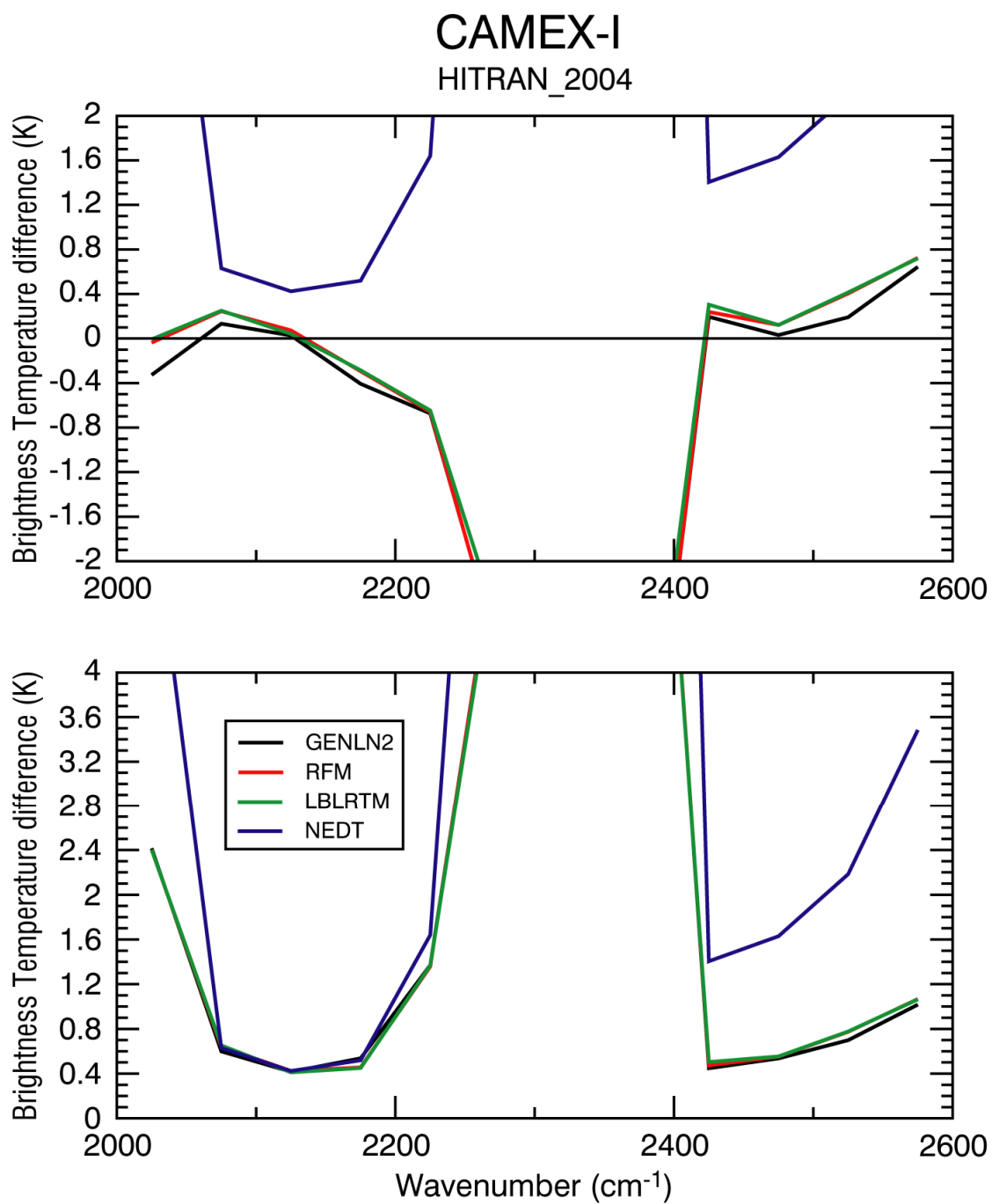


Figure 15: Bias (upper panel) and root-mean-square-error (lower panel) of the difference between simulated and measured spectra for the CAMEX-I case. Values for HIS band 3 are computed over intervals of  $50 \text{ cm}^{-1}$  using the HITRAN2004 molecular database.

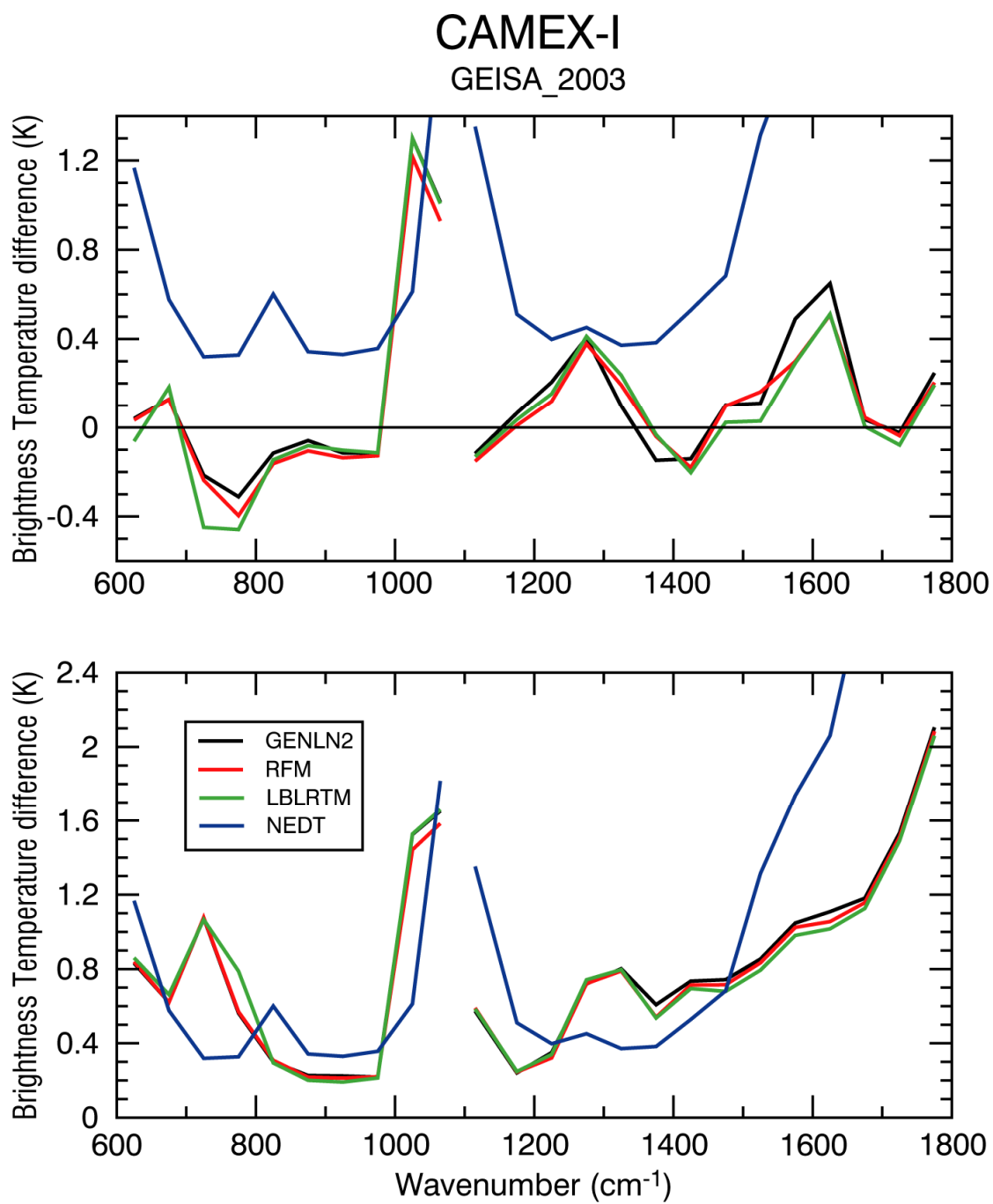


Figure 16: Bias (upper panel) and root-mean-square-error (lower panel) of the difference between simulated and measured spectra for the CAMEX-I case. Values for HIS band 1 and HIS band 2 are computed over intervals of  $50 \text{ cm}^{-1}$  using the GEISA2003 molecular database.

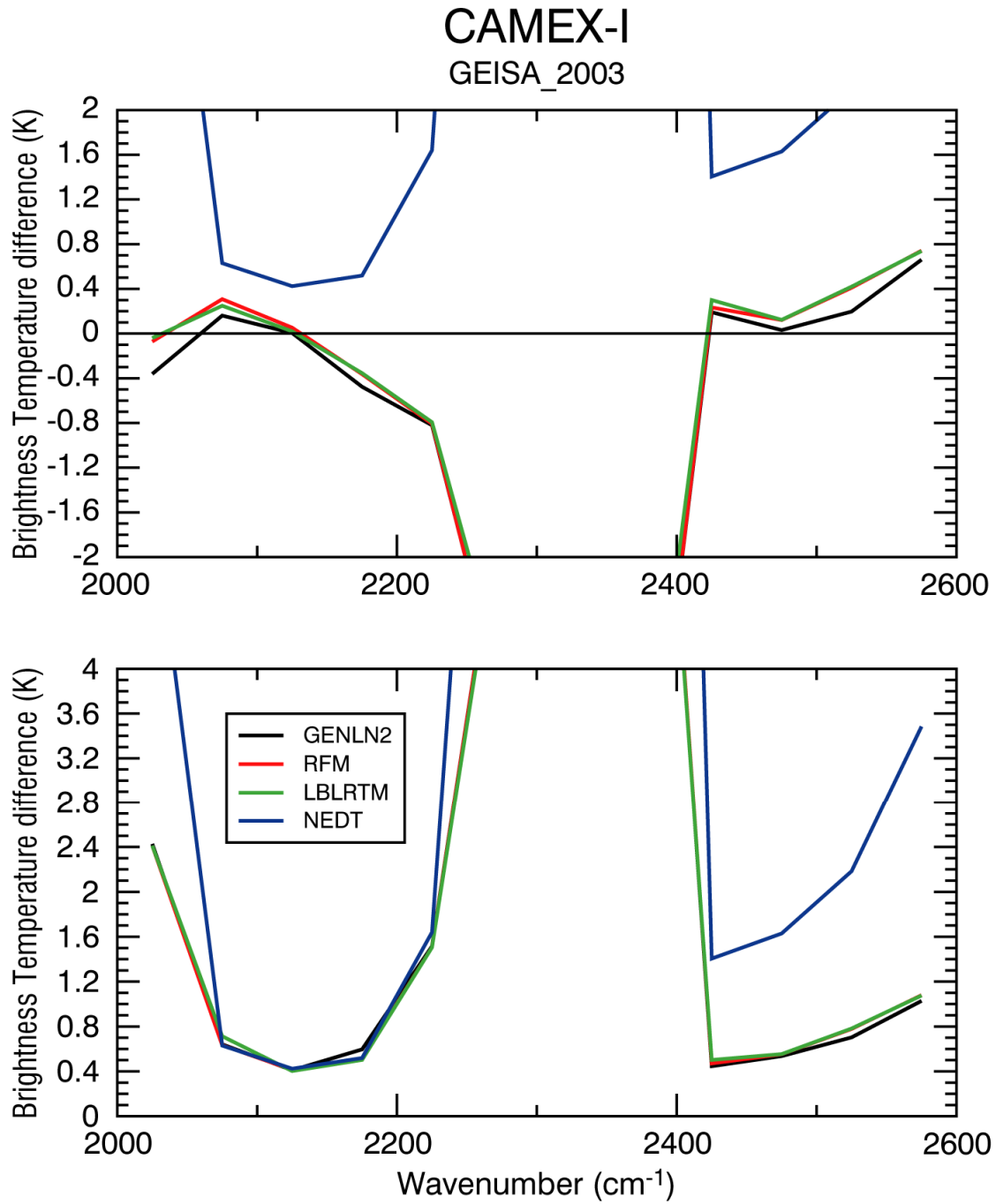


Figure 17: Bias (upper panel) and root-mean-square-error (lower panel) of the difference between simulated and measured spectra for the CAMEX-I case. Values for HIS band 3 are computed over intervals of  $50 \text{ cm}^{-1}$  using the GEISA2003 molecular database.

The differences generated by the use of different line parameters have been studied by comparing radiances computed by each single code to measured radiances using each single molecular database. Results can be found in Figures 18, 19 and 20 where for each single code we have plotted the rms of the difference between simulated and measured radiances obtained from the three

molecular databases considered in this study. In figure 18 it can be seen that for GENLN2 the use of different line parameters results in generally small differences. A noticeable feature is the reduction of rms in the ozone band due to the use of the HITRAN2000 database. Results obtained from the use of HITRAN2000 and GEISA2003 are almost identical in all spectral regions. The use of the HITRAN2004 database results in a marginally lower rms around 1300, 1500, and 2200  $\text{cm}^{-1}$ . Similar conclusion can be drawn looking at the plots for the RFM case. For the LBLRTM case we have introduced the use of the TES database since this is the only database that can be used in conjunction with the formulation of the CO<sub>2</sub> u2 P-R branch line mixing implemented in LBLRTM. Results for this case are shown in figure 20. It can be seen that the use of TES database has a positive impact in reducing the rms in the 620 to 670  $\text{cm}^{-1}$  region. In other spectral regions results are almost identical to those obtained from the use of HITRAN2004. As for the GENLN2 and RFM cases, the utilization of HITRAN2004 does seem to have a positive, albeit marginal, impact in reducing errors in the water vapour band.

To shed more light on the results discussed above we give the plot of the radiance residuals between radiances calculated using the GEISA20003 and HITRAN2004 databases using the RFM model. Results are shown in Figure 20. We have chosen the RFM model to avoid the issue of the mismatch between line parameters and CO<sub>2</sub> line mixing coefficients encountered in LBLRTM and because RFM incorporates a version of water continuum model that is more recent than that used in GENLN2. It can be seen that residuals are almost everywhere smaller than 0.2 K with outliers in the water vapour band and in the CO<sub>2</sub> u3 region. Residuals in the CO<sub>2</sub> bands appear to have a systematic nature whereas those in the water vapour band display a larger scatter. It is interesting to note how looking at figures 18, 19 and 20, in the regions where the residuals are larger, results obtained using HITRAN2004 are in better agreement, albeit marginally, with observations.

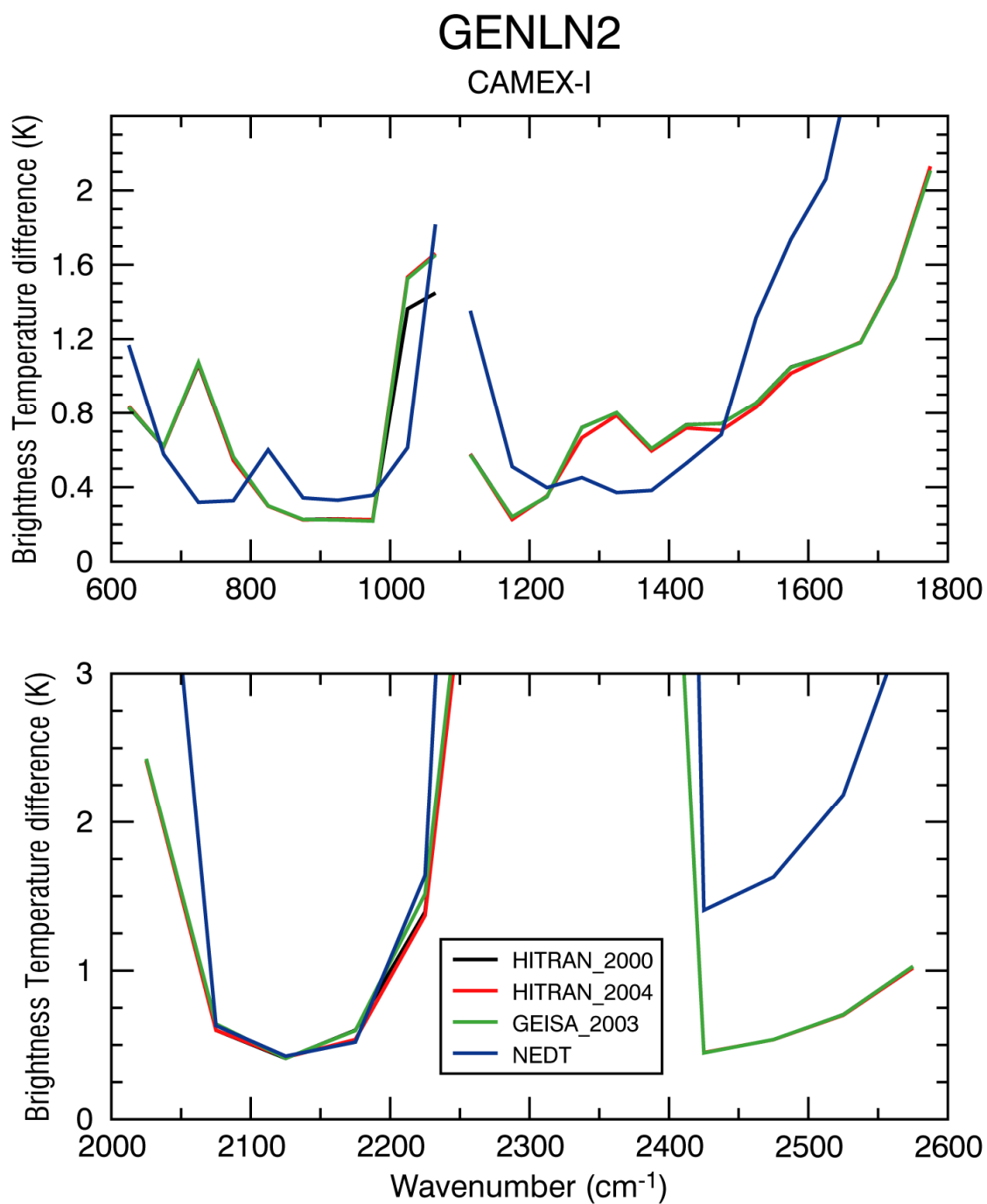


Figure 18: Root-mean-square-error of the difference between simulated and measured spectra for the CAMEX-I case. Values for HIS band 1 and HIS band 2 are shown in the upper panel, values for HIS band 3 are shown in the lower panel. Spectra are computed using the GENLN2 model utilizing the HITRAN2000, HITRAN2004 and GEISA2003 molecular databases.

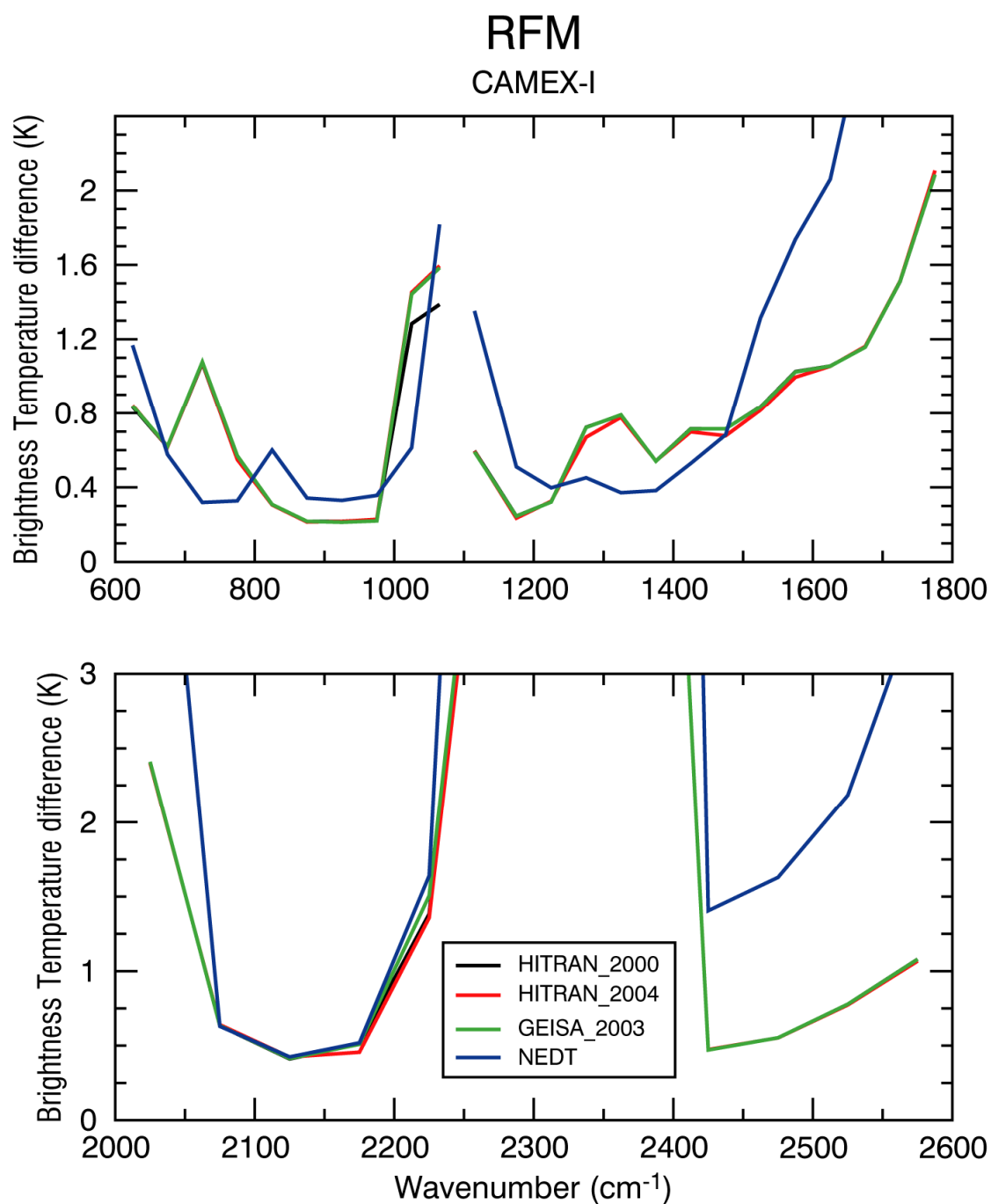


Figure 19: Root-mean-square-error of the difference between simulated and measured spectra for the CAMEX-I case. Values for HIS band 1 and HIS band 2 are shown in the upper panel, values for HIS band 3 are shown in the lower panel. Spectra are computed using the RFM model utilizing the HITRAN2000, HITRAN2004 and GEISA2003 molecular databases.

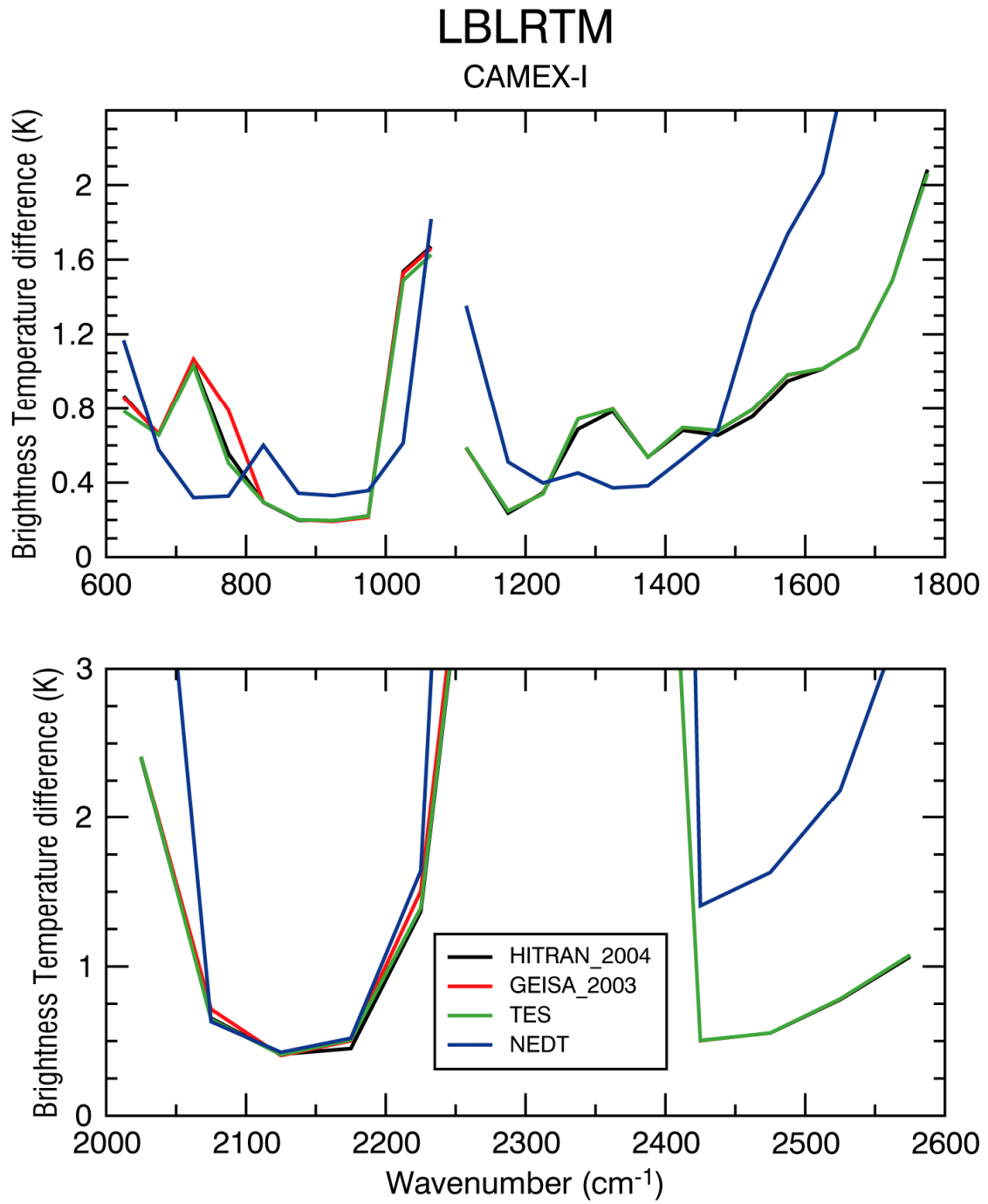


Figure 20: Root-mean-square-error of the difference between simulated and measured spectra for the CAMEX-I case. Values for HIS band 1 and HIS band 2 are shown in the upper panel, values for HIS band 3 are shown in the lower panel. Spectra are computed using the LBLRTM model utilizing the HITRAN2004, GEISA2003 and TES molecular databases.

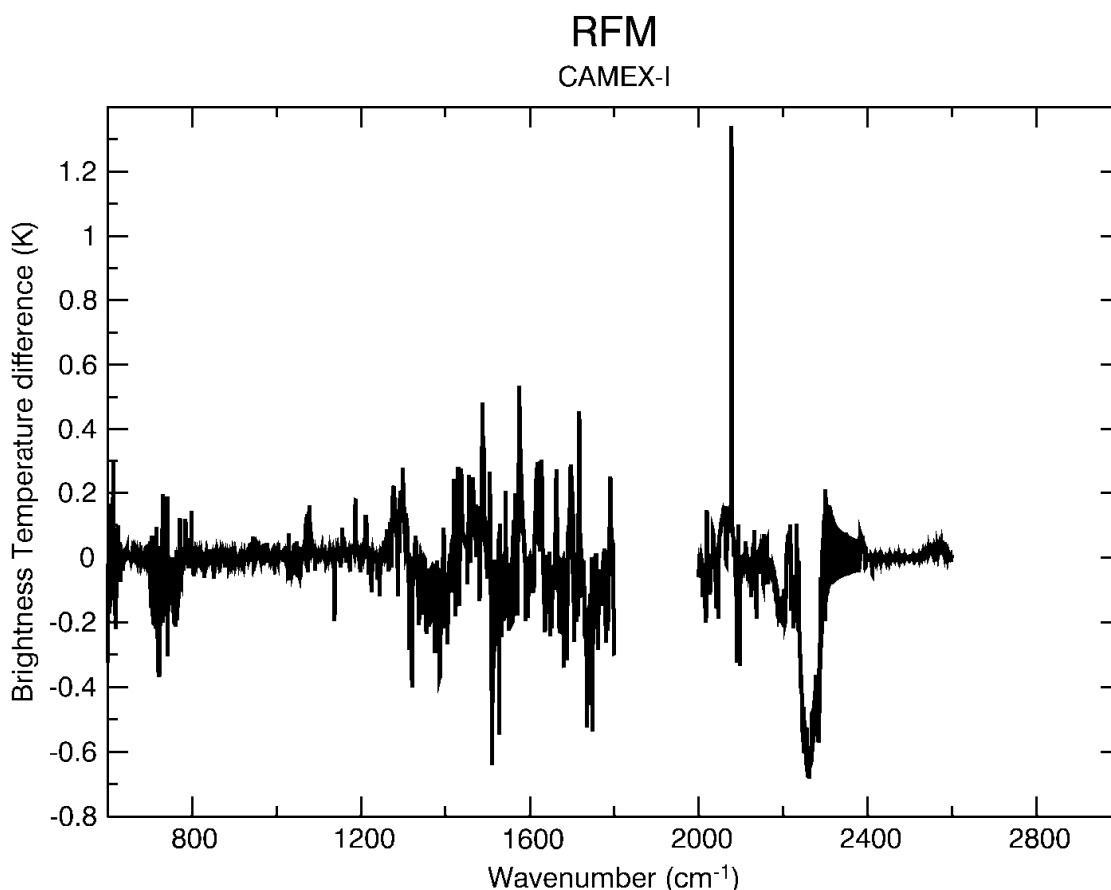


Figure 21: Radiance residuals between radiances calculated using the GEISA2003 database and radiances calculated using the HITRAN2004 database. Spectra are computed using the RFM model.

It is interesting to note how, in many spectral regions, the magnitude of the differences between simulations and measurements is much larger than the difference between the codes as shown in Figure 22 for the HITRAN2004 case. This indicates that the problems encountered, for example in simulating the high frequency CO<sub>2</sub>  $\nu_2$  band, are likely of spectroscopic nature although in this case, because of the magnitude of the difference between RFM and LBLRTM, it cannot be ruled out that the different implementation of the Q branch line mixing is contributing significantly to the error. This means that in the spectral regions where differences between the codes are comparable to or larger than differences between simulations and measurements there is scope for improvement. This can be demonstrated by looking at the region close to the water vapour vibrational resonant frequency where the agreement between LBLRTM and RFM is much better than the agreement between GENLN2 and RFM or between GENLN2 and LBLRTM. The reason for that is because RFM and LBLRTM use the same water vapour continuum model. The same water vapour continuum model is likely to be responsible for the closer agreement between LBLRTM and RFM in the 2000 to 2200 cm<sup>-1</sup> region.

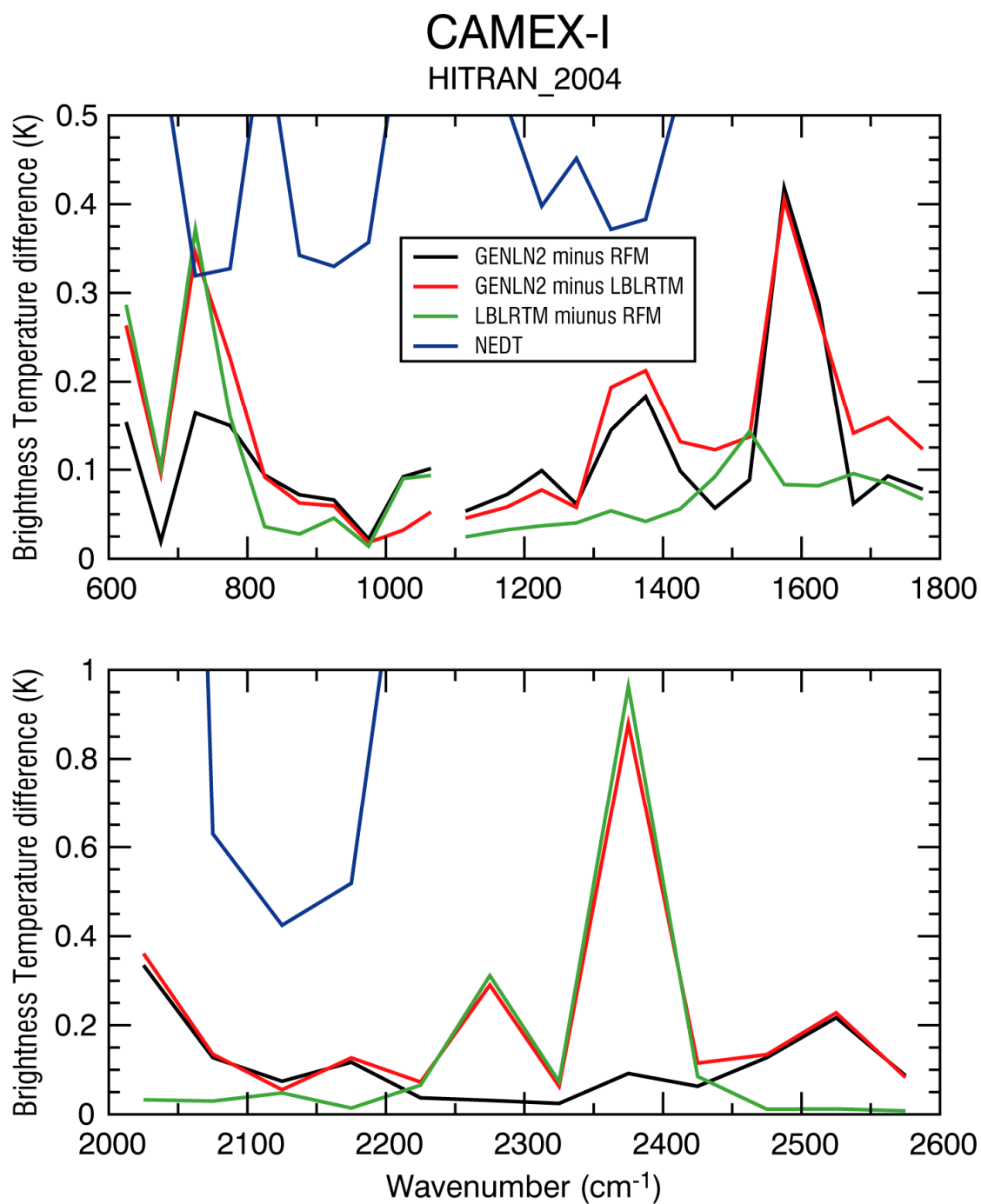


Figure 22: Root-mean-square-error of the difference between simulated spectra for the CAMEX-I case. Values for HIS band 1 and HIS band 2 are shown in the upper panel, values for HIS band 3 are shown in the lower panel.

### Sensitivity to changes in humidity profile

As already mentioned previously, the CAMEX-1 dataset contains estimates of extreme relative humidity values. The modeling of atmospheric radiative transfer is affected by uncertainties in the characterization of water vapour and temperature atmospheric profiles. Although a detailed

assessment of the errors resulting from these uncertainties is outside the scope of this paper, the GENLN2 was used to investigate the sensitivity of the HIS radiances to changes in the humidity profile. Errors assumed here are an upper limit and, as shown in Fig. 23, they vary with level, ranging from less than 5% in the lower troposphere to up 200% in the upper troposphere/stratosphere.

For the perturbed case the bias and rms were computed as the difference between the simulated radiance calculated by increasing and decreasing the reference profile by the error profile and the simulated radiance calculated using the reference profile. The relative bias and relative rms were then computed by dividing the bias and the rms by the average measured radiance in the given interval. Figures 24(a) and 24(b) show the relative bias and the relative rms for the reference case whereas for the perturbed case only the relative bias is shown since, as explained below, the bias and rms are comparable. Results are only shown for band-1 and band-2 since for band-3 the measurement error is too large. Band-2 is where the impact of the perturbed profile is greatest. For this band perturbing the humidity profile gives a signal that is well above the discrepancy generated by the forward model at least in the spectral regions where the peak of the weighting functions is attained in the upper troposphere. Elsewhere the signal is comparable with that generated by the forward model. In the temperature-sounding band, band-1, results are mixed in that the rms is well below the reference level and the bias is at the reference level in most of the spectral range. These results are not straightforward to interpret. It is likely that the relative humidity errors are overestimated in that their inclusion in the forward calculation is expected to generate a signal that is not actually seen. It is worth noting however that since the rms and bias of the signal generated by the error profile are comparable, one effect of perturbing the humidity profile is to impart an offset to the radiance.

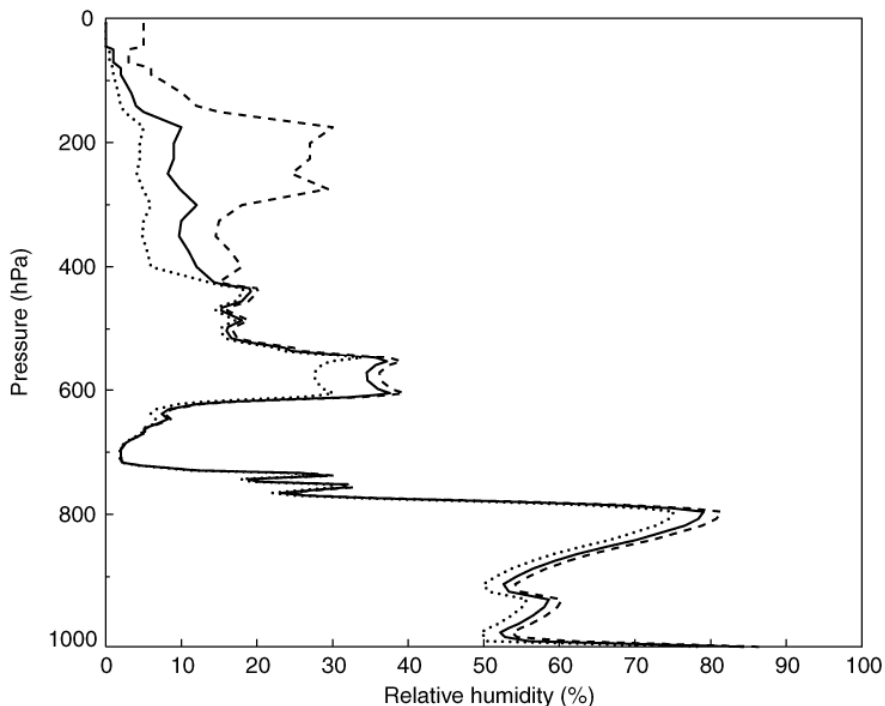


Fig 23: The relative humidity error profile for the CAMEX-1 case.

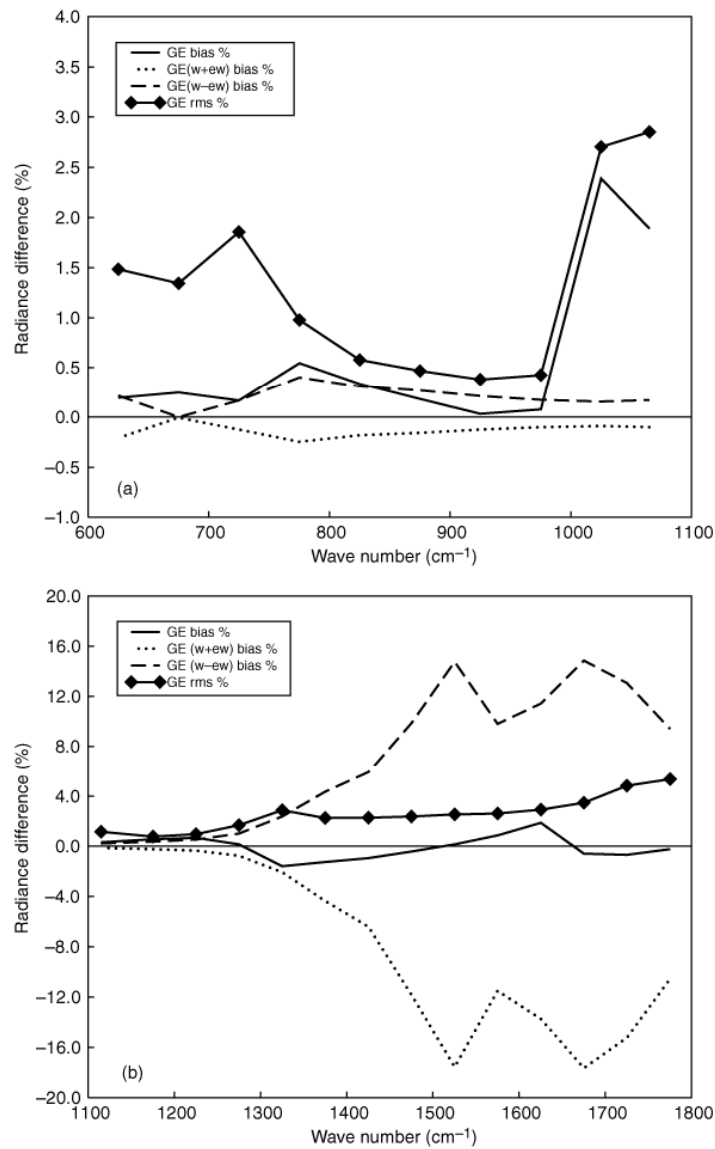


Fig 24: The relative bias of the difference between the reference GENLN2 spectra and those computed by increasing (GE (w+ew)) and decreasing (GE (w-ew)) the water vapour profile by the error profile for the CAMEX-1 case. The relative bias and root-mean-square-error of the difference between the reference GENLN2 spectra and the measured spectra is also shown as solid and solid-diamond line (GE). Values computed over intervals of 50 cm<sup>-1</sup> width are shown for: (a) band-1; (b) band-2.

## Results for CAMEX-III case

The computation of the upwelling radiances at flight altitude was performed applying the same methodology adopted for the CAMEX-I case. In particular we used the same predefined atmospheric layering with adjustments made to the pressure levels at surface and at flight altitude. The line-by-line computations were performed using the same sampling and resolution including the same 14 selected gaseous species. Values of the sea surface emissivity were computed using the model by Masuda et al. (1998) with adjustments for the salinity. It should be noted that although it was originally assumed that measurements were made looking at nadir it was discovered (Masiello, University of Basilicata, personal communication) that measurements were actually made 3° off nadir. This is the value adopted in this study for the radiance and emissivity computations. As discussed previously, the

profiles of water vapour and temperature used in this study are those obtained from the inversion of the NAST-I radiances. For the skin temperature we used the retrieved value of 300.4 K. The mixing ratio values adopted for a selected number of trace gas species are tabulated in table 5. The spectrum used in this study is a single measurement spectrum and the measurement error consists only of the radiometric noise. It is unfortunate that between 2200 and 2400  $\text{cm}^{-1}$  the level of noise is such to render impossible any comparison between measured and computed radiances.

Table 5: Volume mixing ratio for selected gaseous species

Specie	ppmv
CO <sub>2</sub>	363.8
CH <sub>4</sub>	1.8
N <sub>2</sub> O	0.314
CFC-11	$2.62 \text{ E}^{-4}$
CFC-12	$5.41 \text{ E}^{-4}$
CCL <sub>4</sub>	$9.89 \text{ E}^{-5}$

The methodology used to simulate NAST-I radiances has not involved FFT techniques since a code developed to convolve IASI simulated radiances was ready available that performs the convolutions of synthetic spectra in the wavenumber space using the specified spectral response function (i.e. a cardinal sinc function).

The radiance residuals between simulated and measured radiances for the three NAST-I bands are plotted in Figure 25, 26 and 27. Results are shown in units of equivalent brightness temperature for all the molecular databases utilized in the simulations. It is evident that because of the larger number of channels the residual plots show more structure than those for the CAMEX-I case. There are however a number of features in common. The better agreement with observations is achieved by all models in the window region between 800 and 1000  $\text{cm}^{-1}$ ; larger differences are found in the CO<sub>2</sub>  $\nu_2$  region (600-800  $\text{cm}^{-1}$ ) and in NAST-I band 2 where a local maximum can be observed in the region where methane and water vapour lines are present (around 1350  $\text{cm}^{-1}$ ). A local maximum also exist and in the ozone band (1040  $\text{cm}^{-1}$ ) but, possibly as the results of a better specification of the atmospheric state for this specie, residuals are significantly lower than residuals observed for the CAMEX-I case. A noticeable feature is the large value of the residuals for a number of strong water vapour lines in NAST-I band 2. Because of the large radiometric noise is not possible to comment the features observed in the CO<sub>2</sub>  $\nu_3$  absorption band at 2325  $\text{cm}^{-1}$ . Finally, all the line-by-line models appear to capture the absorption of the various gaseous species in a remarkably similar way.

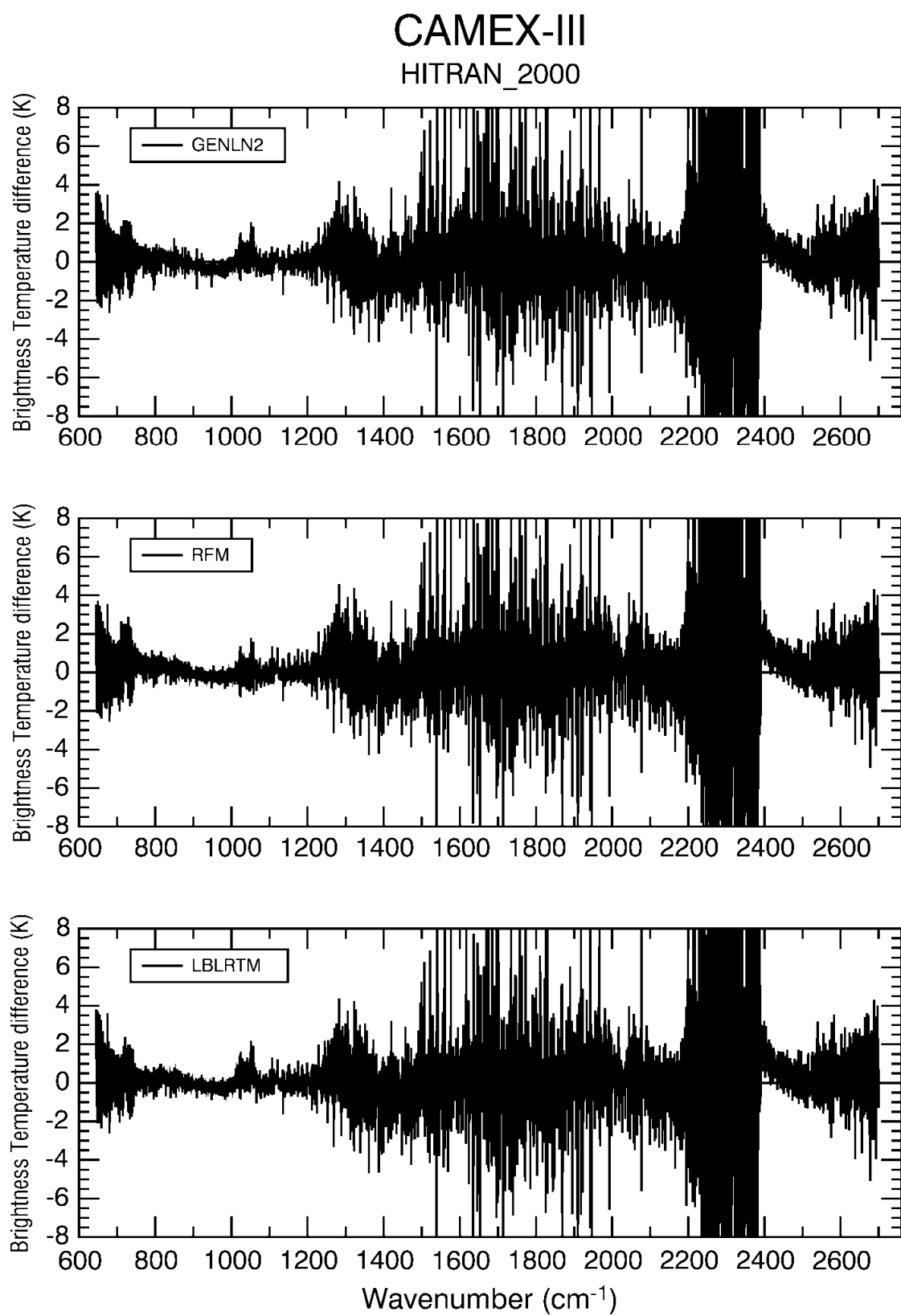


Figure 25: Radiance residuals between calculated and measured radiance for NAST-I. Calculated radiances were obtained using the HITRAN2000 molecular database.

# CAMEX-III

HITRAN\_2004

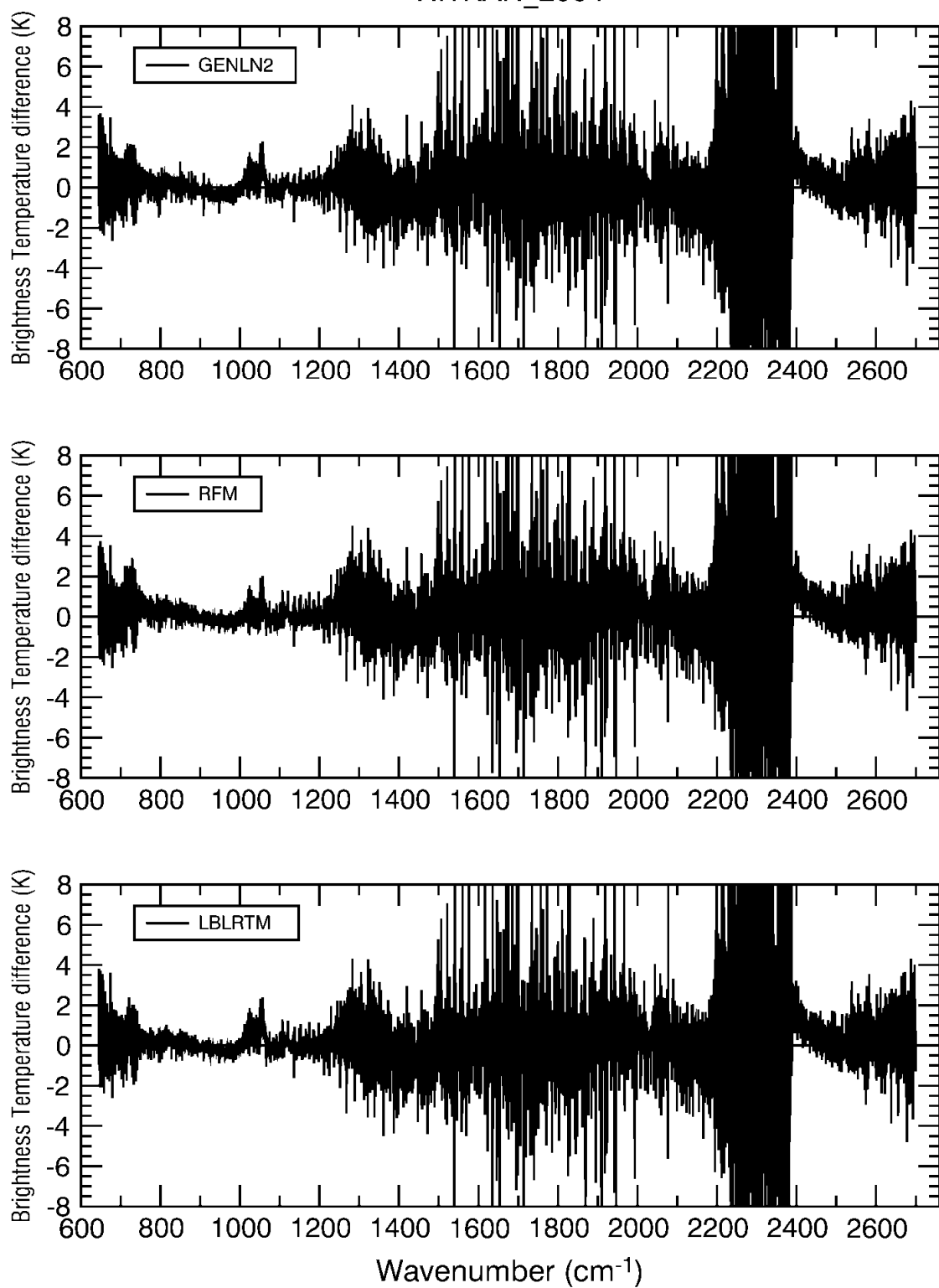


Figure 26: Radiance residuals between calculated and measured radiance for NAST-I. Calculated radiances were obtained using the HITRAN2004 molecular database.

# CAMEX-III

GEISA\_2003

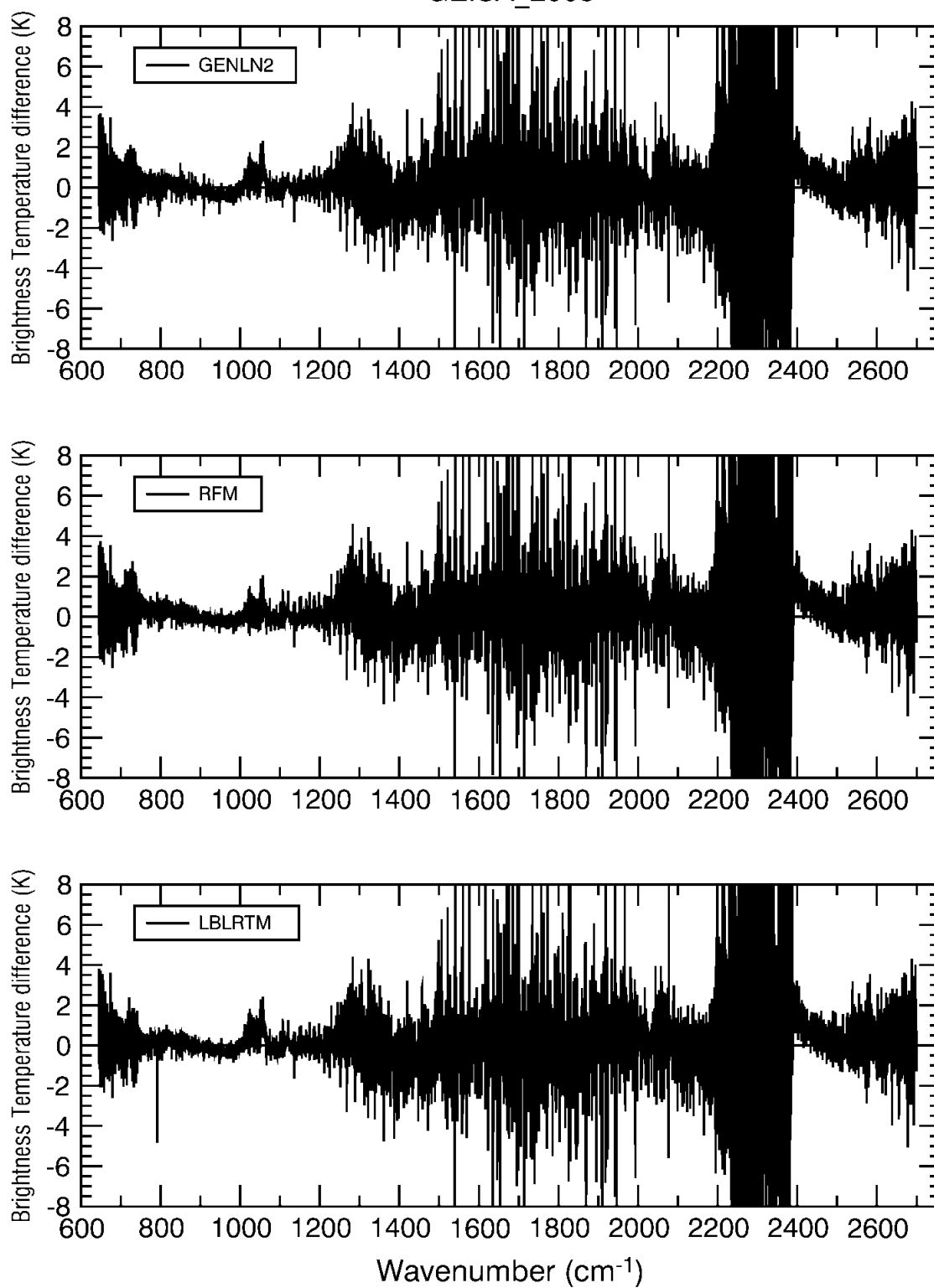


Figure 27: Radiance residuals between calculated and measured radiance for NAST-I. Calculated radiances were obtained using the GEISA2003 molecular database.

In Figures 28, 29 and 30 we show the bias and rms of the difference between the simulated and measured radiance over intervals of width  $50\text{ cm}^{-1}$ .

From the figures we can observe a peak in the rms curves around  $740\text{ cm}^{-1}$  showing that as discussed in the previous section there are problems in simulating the high frequency branch of  $\text{CO}_2$   $\nu_2$  band. In this region GENLN2 and LBLRTM seem to capture the absorption of  $\text{CO}_2/\text{H}_2\text{O}$  better than RFM. In the  $645$  to  $1000\text{ cm}^{-1}$  region the LBLRTM rms error is consistently lower than the RFM and GENLN2 error. In the ozone band the situation is reversed with RFM capturing the  $\text{O}_3$  absorption better than GENLN2 and LBLRTM. A local rms maximum is seen around  $1320\text{ cm}^{-1}$ , a spectral region where a large number of water vapour and methane lines are present. In this region GENLN2 appears to be in better agreement with observations. In terms of bias better results are obtained by each code in different spectral ranges across the water vapour band. However, it is noticeable how the GENLN2 bias in the  $1900$  to  $2200\text{ cm}^{-1}$  region is significantly lower than the RFM and LBLRTM bias. As observed in the previous sections, this is a region where the water continuum coefficients used in GENLN2 differ from those used in RFM and LBLRTM. The sharp increase/decrease in rms above  $1500\text{ cm}^{-1}$  occurs in a region where the radiometric noise, expressed in terms of noise-equivalent-delta-temperature (NEDT) at a blackbody temperature equal to the actual temperature of the scene, is sharply increasing/decreasing. It is worth noticing that while values of the bias are almost everywhere below the radiometric noise, the rms values are in fact consistently above the noise.

The different choice of line parameters does appear to have a limited impact on the residuals, with exceptions in the ozone band, where the use of HITRAN2004 and GEISA2003 results in larger values of the bias and rms. Computations for LBLRTM show that the use of the GEISA2003 parameters still results in larger values of the bias and rms between  $750$  and  $850\text{ cm}^{-1}$ .

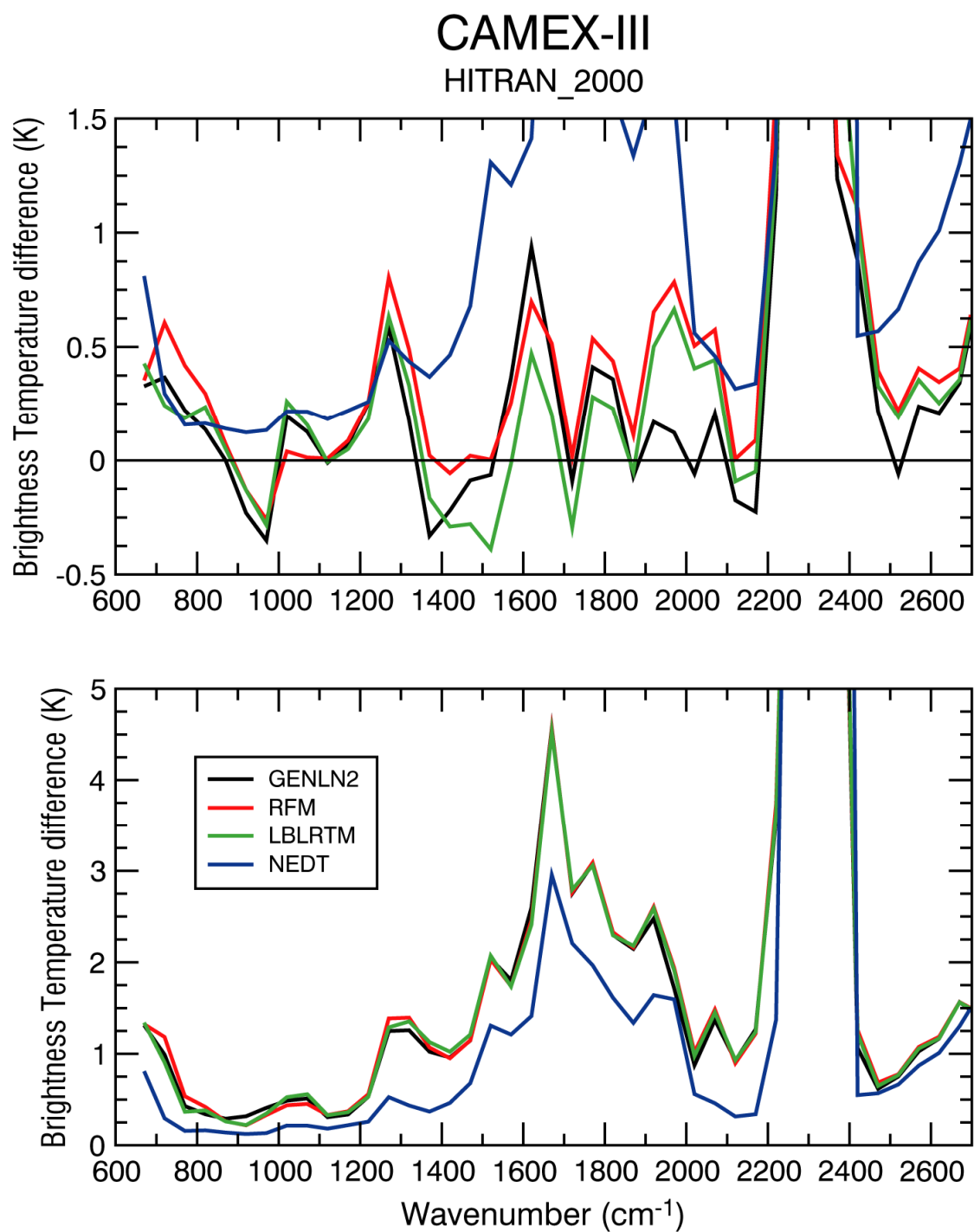


Figure 28: Bias (upper panel) and root-mean-square-error (lower panel) of the difference between simulated and measured spectra for the CAMEX-III case. Values for NAST-I band 1, band 2 and band 3 are computed over intervals of 50 cm<sup>-1</sup> using the HITRAN2000 molecular database.

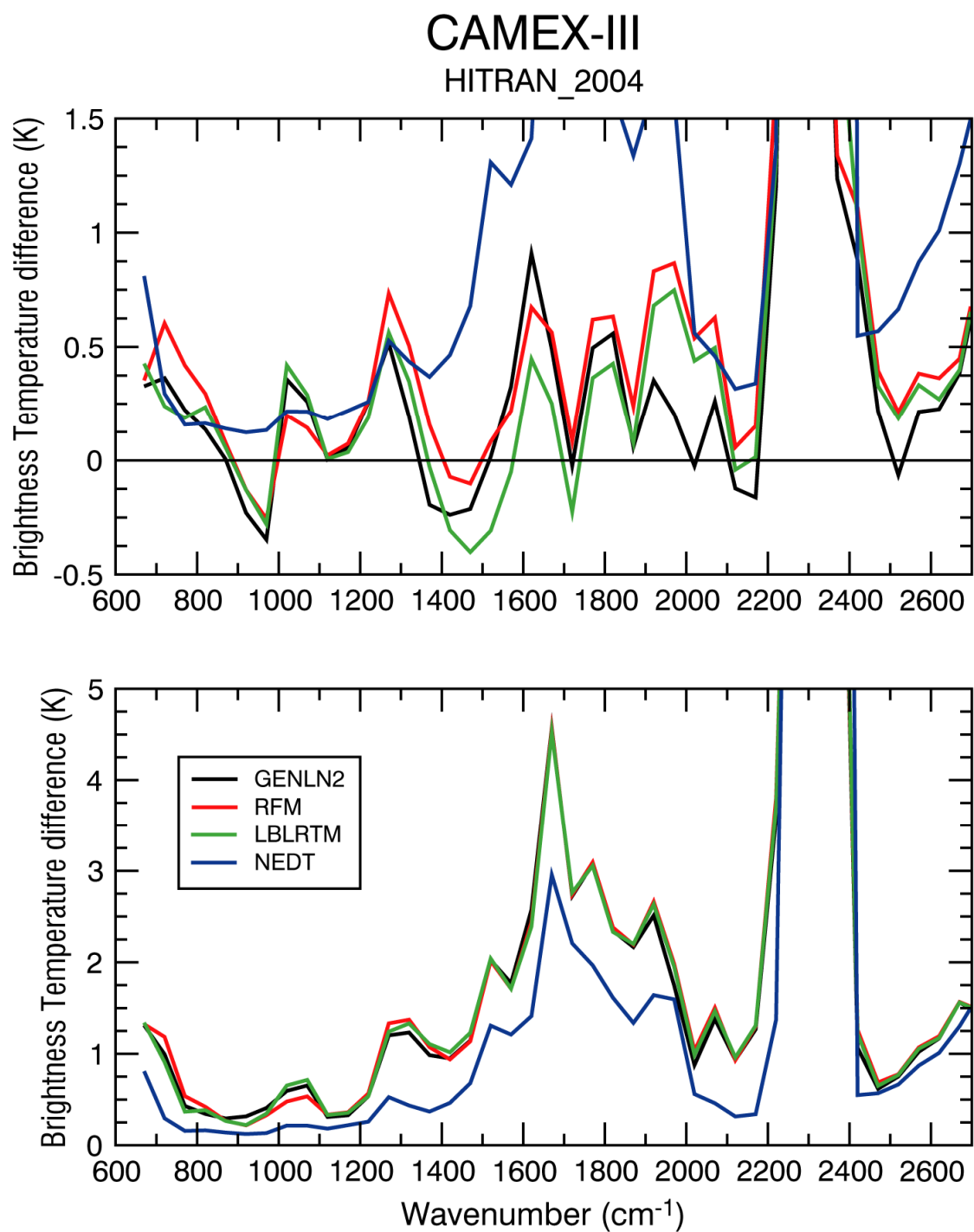


Figure 29: Bias (upper panel) and root-mean-square-error (lower panel) of the difference between simulated and measured spectra for the CAMEX-III case. Values for NAST-I band 1, band 2 and band 3 are computed over intervals of 50 cm<sup>-1</sup> using the HITRAN2004 molecular database.

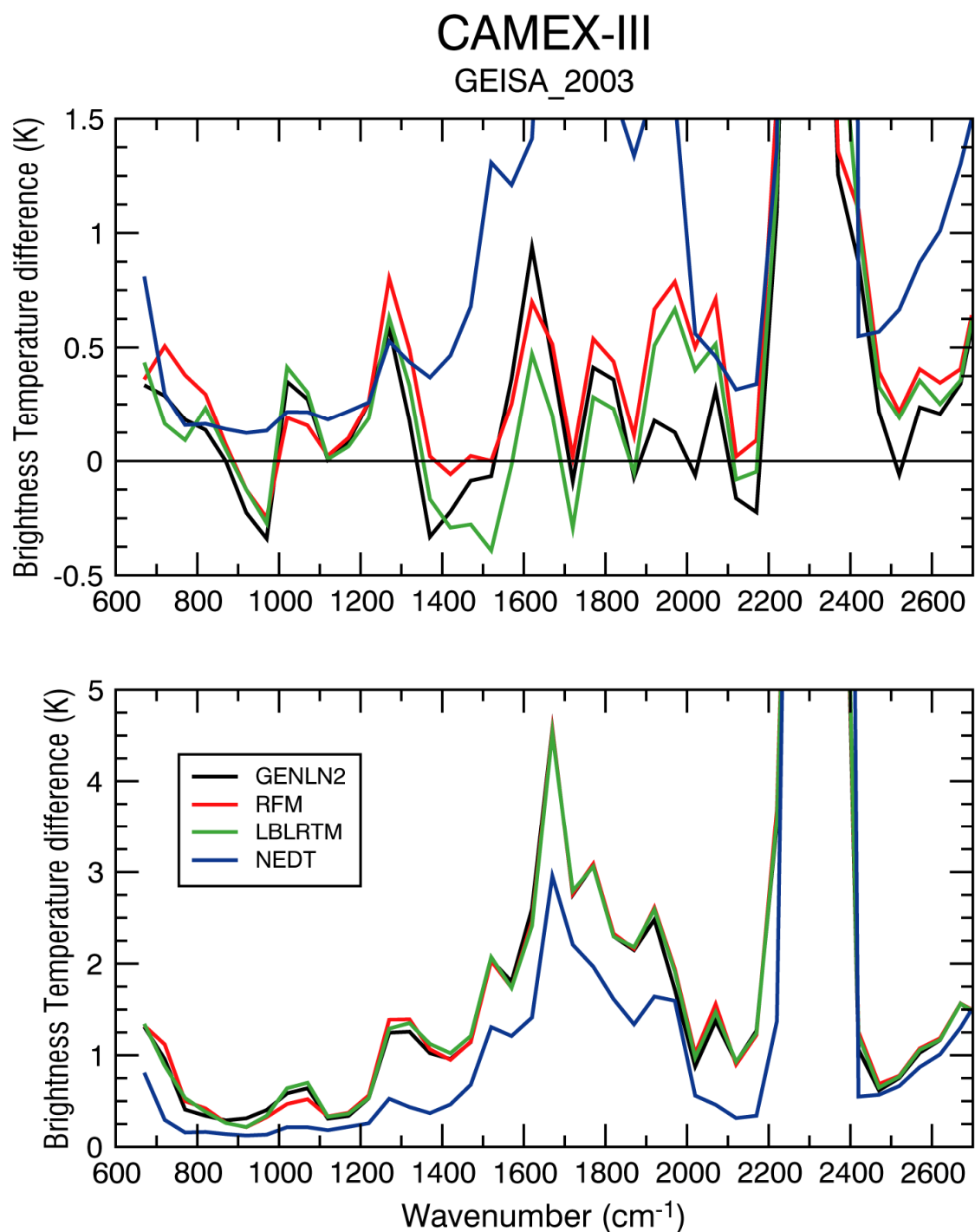


Figure 30: Bias (upper panel) and root-mean-square-error (lower panel) of the difference between simulated and measured spectra for the CAMEX-III case. Values for NAST-I band 1, band 2 and band 3 are computed over intervals of  $50 \text{ cm}^{-1}$  using the GEISA2005 molecular database.

In figure 31 we have plotted the radiance residuals between radiances that have been calculated using the GEISA20003 and HITRAN2004 databases using the RFM model. Results shown in Figures 32 33 and 34 suggest that the impact resulting from the use of different line parameters is very small. The

only noticeable feature is the larger error in the ozone band when the HITRAN2004 and GEISA2003 parameters are used. Unfortunately, because of the large radiometric noise is not possible to make an estimate of the impact of the discrepancies observed at  $2230\text{ cm}^{-1}$ .

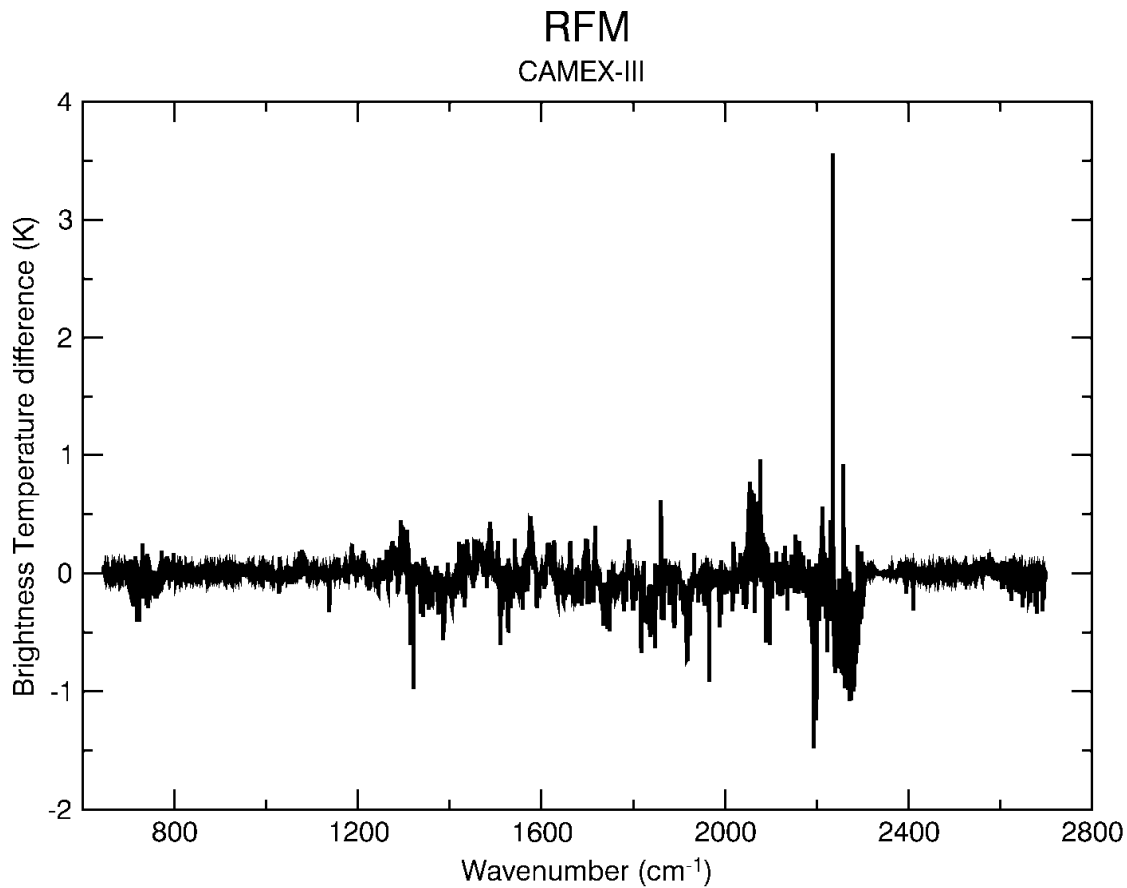


Figure 31: Radiance residuals between radiances calculated using the GEISA2003 database and radiances calculated using the HITRAN2004 database. Spectra are computed using the RFM model.

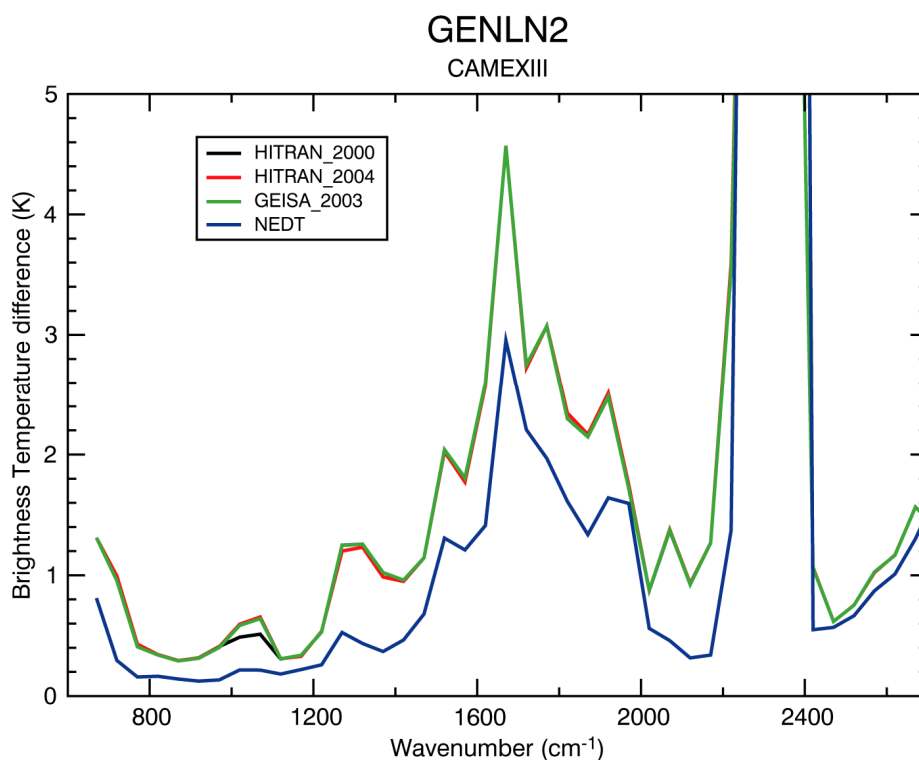


Figure 32: Root-mean-square-error of the difference between simulated and measured spectra for the CAMEX-III case. Spectra are computed using the GENLN2 model utilizing the HITRAN2000, HITRAN2004 and GEISA2003 molecular databases.

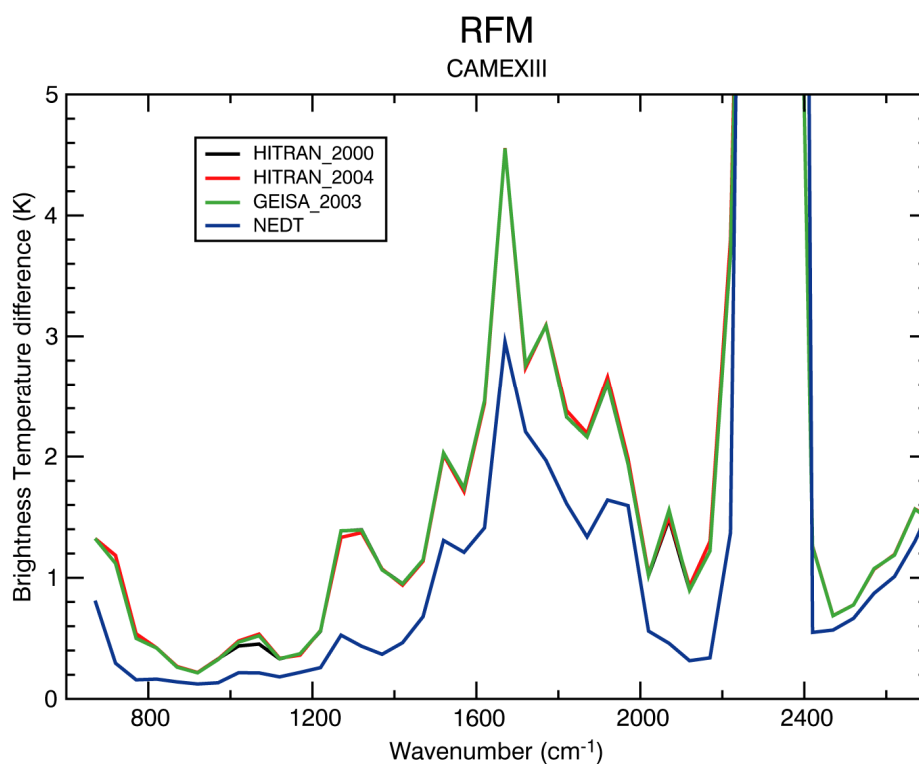


Figure 33: Root-mean-square-error of the difference between simulated and measured spectra for the CAMEX-III case. Spectra are computed using the RFM model utilizing the HITRAN2000, HITRAN2004 and GEISA2003 molecular databases.

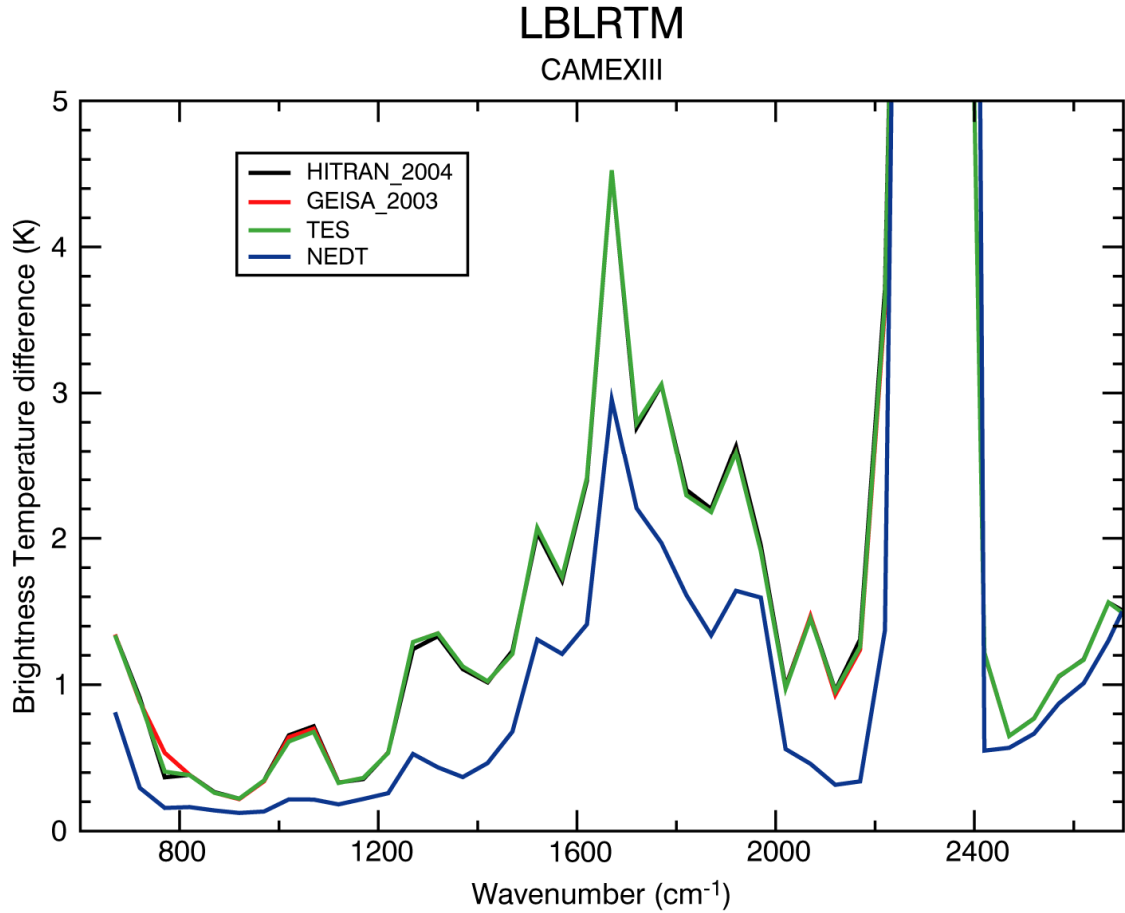


Figure 34: Root-mean-square-error of the difference between simulated and measured spectra for the CAMEX-III case. Spectra are computed using the LBLRTM model utilizing the HITRAN2000, HITRAN2004 and GEISA2003 molecular databases.

In figure 35 we have plotted the rms of the difference between simulated radiances. It can be seen that rms values are smaller than rms values obtained when the differences between simulations and observations are plotted. It has already been observed that this is an indication of the fact that errors are predominantly of spectroscopic nature. However, in the regions where larger local maxima are attained other contributions to the error cannot be ruled out. The peaks at 750, 1600 and 2000 cm<sup>-1</sup> are likely to be related to the different implementation of the CO<sub>2</sub> line mixing and the different water continuum model.

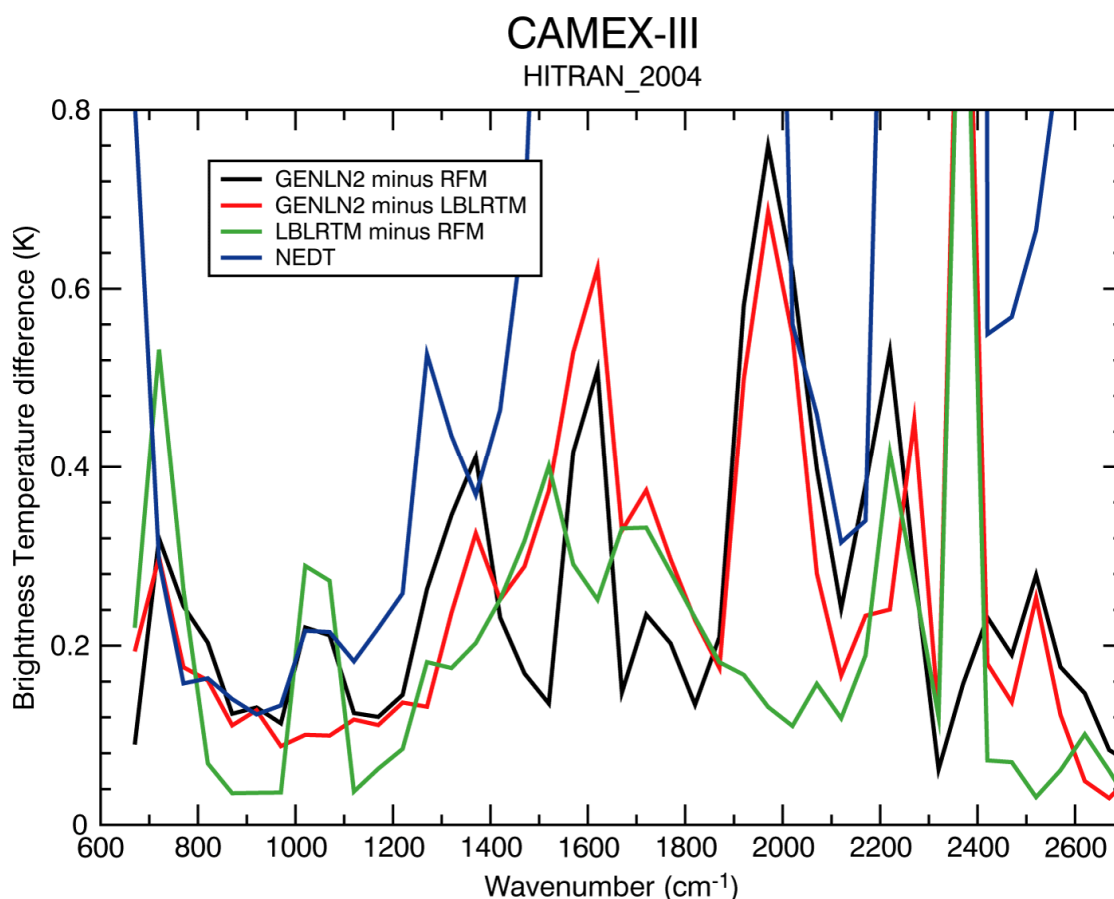


Figure 35: Root-mean-square-error of the difference between simulated spectra for the CAMEX-III case.

## Results for EAQUATE case

For the EAQUATE case we have used the surface emissivity retrieved by Masiello et al. (1996) in conjunction with inverted profiles of temperature and water vapour. The value of the skin temperature was set to 282.35K and computations were performed at an angle of  $7.5^\circ$  off nadir. As in the previous cases we used the same atmospheric layering adjusting the pressure levels at surface and at flight altitude. The mixing ratio values adopted for a selected number of trace gas species are tabulated in table 6. As for the CAMEX-III case the spectrum used in this study is a single measurement spectrum and the measurement error consists only of the radiometric noise. Again, it is unfortunate that between 2200 and 2400  $\text{cm}^{-1}$  the level of noise is such to render impossible any comparison between measured and computed radiances.

Table 6: Volume mixing ratio for selected gaseous species

Specie	ppmv
CO <sub>2</sub>	371.6
CH <sub>4</sub>	1.89
N <sub>2</sub> O	0.318
CFC-11	$2.51 \text{ E}^{-4}$
CFC-12	$5.43 \text{ E}^{-4}$
CCL <sub>4</sub>	$9.29 \text{ E}^{-5}$

Results for this case convey on the whole the same information obtained from the CAMEX-III case; hence we will not go in any further detailed discussion of the results. We will discuss here only three

noticeable features. The first feature is that the values of the bias for RFM are significantly higher than the values of the bias for LBLRTM and GENLN2 in the 650 to 750  $\text{cm}^{-1}$  region. The third feature is that the use of GEISA2003 line parameters appear to slightly reduce errors in the 1900  $\text{cm}^{-1}$  region whereas the use of the HITRAN2004 line parameters slightly reduce errors in the 1400  $\text{cm}^{-1}$  region. The radiance residuals between simulated and measured radiances are plotted in figures 36, 37 and 38 for the HITRAN2000, HITRAN2004 and GEISA2003 cases respectively and the average bias and the rms error of the difference between simulated and measured radiances are plotted in figures 39, 40 and 41. In figures 42, 43 and 44 we plot the rms error of the difference between simulated and measured radiances for GENLN2, RFM and LBLRTM using different line parameters. In figure 45 we plot the radiance residuals between radiances calculated using the GEISA2003 and HITRAN2004 database and finally in figure 46 we plot the rms error of the difference between the radiances simulated by the various model involved in this study.

# EAQUATE

HITRAN\_2000

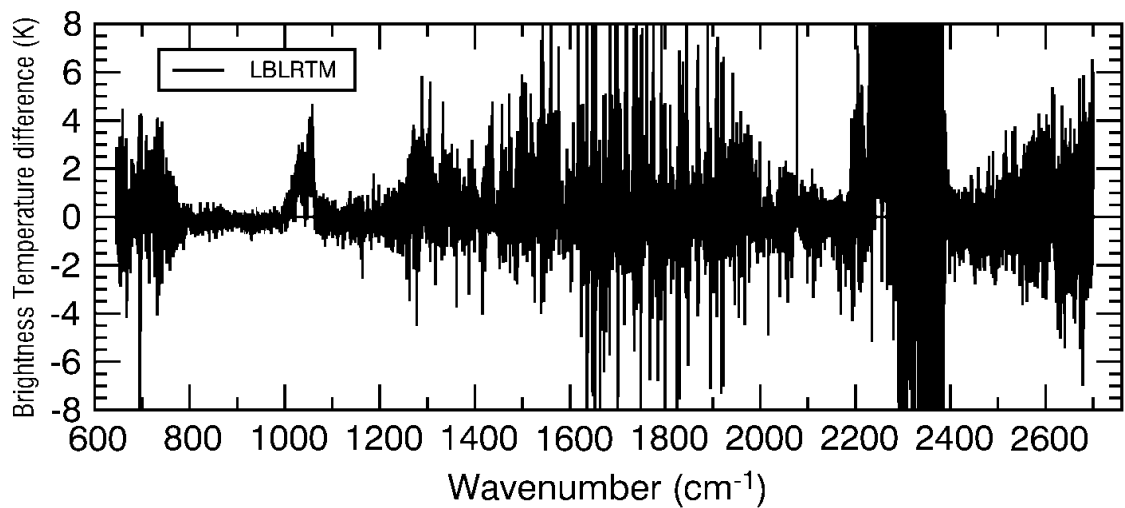
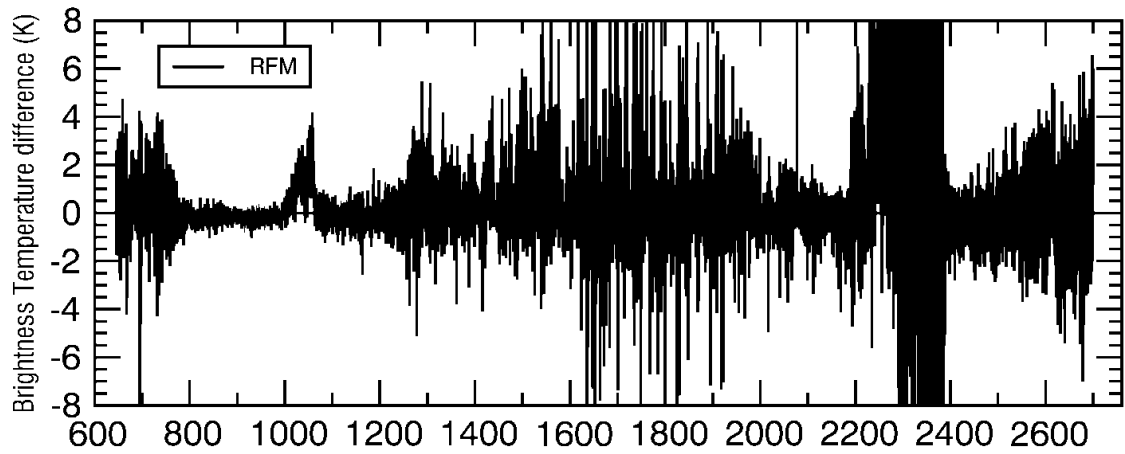
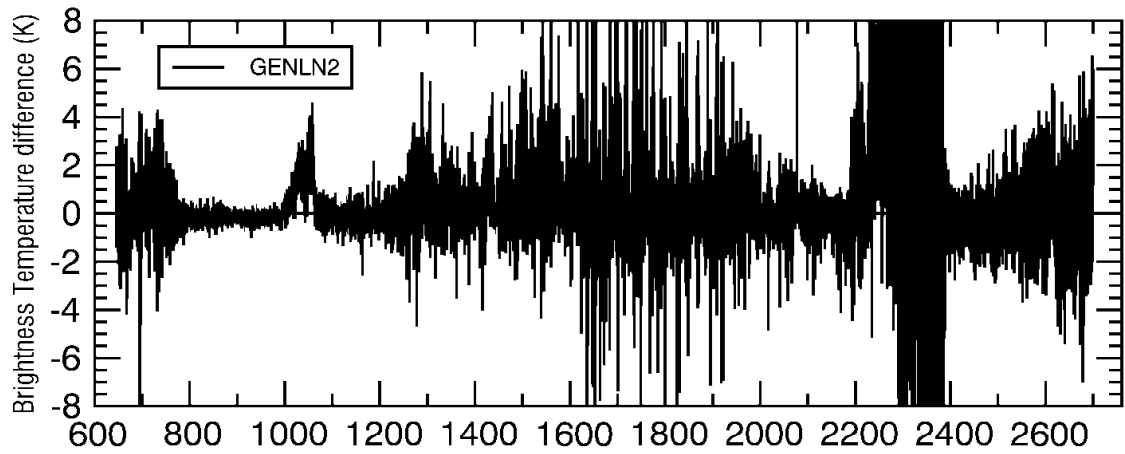
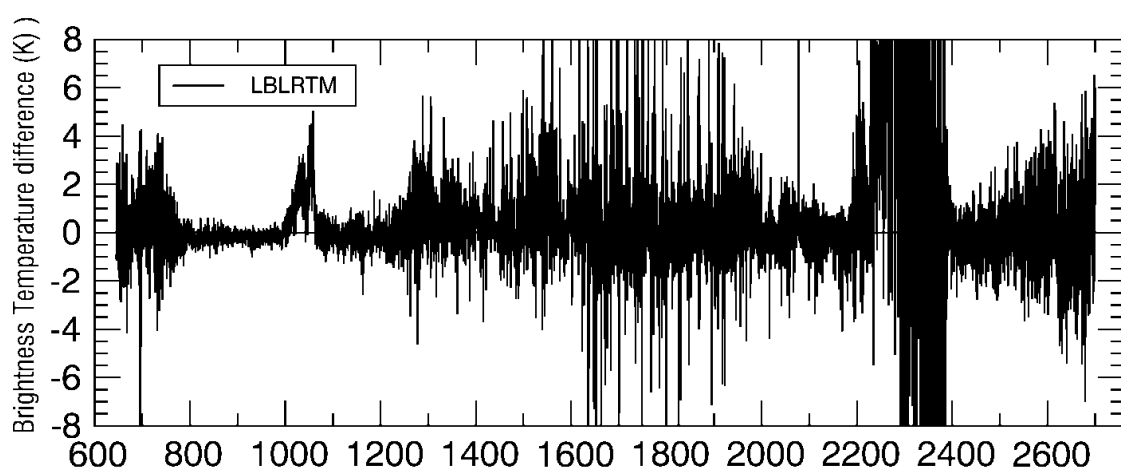
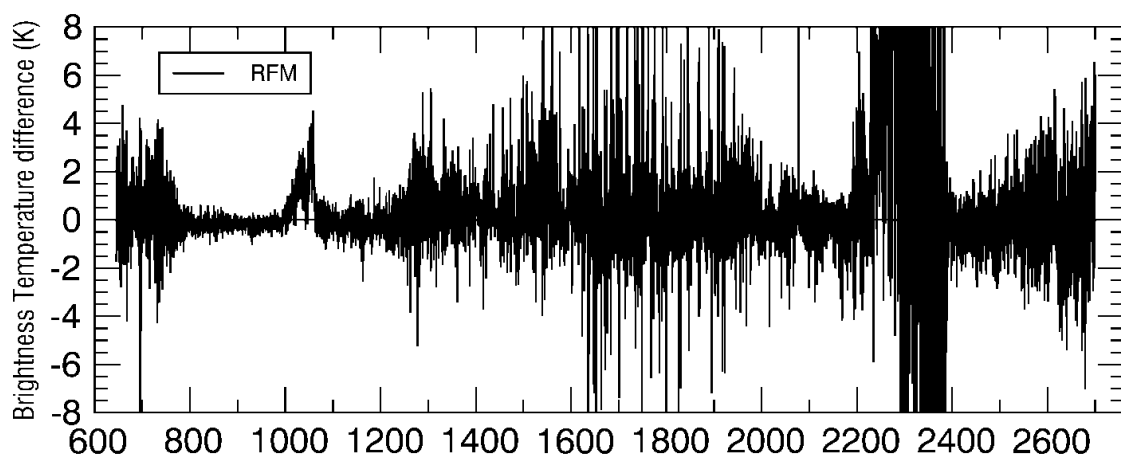
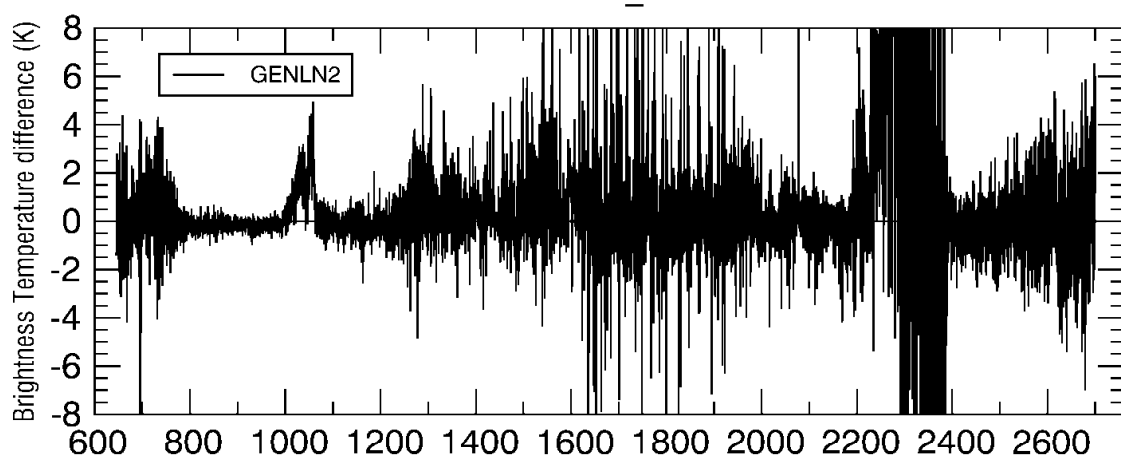


Figure 36: Radiance residuals between calculated and measured radiance for NAST-I. Calculated radiances were obtained using the HITRAN2000 molecular database.

# EAQUATE

HITRAN\_2004



Wavenumber (cm<sup>-1</sup>)

Figure 37: Radiance residuals between calculated and measured radiance for NAST-I. Calculated radiances were obtained using the HITRAN2004 molecular database.

# EAQUATE

GEISA\_2003

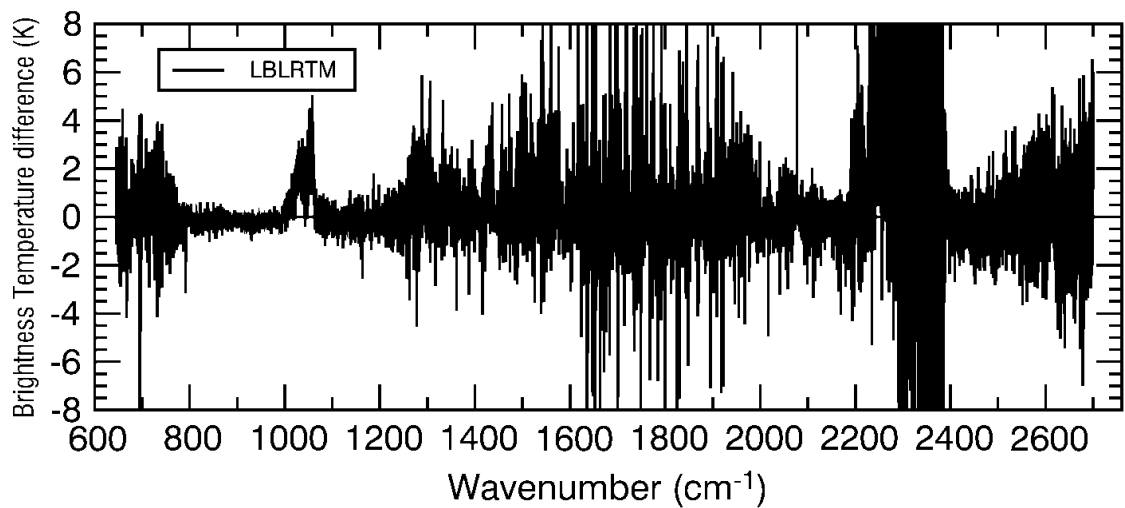
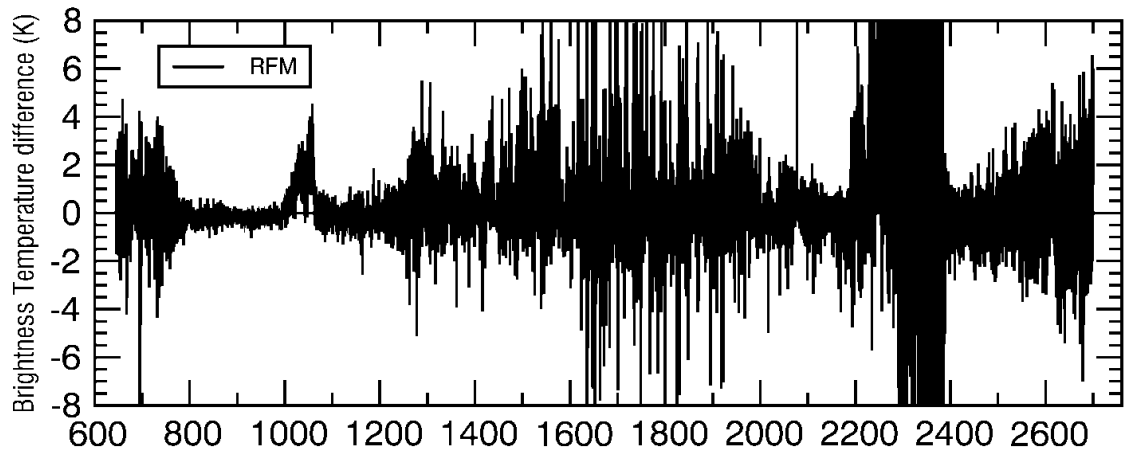
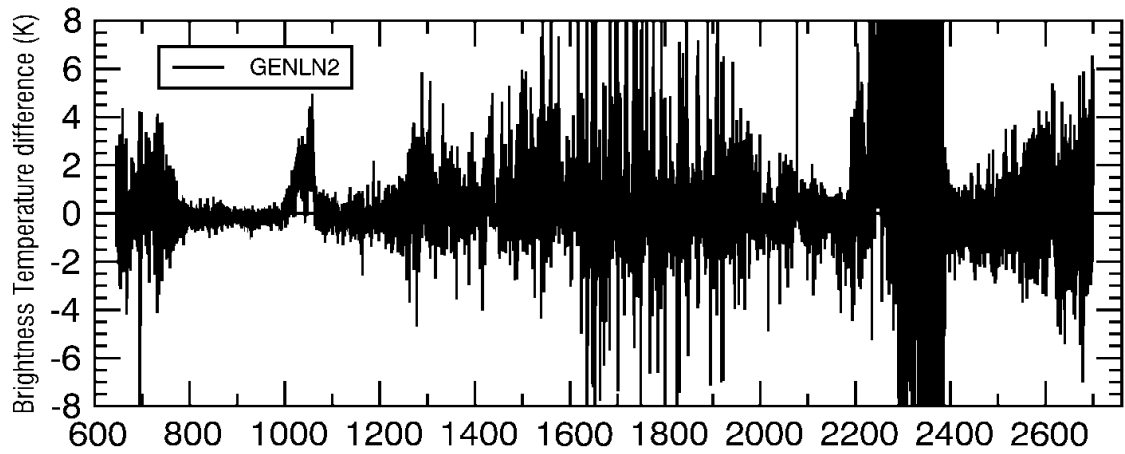


Figure 38: Radiance residuals between calculated and measured radiance for NAST-I. Calculated radiances were obtained using the HITRAN2000 molecular database.

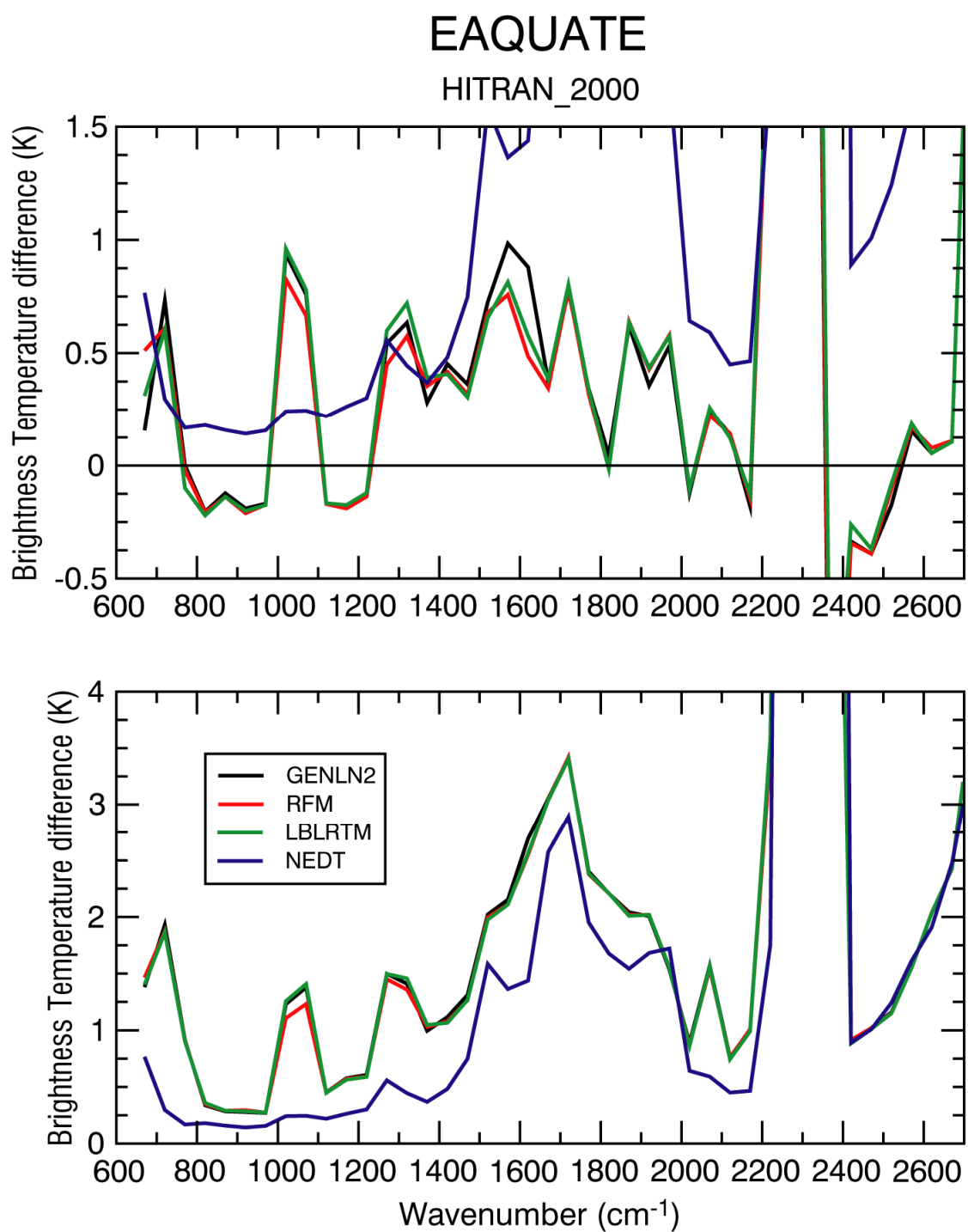


Figure 39: Bias (upper panel) and root-mean-square-error (lower panel) of the difference between simulated and measured spectra for the EAQUATE case. Values for NAST-I band 1, band 2 and band 3 are computed over intervals of 50 cm<sup>-1</sup> using the HITRAN2000 molecular database.

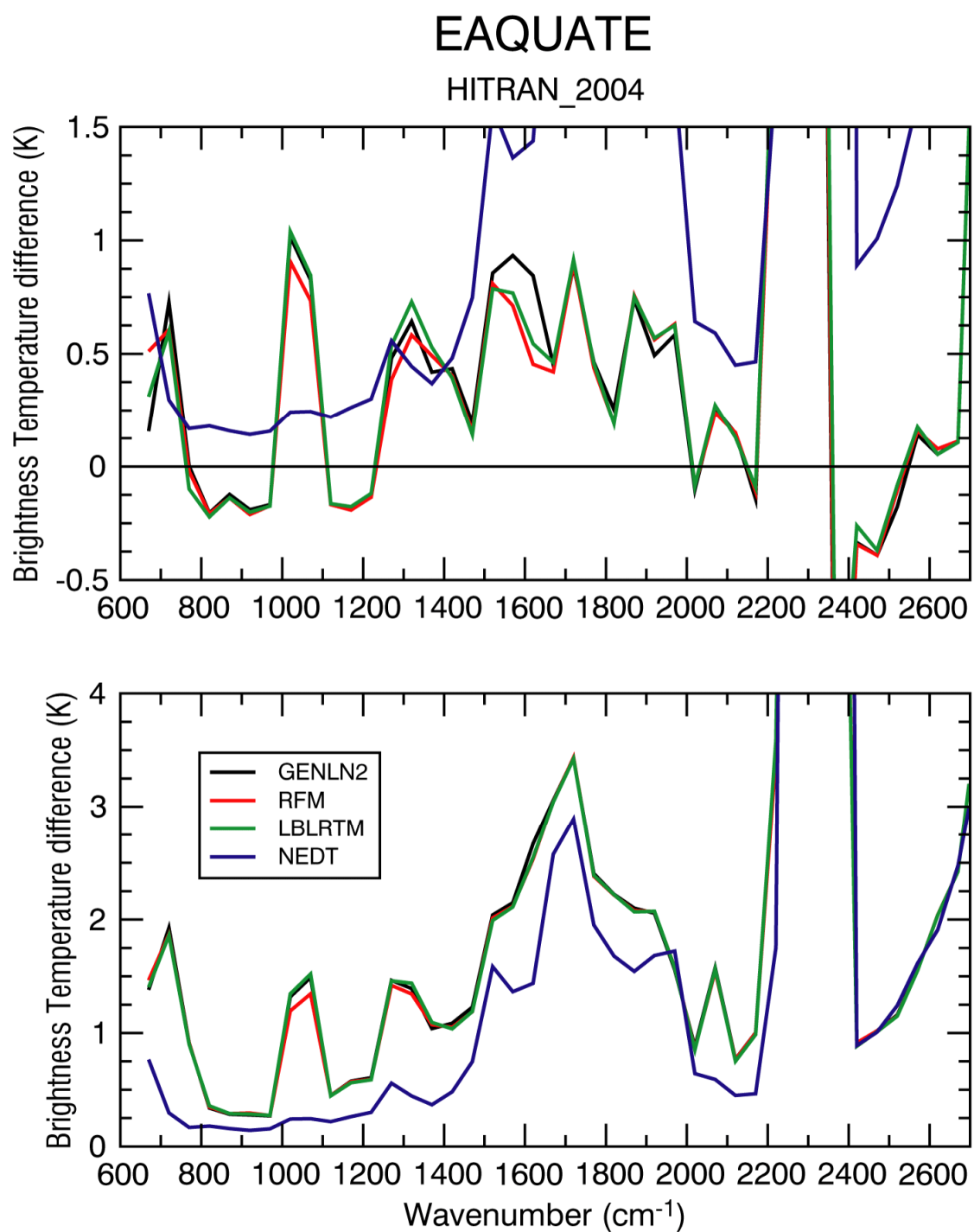


Figure 40: Bias (upper panel) and root-mean-square-error (lower panel) of the difference between simulated and measured spectra for the EAQUATE case. Values for NAST-I band 1, band 2 and band 3 are computed over intervals of  $50 \text{ cm}^{-1}$  using the HITRAN2004 molecular database.

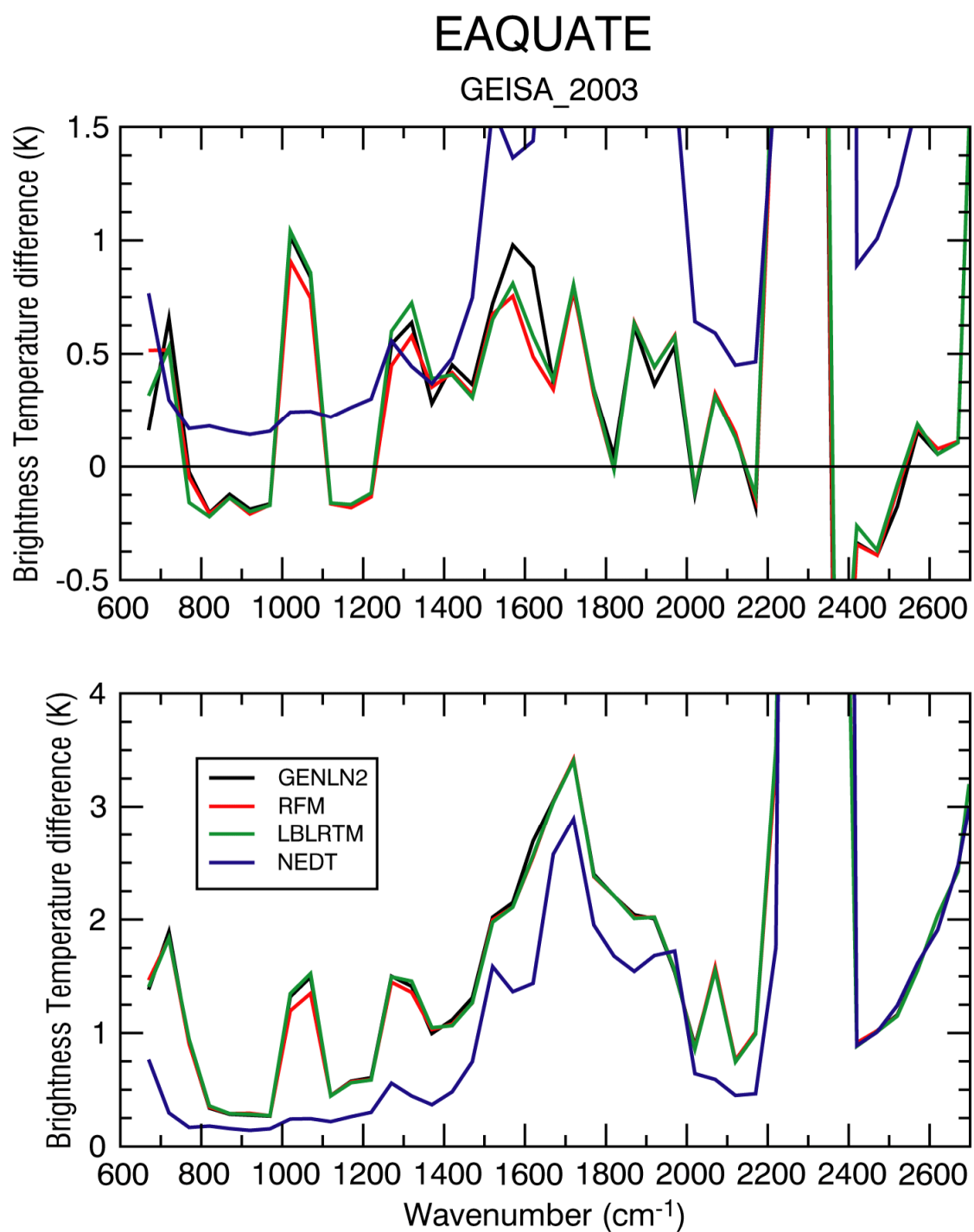


Figure 41: Bias (upper panel) and root-mean-square-error (lower panel) of the difference between simulated and measured spectra for the EAQUATE case. Values for NAST-I band 1, band 2 and band 3 are computed over intervals of  $50 \text{ cm}^{-1}$  using the GEISA2003 molecular database.

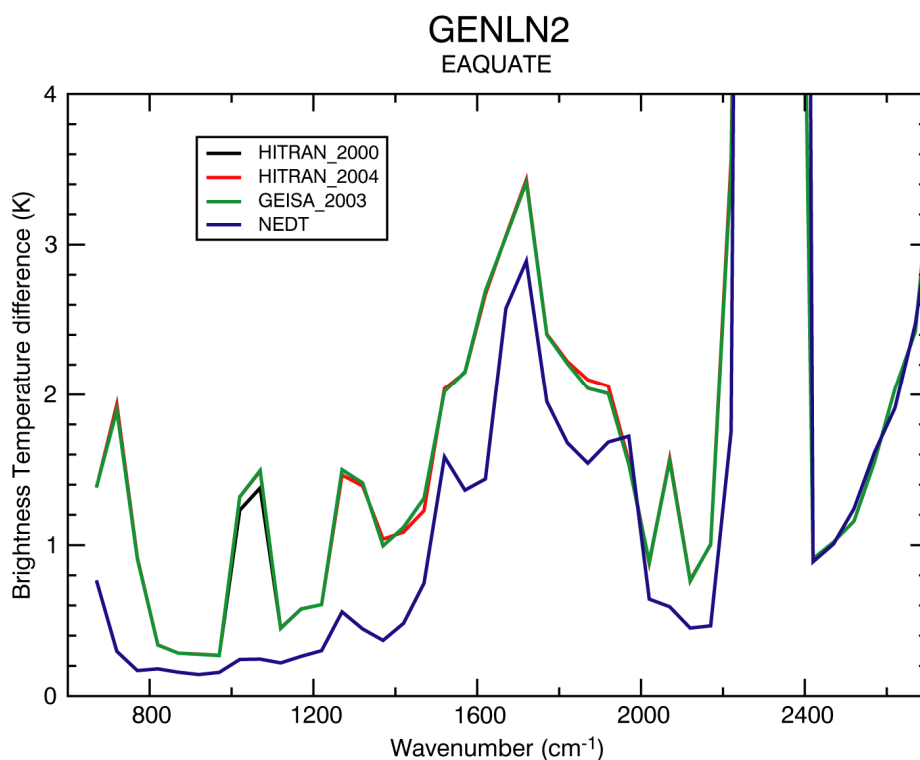


Figure 42: Root-mean-square-error of the difference between simulated and measured spectra for the EAQUATE case. Spectra are computed using the GENLN2 model utilizing the HITRAN2000, HITRAN2004 and GEISA2003 molecular databases.

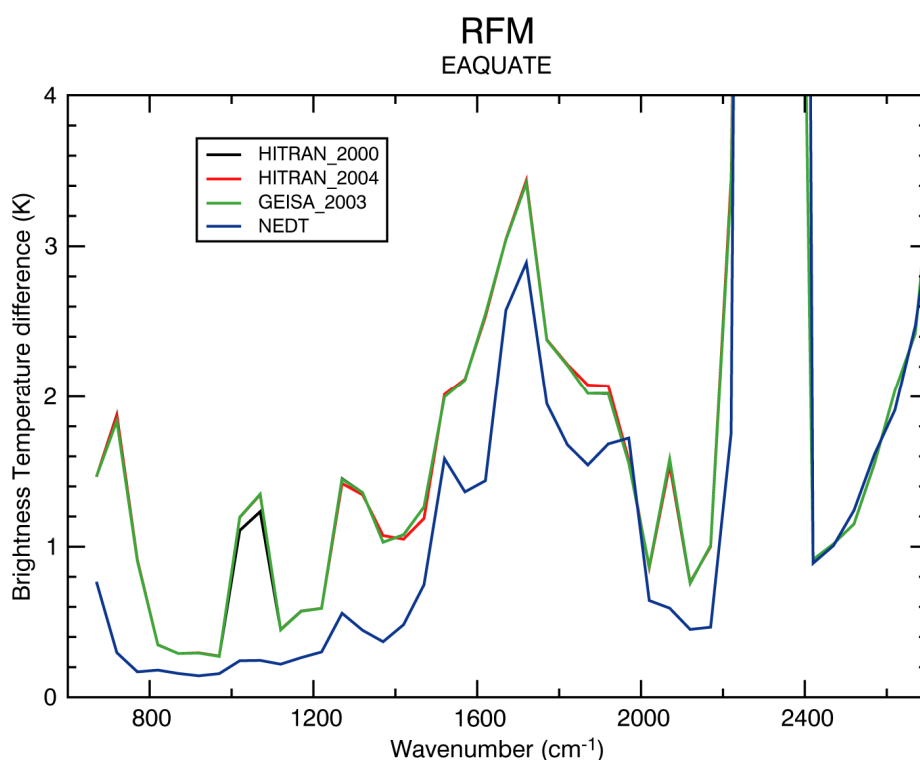


Figure 43: Root-mean-square-error of the difference between simulated and measured spectra for the EAQUATE case. Spectra are computed using the GENLN2 model utilizing the HITRAN2000, HITRAN2004 and GEISA2003 molecular databases.

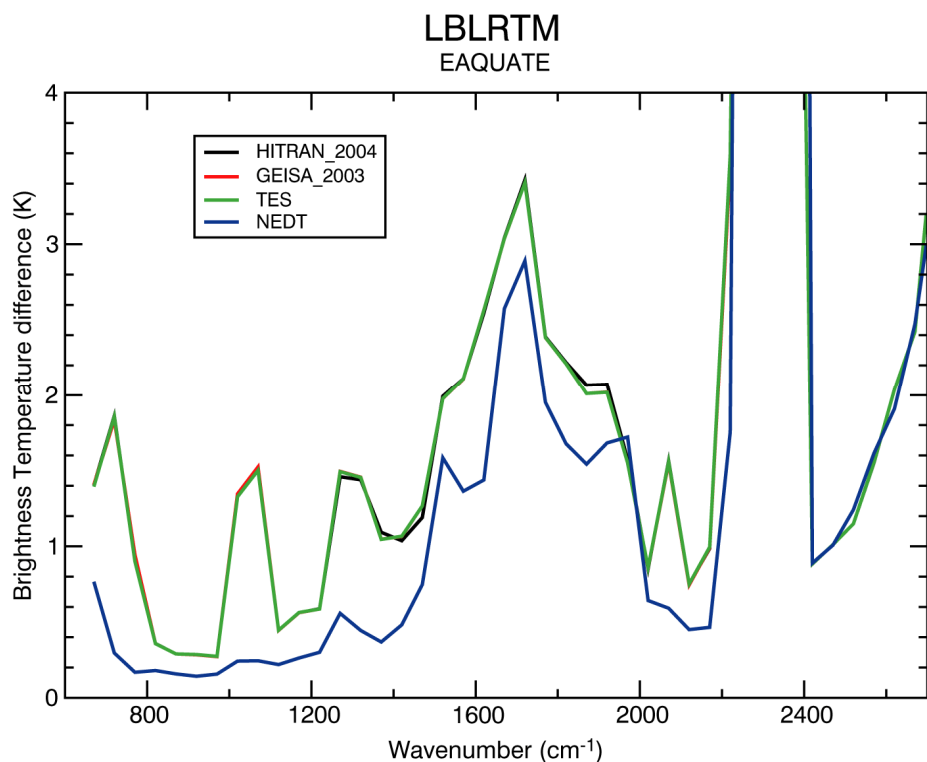


Figure 44: Root-mean-square-error of the difference between simulated and measured spectra for the EAQUATE case. Spectra are computed using the GENLN2 model utilizing the HITRAN2000, HITRAN2004 and GEISA2003 molecular databases.

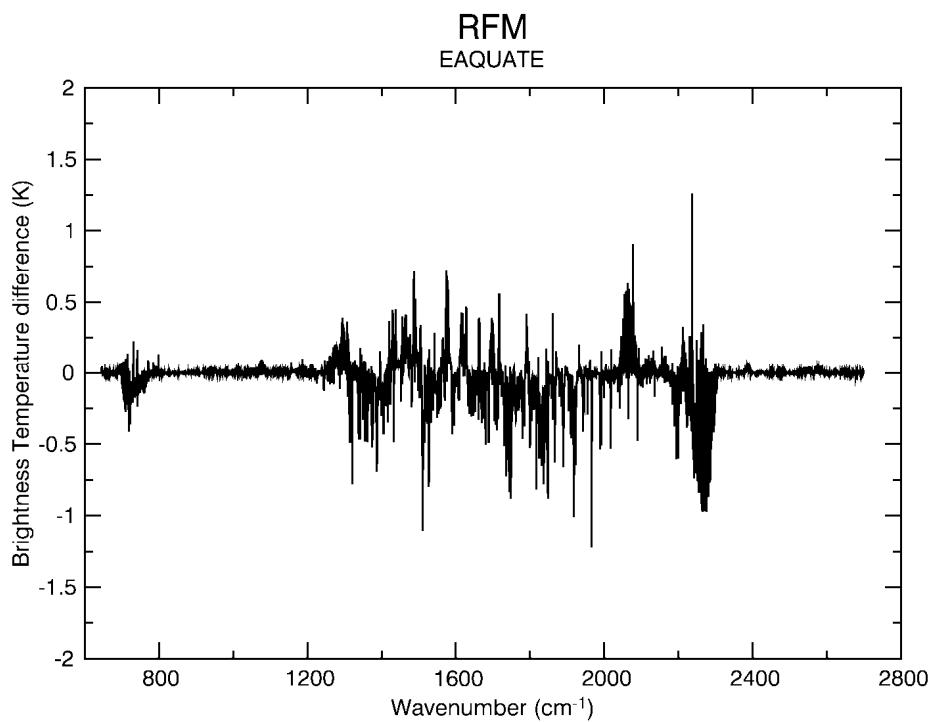


Figure 45: Radiance residuals between radiances calculated using the GEISA2003 database and radiances calculated using the HITRAN2004 database. Spectra are computed using the RFM model.

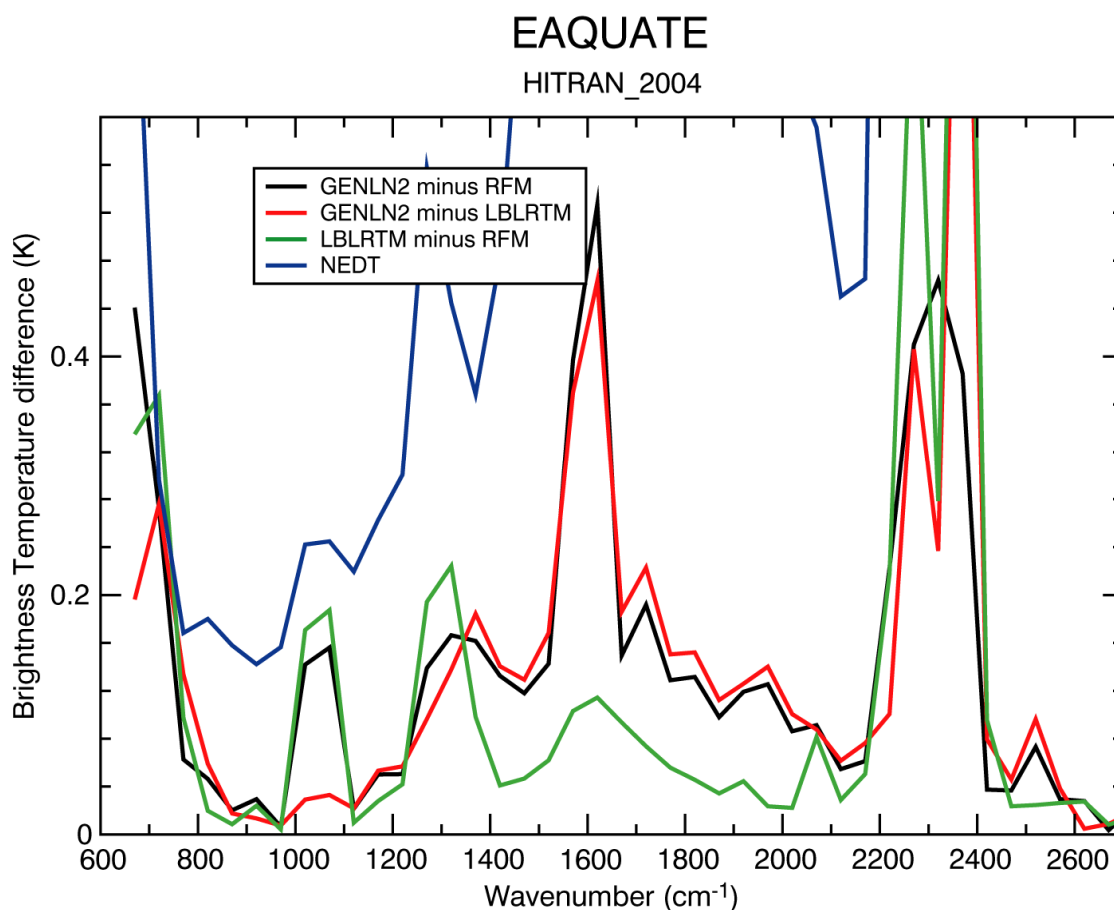


Figure 46: Root-mean-square-error of the difference between simulated spectra for the EAQUATE case.

## Results for MOTH case

For this case solar contamination is an issue. In fact most of the flights have been carried out in daytime, mainly for reasons of crew duty hours. One or two flights at night were available; however, these do not have the same level of collocated profile information. Consequently in our discussion of the results we will not include the spectral region beyond 2400 cm<sup>-1</sup>. As discussed in a previous section, in the 1200 to 2100 cm<sup>-1</sup> region, problems in the calibration of the interferometer can result in spikes in the observed radiance spectra. A number of channels were identified that displayed very large departures and were consequently removed from the spectrum. As in previous cases we have used spectral emissivity values obtained from the model by Masuda et al. (1988). The mixing ratio values adopted for a selected number of trace gas species are tabulated in table 7.

Table 7: Volume mixing ratio for selected gaseous species

Specie	Ppmv
CO2	365.6
CH4	1.73
N2O	0.315
CFC-11	2.61 E <sup>-4</sup>
CFC-12	5.41 E <sup>-4</sup>
CCL4	9.8 E <sup>-5</sup>

It should be noted that when compared to the previous cases, measurements by the ARIES instrument were taken at lower altitudes and the atmosphere was characterized by higher temperatures and a significantly higher water vapor burden.

From Figures 47, 48 and 49 it can be seen that the residuals show that in general a good level of agreement with observations is achieved by all models. Some scatter can be observed in the water vapor band that is likely to be caused by the calibration problems discussed above. Two features can be readily observed from the plots. The first feature is the better performance of LBLRTM in the 800 to 1000  $\text{cm}^{-1}$  window region. Since LBLRTM and RFM use the same model, it is unlikely that this behavior can be ascribed to the water vapour continuum. Instead it is most likely related to the fact that the surface reflection of down-welling thermal radiation is treated in LBLRTM using the diffusivity approximation whereas RFM and GENLN2 assume a specular surface. The second feature is that in the 1800 to 2200  $\text{cm}^{-1}$  region the behavior of GENLN2 deviates significantly from the behavior of RFM and LBLRTM. Results for RFM and LBLRTM are almost identical and this supports the hypothesis that differences can be ascribed to the water continuum model. Finally the spike observed for LBLRTM at 800  $\text{cm}^{-1}$  from the GEISA2003 case is likely related to the already mentioned inconsistency between line mixing coefficients and line parameters.

The average values of the bias and rms plotted in figures 50, 51 and 52 clearly points to a better performance of LBLRTM in the longwave window region. In the 1400  $\text{cm}^{-1}$  region GENLN2 has a smaller bias and a larger rms, whereas in the 2000  $\text{cm}^{-1}$  region the same code has a larger bias and larger rms. For GENLN2 a larger value of the bias is also observed around 1600  $\text{cm}^{-1}$ . In these two latter spectral regions results for GENLN are consistent with those observed in HIS and NAST-I cases. Also noticeable is the better performance in terms of bias and rms of RFM in the 1900 to 2100  $\text{cm}^{-1}$  region.

From figure 53 it can be seen that in the 1800 to 2000  $\text{cm}^{-1}$  region the use of GEISA2003 results in an increase of the rms. If we then look at the spectra computed using RFM and LBLRTM (figures 54 and 55), in the same region the use of GEISA2003 results in a decrease of the rms. From these figures it can also be seen that for all codes, in the 2250  $\text{cm}^{-1}$  region the use of the GEISA2003 line parameters results in a reduction of the rms. The same can be said for the region around 760  $\text{cm}^{-1}$  where a marginal reduction of the error is also observed. The spectrum shown in figure 56 supports the hypothesis that improvement in these two spectral regions are linked to the systematic nature of the residuals observed in the same regions.

Finally, figure 57 highlights the fact that GENLN2 results differ significantly from those obtained from RFM and LBLRTM in the 2000  $\text{cm}^{-1}$  region. Local maxima are also present in other regions but the magnitude is much smaller. We want also to note that in the 600 to 1400  $\text{cm}^{-1}$  region differences between GENLN2 and the other two models are comparable or even greater than differences between simulations and observations. Consequently it is very likely that these differences do not originate from the spectroscopy but rather from the computational procedures adopted by the three codes.

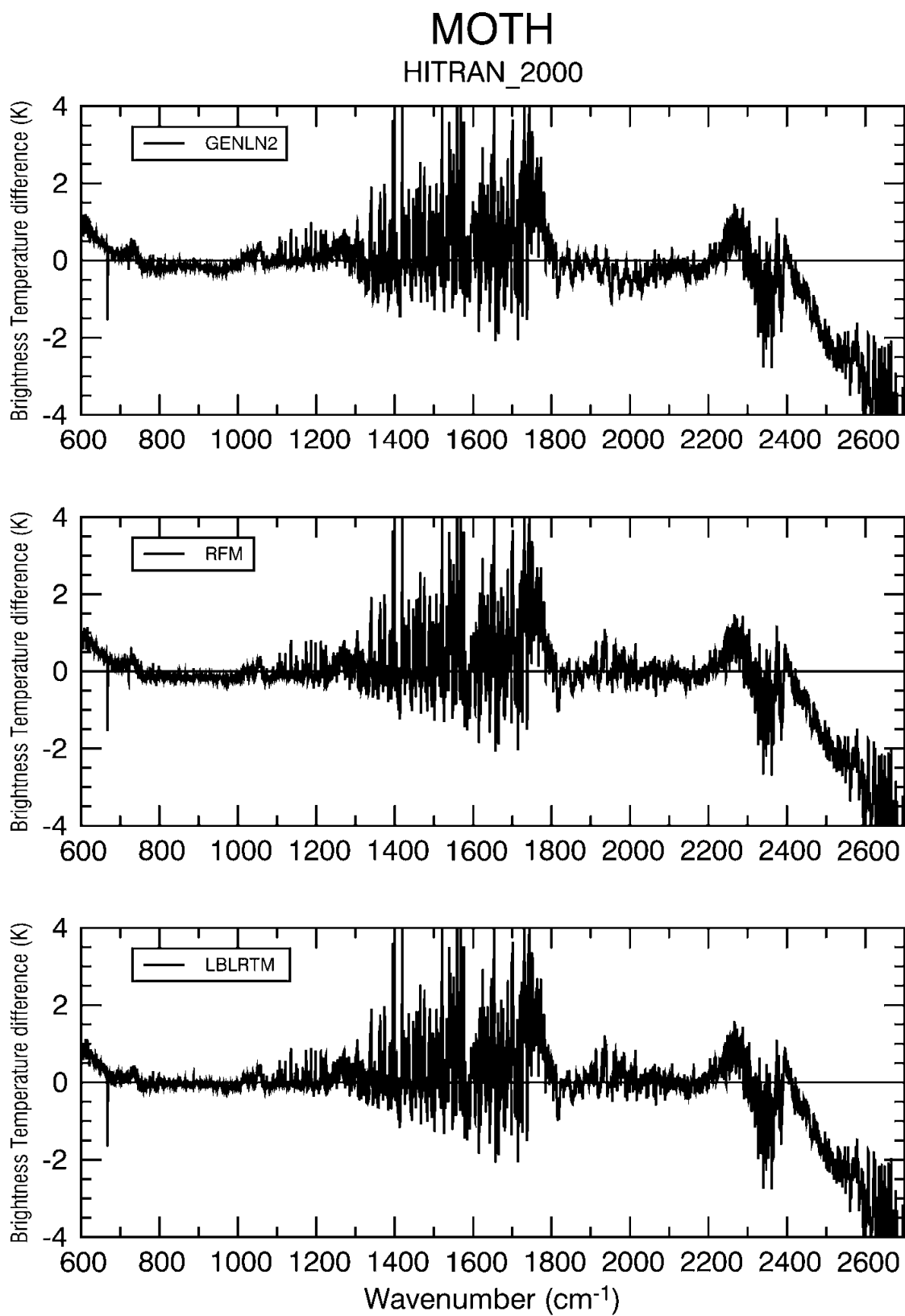


Figure 47: Radiance residuals between calculated and measured radiance for ARIES. Calculated radiances were obtained using the HITRAN2000 molecular database.

# MOTH

HITRAN\_2004

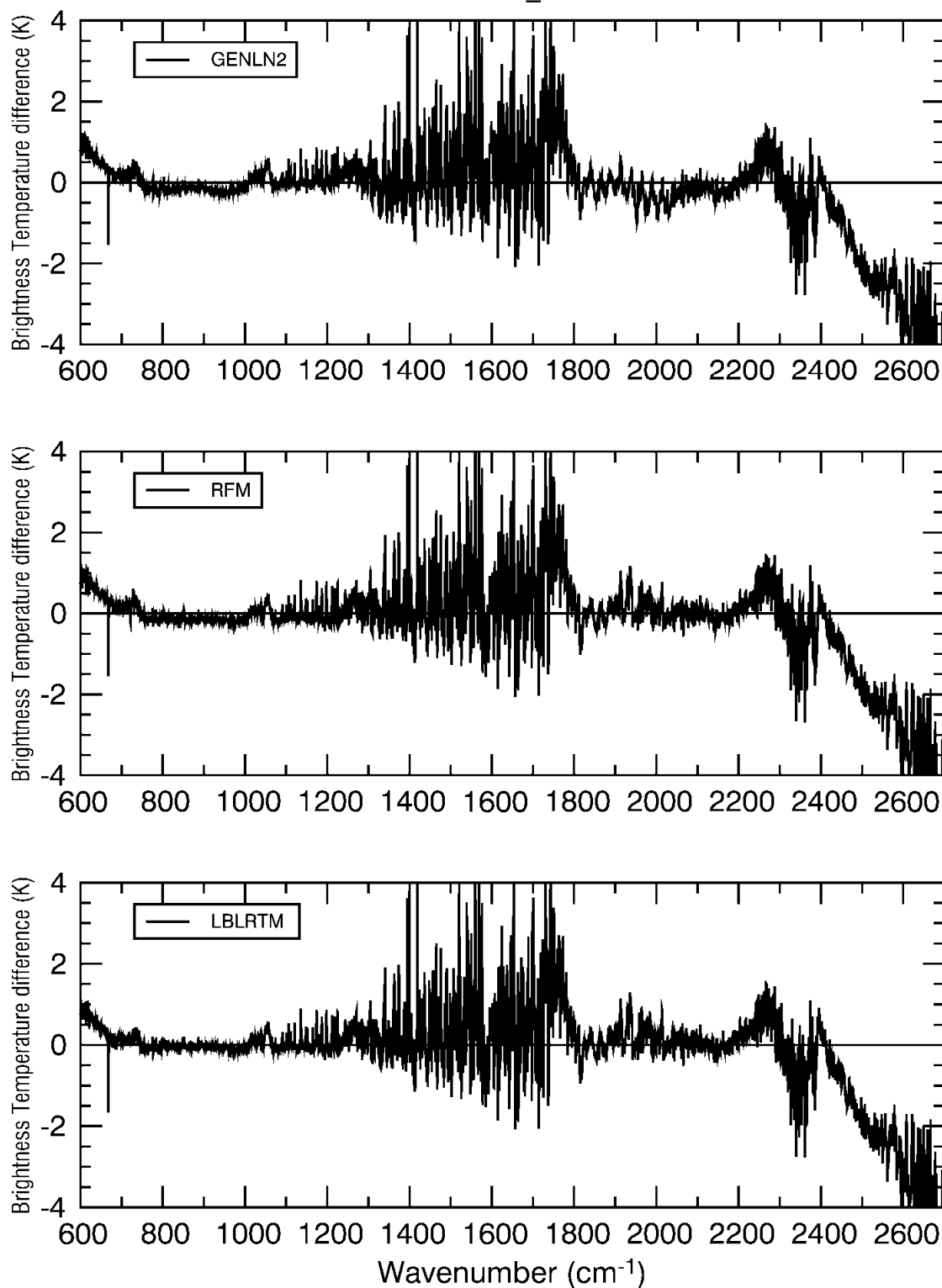


Figure 48: Radiance residuals between calculated and measured radiance for ARIES. Calculated radiances were obtained using the HITRAN2004 molecular database.

# MOTH

GEISA\_2003

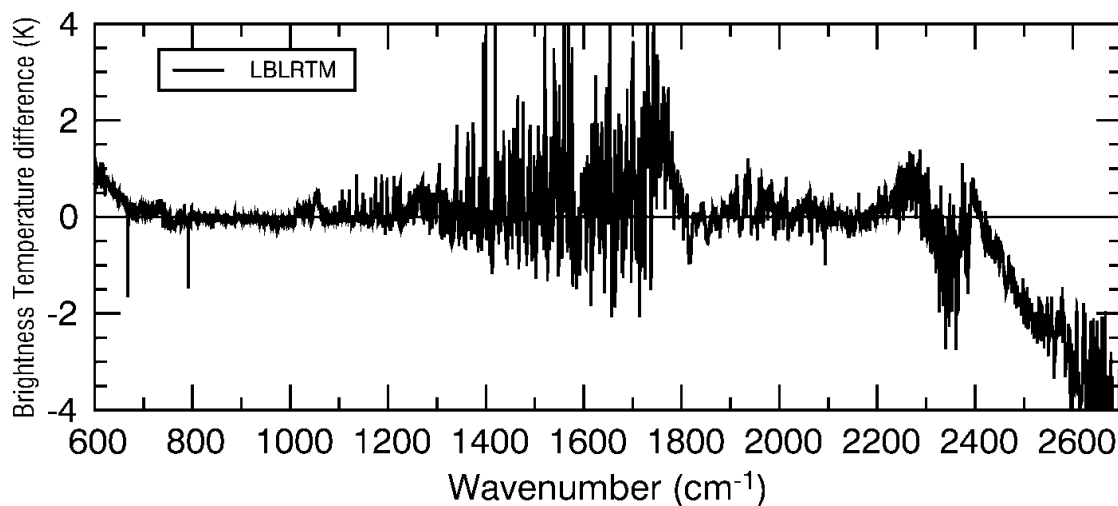
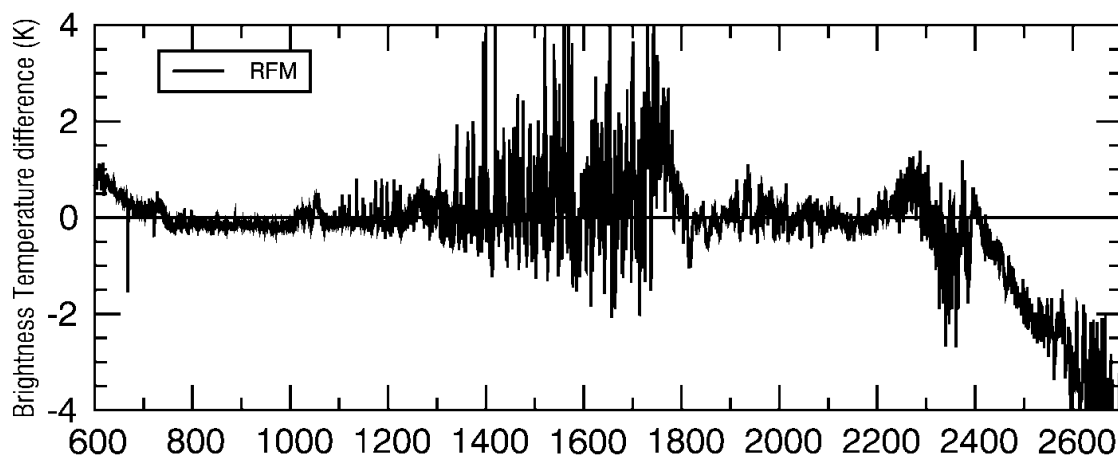
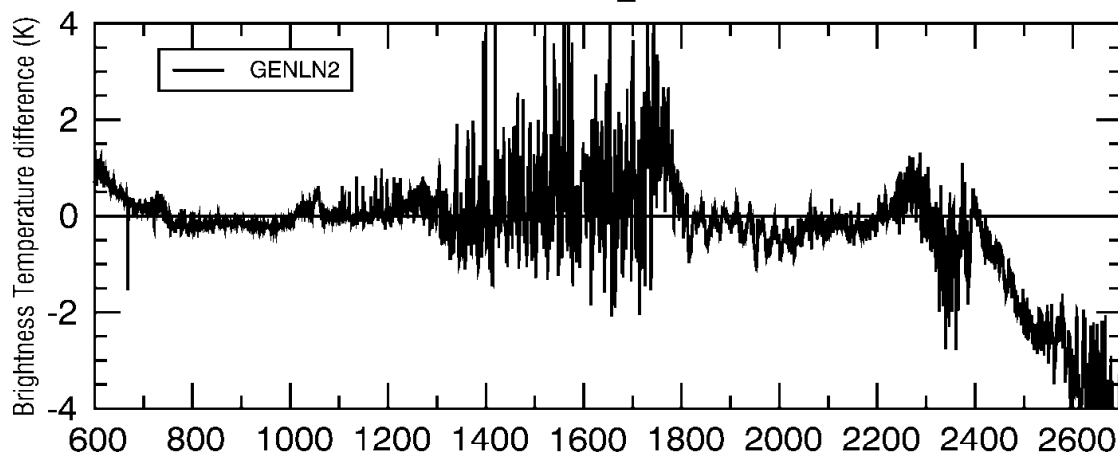


Figure 49: Radiance residuals between calculated and measured radiance for ARIES. Calculated radiances were obtained using the GEISA2003 molecular database.

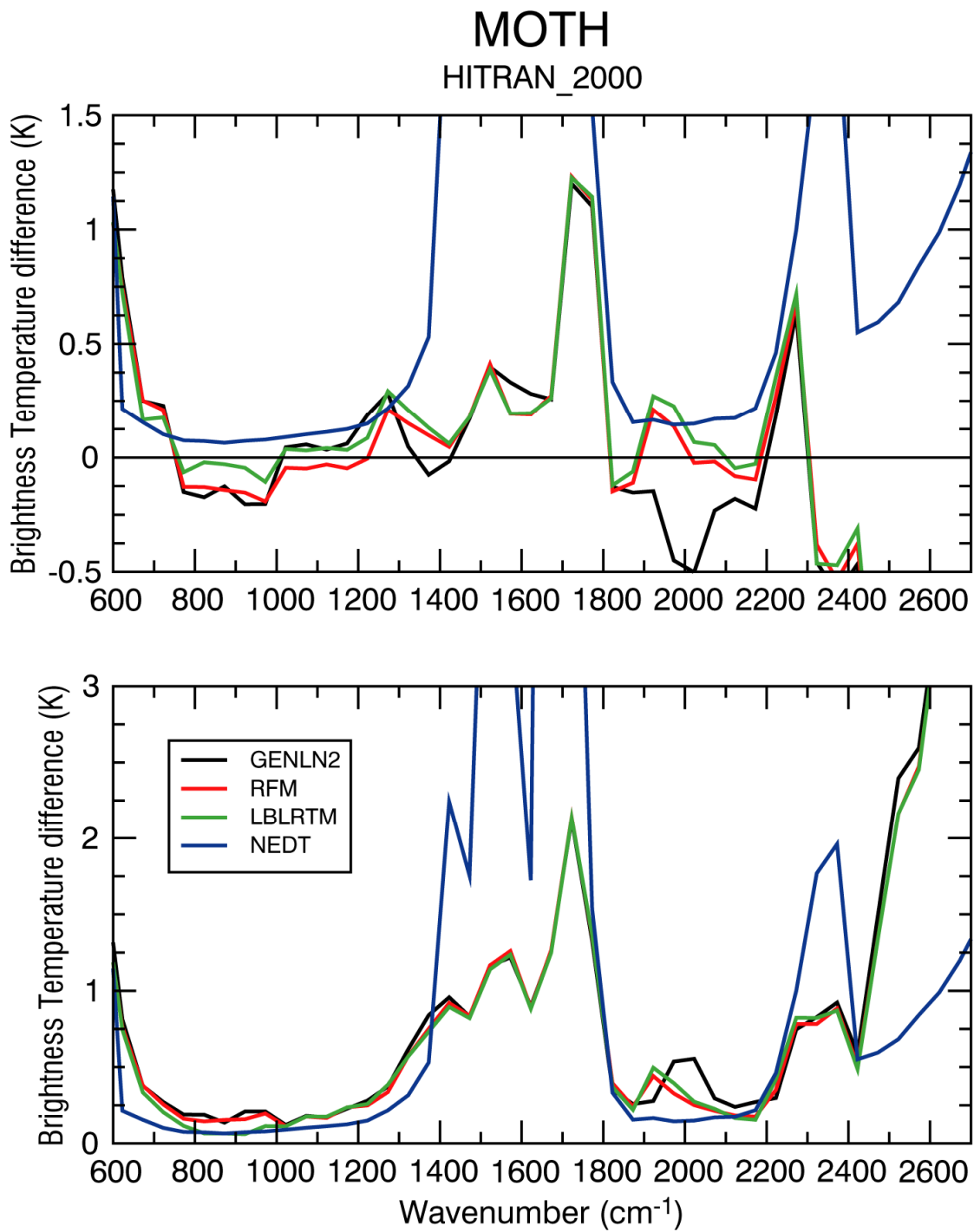


Figure 50: Bias (upper panel) and root-mean-square-error (lower panel) of the difference between simulated and measured spectra for the MOTH case. Values for ARIES band 1 and band 2 are computed over intervals of 50 cm<sup>-1</sup> using the HITRAN2000 molecular database.

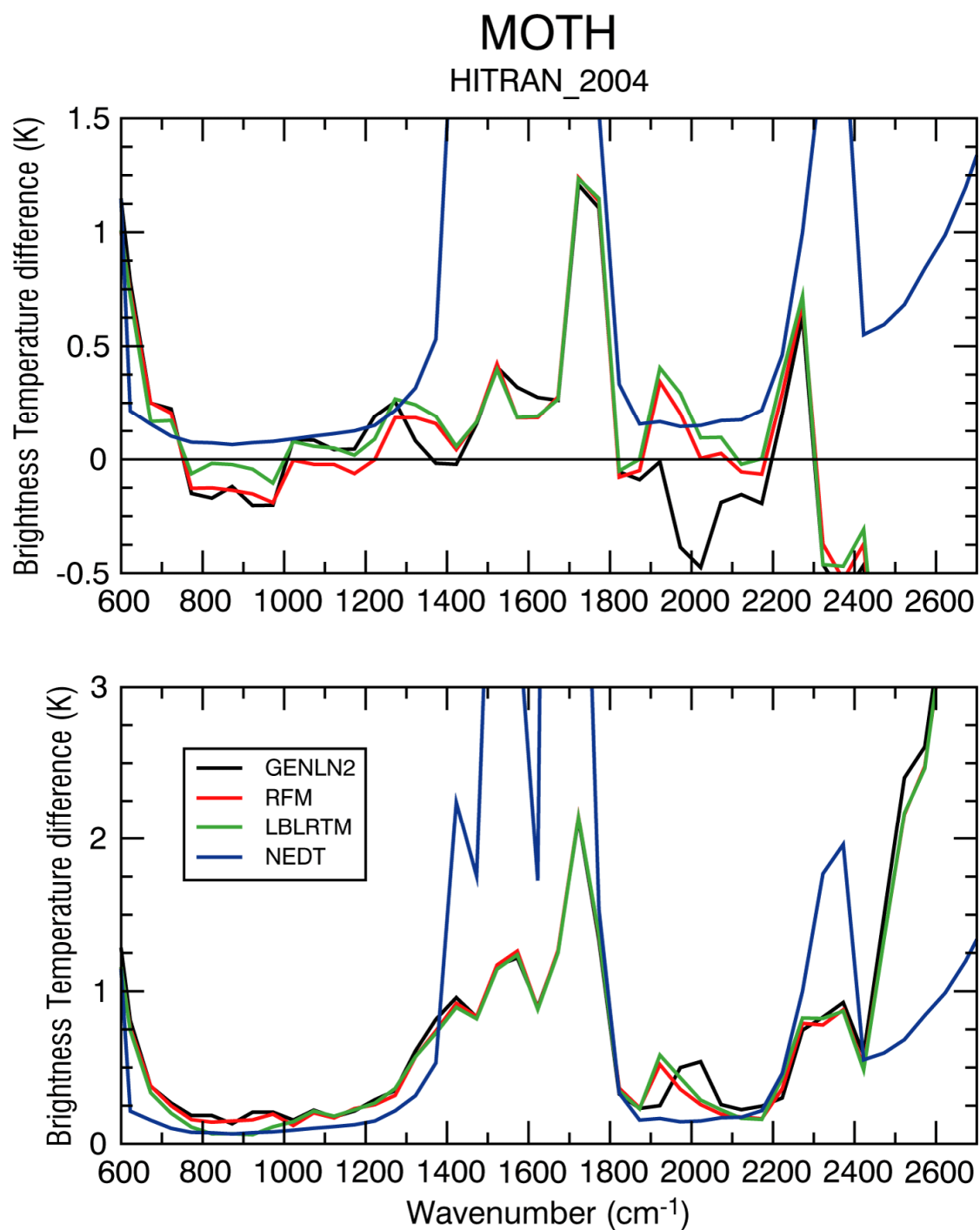


Figure 51: Bias (upper panel) and root-mean-square-error (lower panel) of the difference between simulated and measured spectra for the MOTH case. Values for ARIES band 1 and band 2 are computed over intervals of 50 cm<sup>-1</sup> using the HITRAN2004 molecular database.

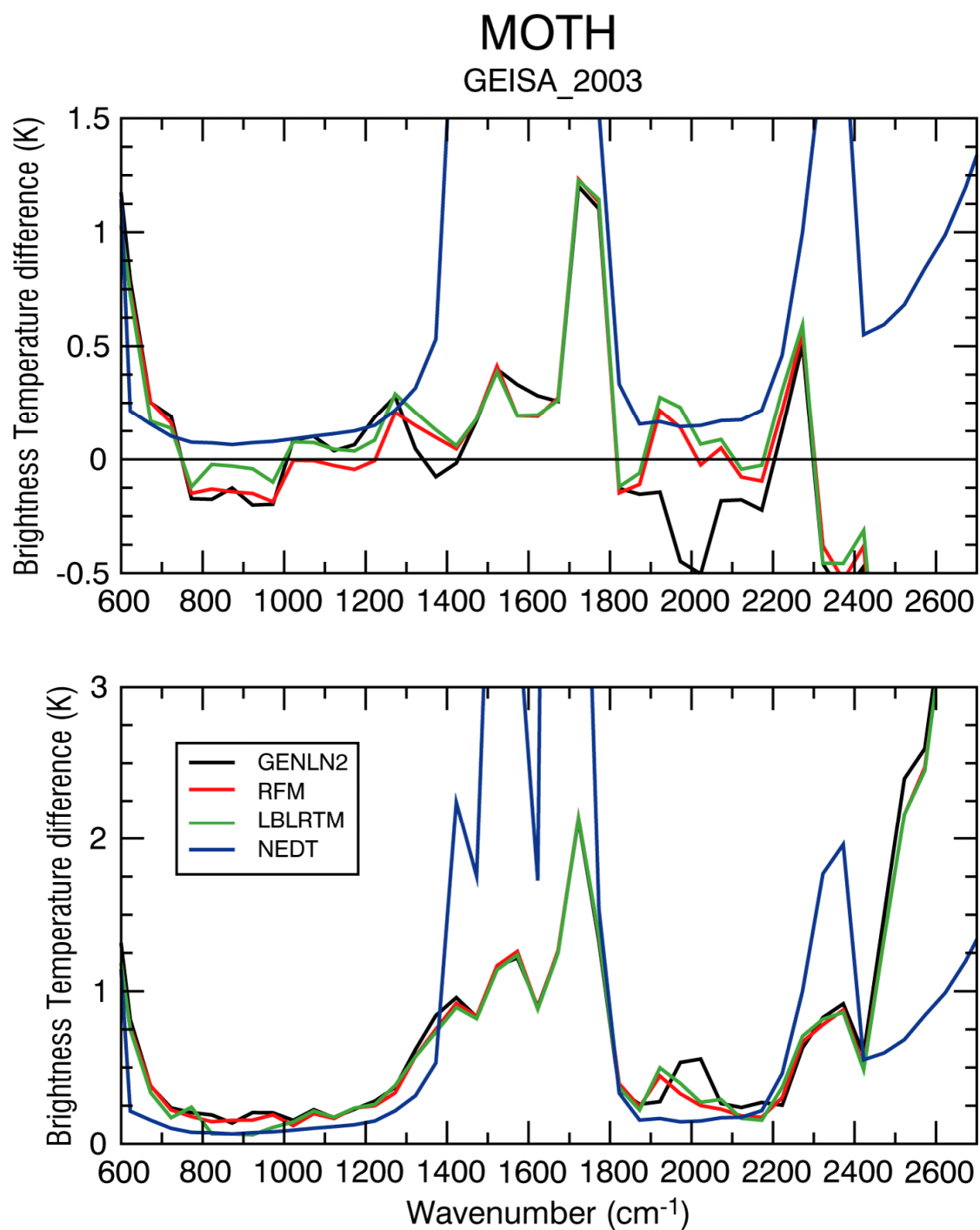


Figure 52: Bias (upper panel) and root-mean-square-error (lower panel) of the difference between simulated and measured spectra for the MOTH case. Values for ARIES band 1 and band 2 are computed over intervals of  $50 \text{ cm}^{-1}$  using the GEISA2003 molecular database.

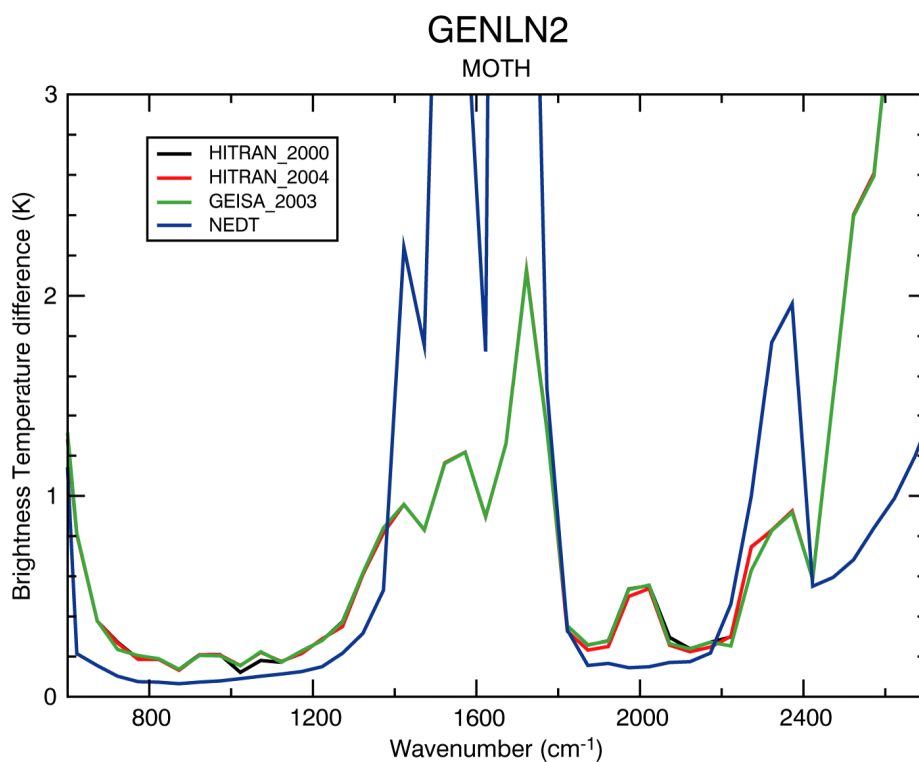


Figure 53: Root-mean-square-error of the difference between simulated and measured spectra for the MOTH case. Spectra are computed using the GENLN2 model utilizing the HITRAN2000, HITRAN2004 and GEISA2003 molecular databases.

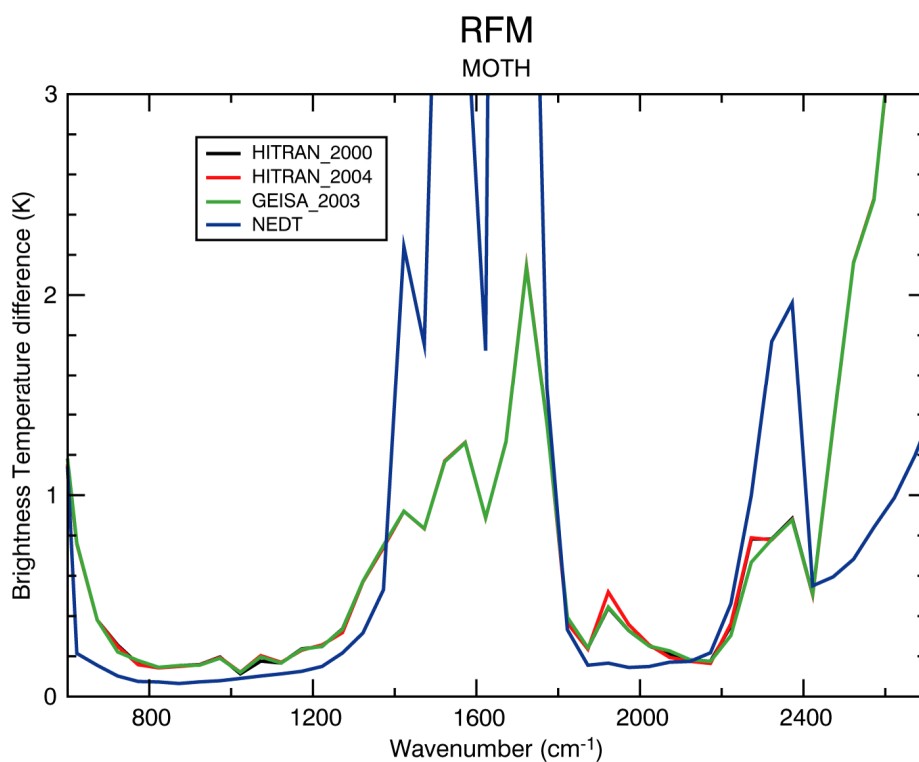


Figure 54: Root-mean-square-error of the difference between simulated and measured spectra for the MOTH case. Spectra are computed using the RFM model utilizing the HITRAN2000, HITRAN2004 and GEISA2003 molecular databases.

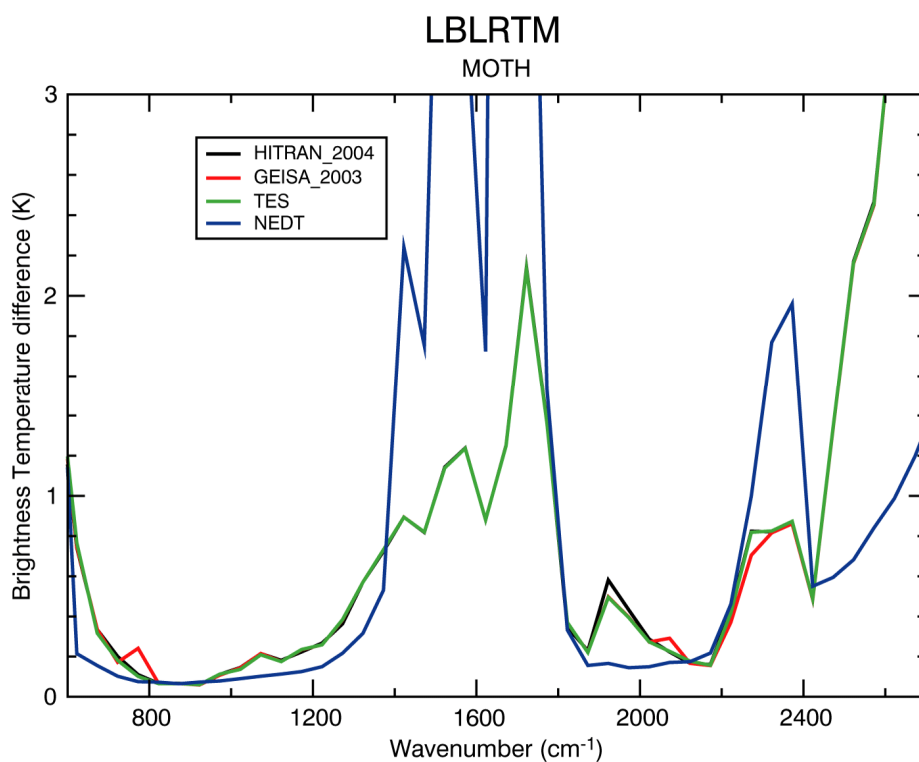


Figure 55: Root-mean-square-error of the difference between simulated and measured spectra for the MOTH case. Spectra are computed using the LBLRTM model utilizing the HITRAN2000, HITRAN2004 and GEISA2003 molecular databases.

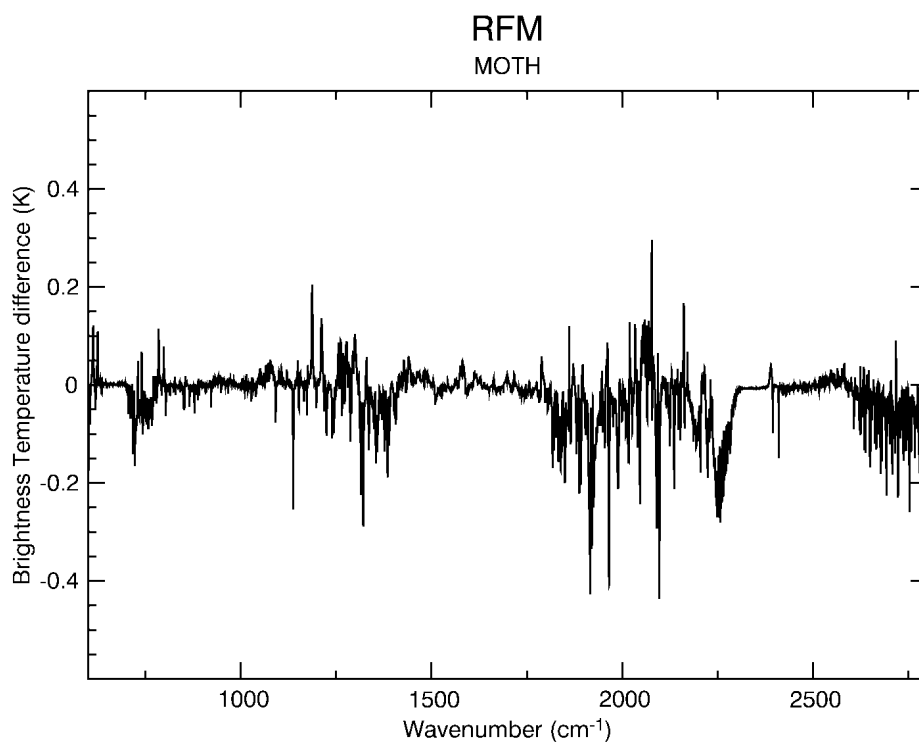


Figure 56: Radiance residuals between radiances calculated using the GEISA2003 database and radiances calculated using the HITRAN2004 database. Spectra are computed using the RFM model.

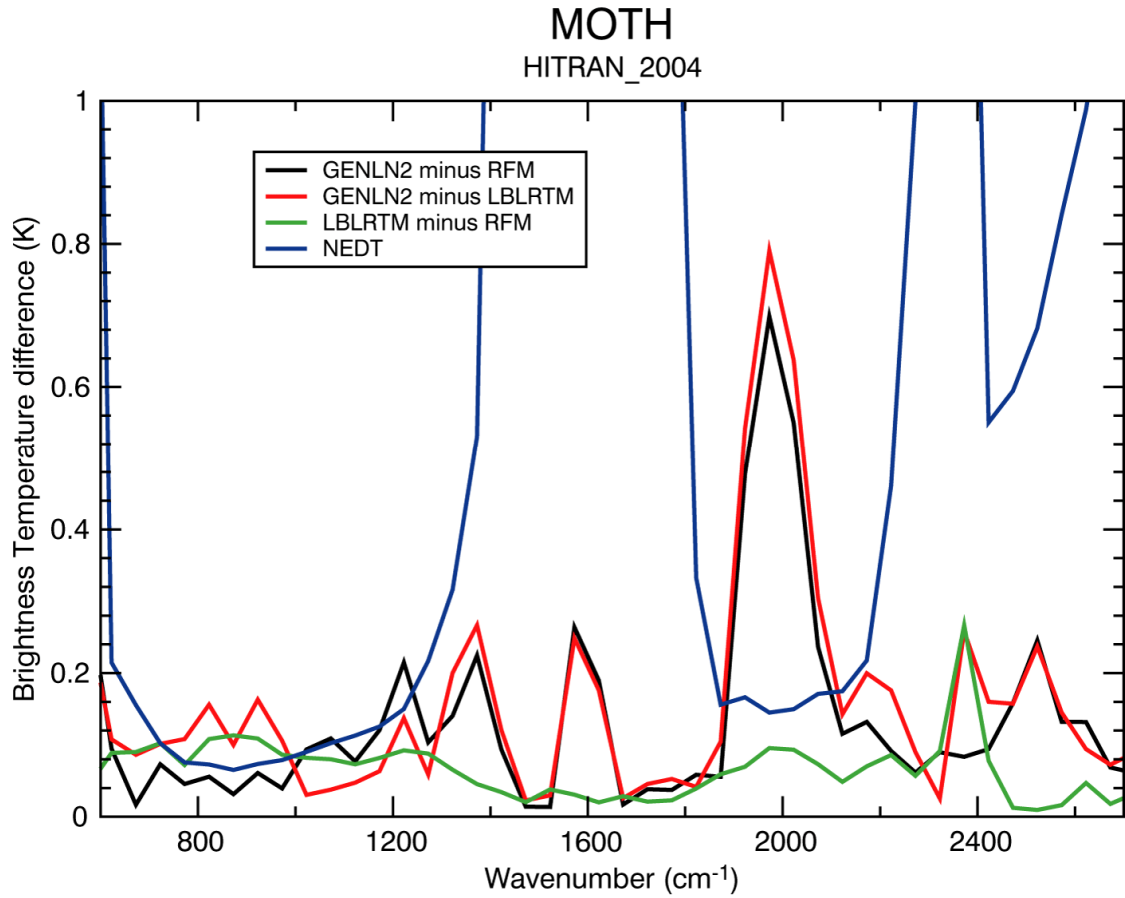


Figure 57: Root-mean-square-error of the difference between simulated spectra for the MOTH case.

## Results for ARM case

We have used for the comparison the measurement by AERI-00, since differences with AERI-01 are very small and in any case much smaller than the standard deviation during the period of integration.

Some characteristics of AERI are given in Table 8. The S/N curve (not shown) is largely variable across the spectrum, generally decreasing with increasing wave number and with relative minima across window regions since the signal measured in window regions when looking at the zenith is relatively low. Our analysis will concentrate below 2200 cm<sup>-1</sup> since the S/N values at larger wave numbers is below 100. The processing from HR spectra to the final simulated spectra is same as described in the CAMEX-I section, account taken of the different properties of AERI.

Table 8: AERI Parameters

Band	Band 1		Band 2	
Free Spectral Range (cm <sup>-1</sup> )	0.	7988.5	0.	7988.5
Optical filter Range (cm <sup>-1</sup> )	520	1800	1800	3020
Spectral Spacing (cm <sup>-1</sup> )	.4821472		.4821472	
Maximum Delay (cm)	1.037028		1.037028	
Unapodised Resolution (cm <sup>-1</sup> )	.4821472		.4821472	

Figures 58, 59 and 60 show some interesting features. Firstly, it is evident how RFM is in better agreement with observations in the transparent region of the spectrum between 800 and 1000 cm<sup>-1</sup>. Also noticeable is the worse performance of GENLN2 in the 1080 to 1230 cm<sup>-1</sup> region and the significantly larger scatter of the RFM and LBLRTM residuals in the 1900 to 2150 cm<sup>-1</sup> region.

Figures 61, 62 and 63 show the bias and rms of the difference between simulated and measured radiances, computed over intervals of width 50 cm<sup>-1</sup>. The behavior of the rms and bias curves, for all LBL codes, indicate that a large fraction of the rms values is due to systematic errors and that the AERI-00 estimated averaged noise is much smaller than the discrepancies of the simulations with the measurements. All simulations underestimate the measured radiances almost in the whole range, and although the spectral behaviour of rms differences is very similar, LBLRTM tends to have a larger negative bias. In the range from 1900 to 2150 cm<sup>-1</sup> RFM and LBLRTM have a bias that is significantly larger than the GENLN2 bias.

In the interval between 600 and 1000 cm<sup>-1</sup>, larger discrepancies with measurement are found for LBLRTM in the most transparent regions. A local minimum in rms is seen from 1250 to 1400 cm<sup>-1</sup> where important absorption by N<sub>2</sub>O and CH<sub>4</sub> occurs on top of H<sub>2</sub>O absorption. The rms curves attain another maximum in the water vapor band mostly caused again by a systematic underestimation by both codes. A minimum in both bias and rms curves is obtained around 1840 cm<sup>-1</sup>, where absorption by H<sub>2</sub>O is still quite important and then larger bias and rms differences beyond 1900 cm<sup>-1</sup> are seen in a region of weaker H<sub>2</sub>O absorption. All these results point to the great need to improve our knowledge in basic spectroscopy of the water vapor molecule and are a clear indication of the role played by the water vapor continuum absorption. The use of the CKD\_2.1 continuum utilized in GENLN2 significantly reduces the errors from 1900 to 2150 cm<sup>-1</sup> whereas in the region between 1080 and 1230 cm<sup>-1</sup>, another region where we expect the continuum to give a significant contribution to absorption, the use of the CKD\_2.1 continuum does not results in a reduction of the errors. Results in the 1900 to 2150 cm<sup>-1</sup> region are noticeable since they are in contrast to what seen for HIS, NAST-I and ARIES where the performance of GENLN2 in this region was worse than RFM and LBLRTM. It is interesting to note how RFM is performing consistently better than GENLN2 and LBLRTM across the whole spectrum.

Figure 67 shows that residuals generated by the use of different line parameters are in general well below 0.4K and are negligible in the water vapor band. For some isolated channels differences can be as large as 0.8 K. From Figure 64 it can be seen that the use of GENLN2 in conjunction with HITRAN2004 generates larger rms values. Since this feature is only observed for the GENLN2 case, it might point to a possible inconsistency between the HITRAN2004 line parameters and the CKD\_2.1 continuum. In other regions of the spectrum only slight differences can be observed. For the GENLN2 case HITRAN2004 has slightly positive impact between 1050 and 1200 cm<sup>-1</sup> whereas HITRAN2000 has a slight negative impact around 1000 cm<sup>-1</sup> and GEISA2003 has a slight positive impact around 750

$\text{cm}^{-1}$ . For the RFM case HITRAN2004 has a slight negative impact around  $2000 \text{ cm}^{-1}$  whereas GEISA2003 has a positive impact around  $750 \text{ cm}^{-1}$  and  $1080 \text{ cm}^{-1}$ . For the LBLRTM case we can notice that the TES database has a very slight positive impact around  $750 \text{ cm}^{-1}$  and a negative impact around  $800 \text{ cm}^{-1}$ .

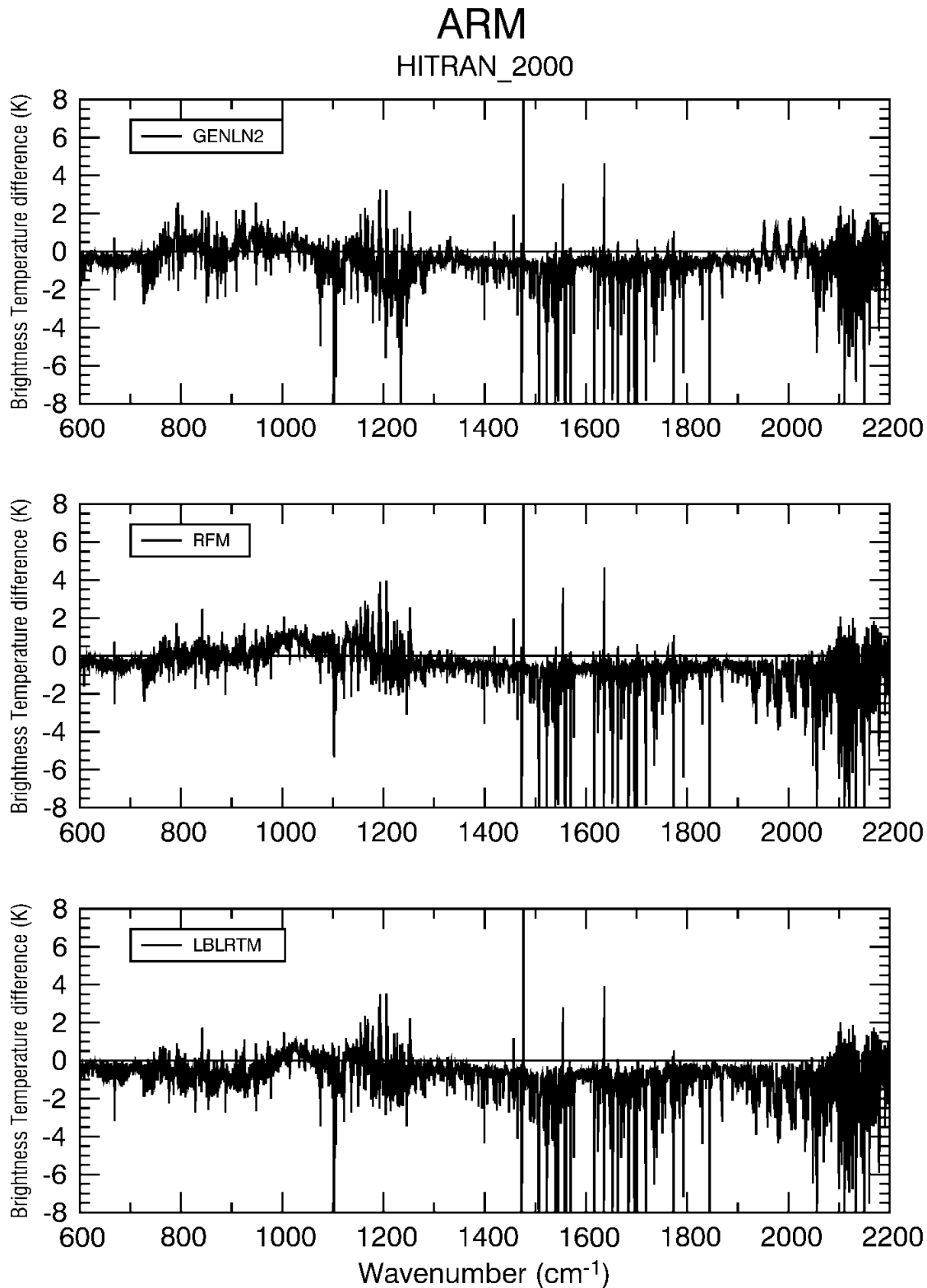


Figure 58: Radiance residuals between calculated and measured radiance for AERI. Calculated radiances were obtained using the HITRAN2000 molecular database.

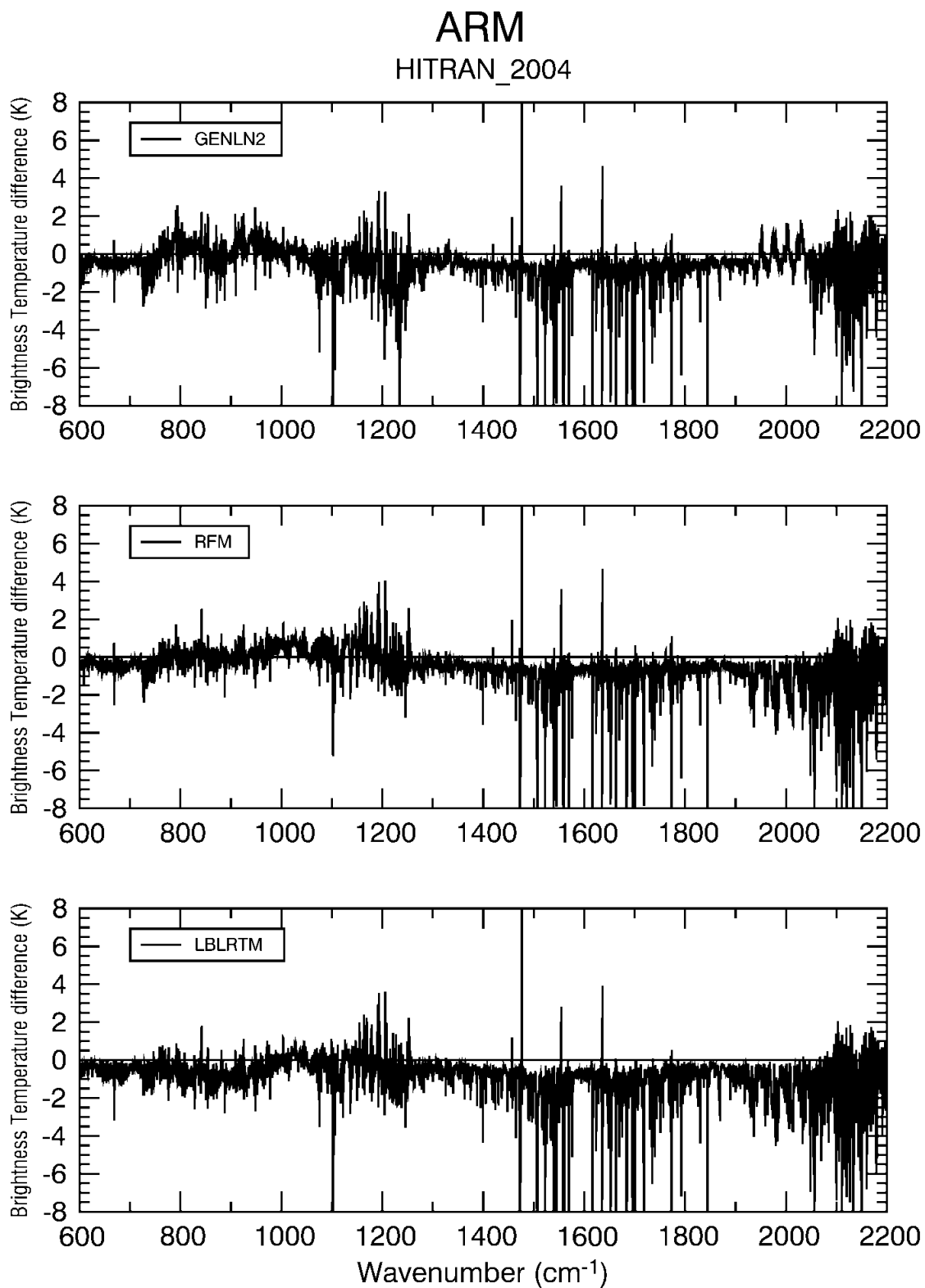


Figure 59: Radiance residuals between calculated and measured radiance for AERI. Calculated radiances were obtained using the HITRAN2004 molecular database.

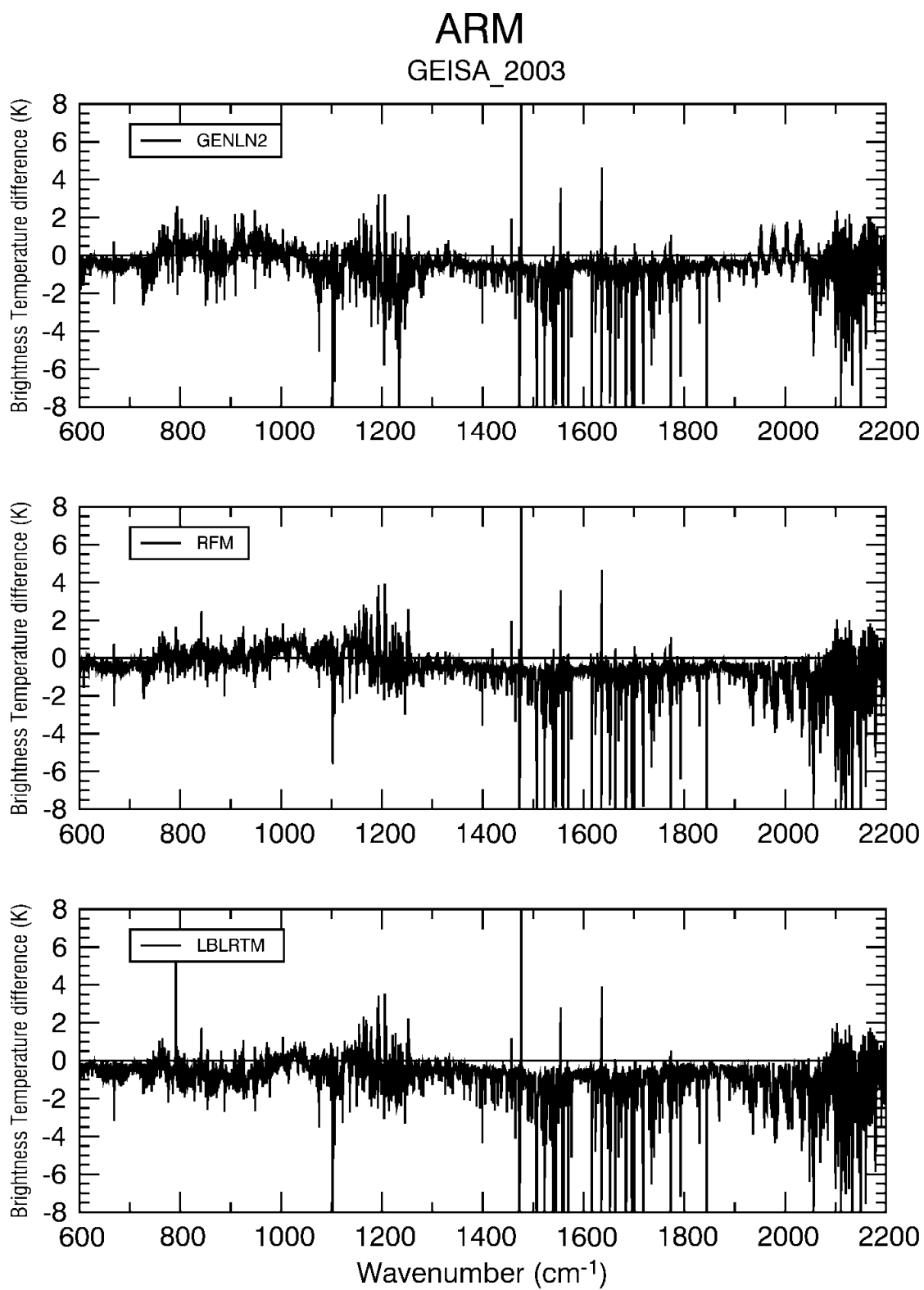


Figure 60: Radiance residuals between calculated and measured radiance for AERI. Calculated radiances were obtained using the GEISA2003 molecular database.

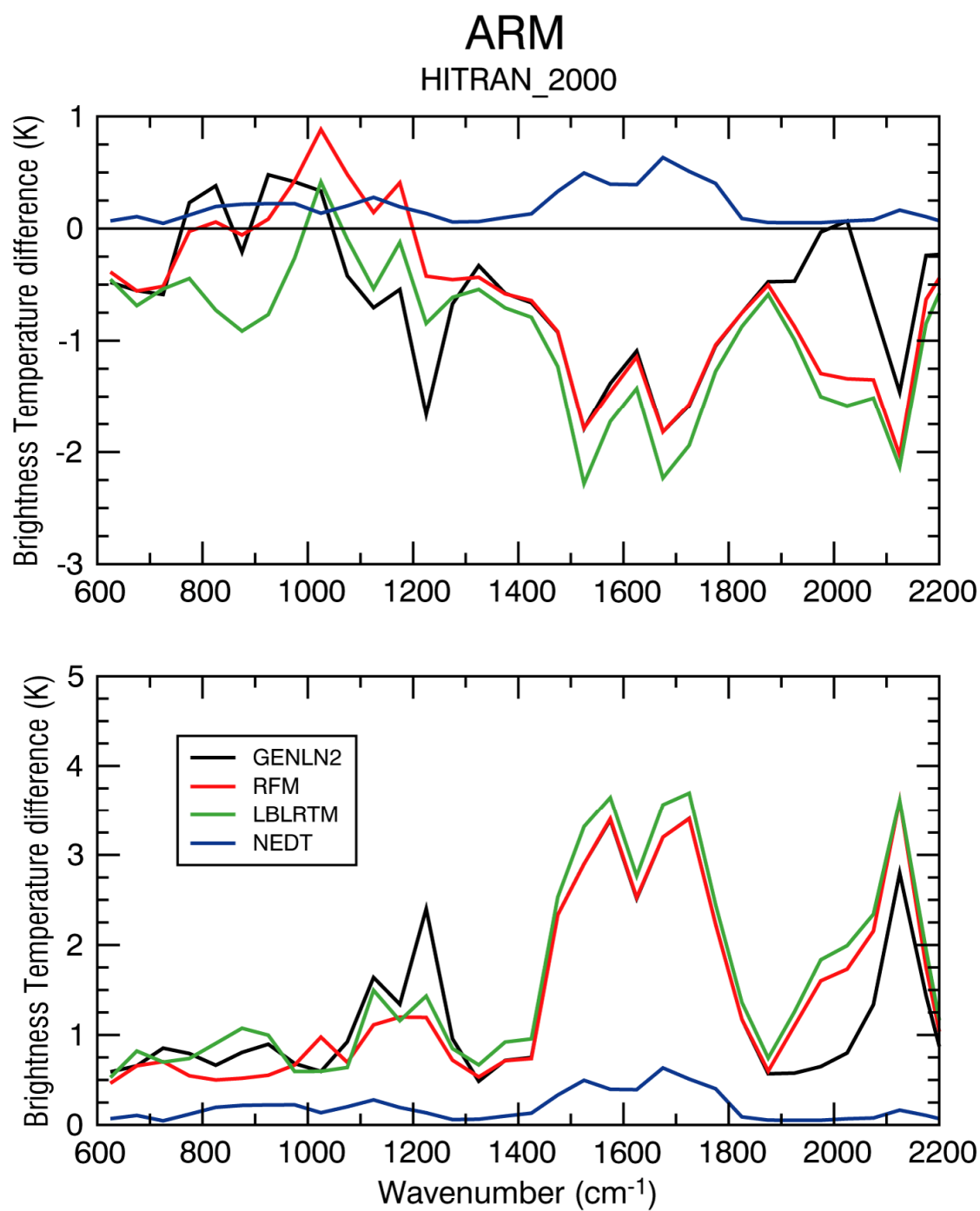


Figure 61: Bias (upper panel) and root-mean-square-error (lower panel) of the difference between simulated and measured spectra for the ARM case. Values for AERI band 1 and band 2 are computed over intervals of  $50 \text{ cm}^{-1}$  using the HITRAN2000 molecular database.

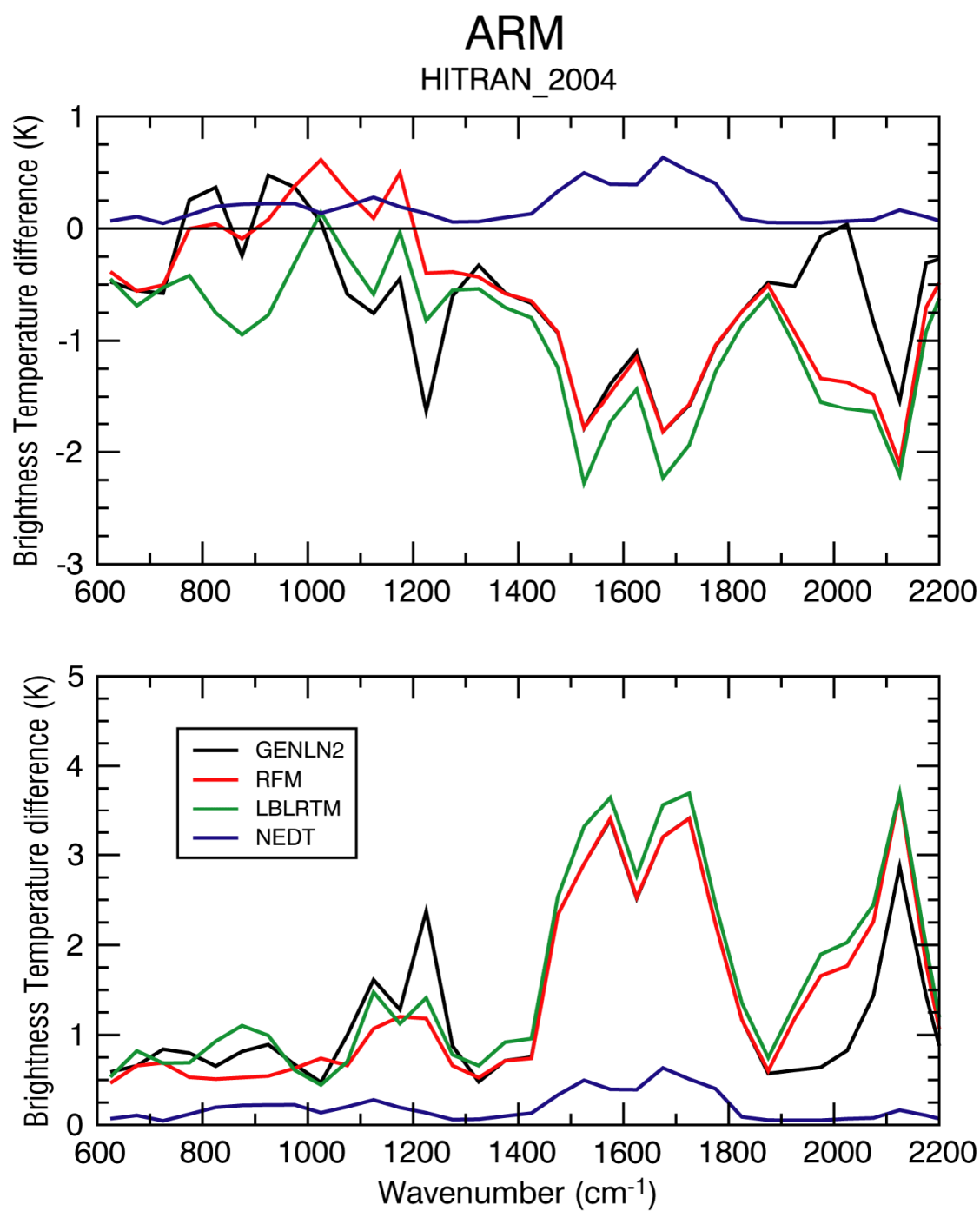


Figure 62: Bias (upper panel) and root-mean-square-error (lower panel) of the difference between simulated and measured spectra for the ARM case. Values for AERI band 1 and band 2 are computed over intervals of  $50 \text{ cm}^{-1}$  using the HITRAN2004 molecular database.

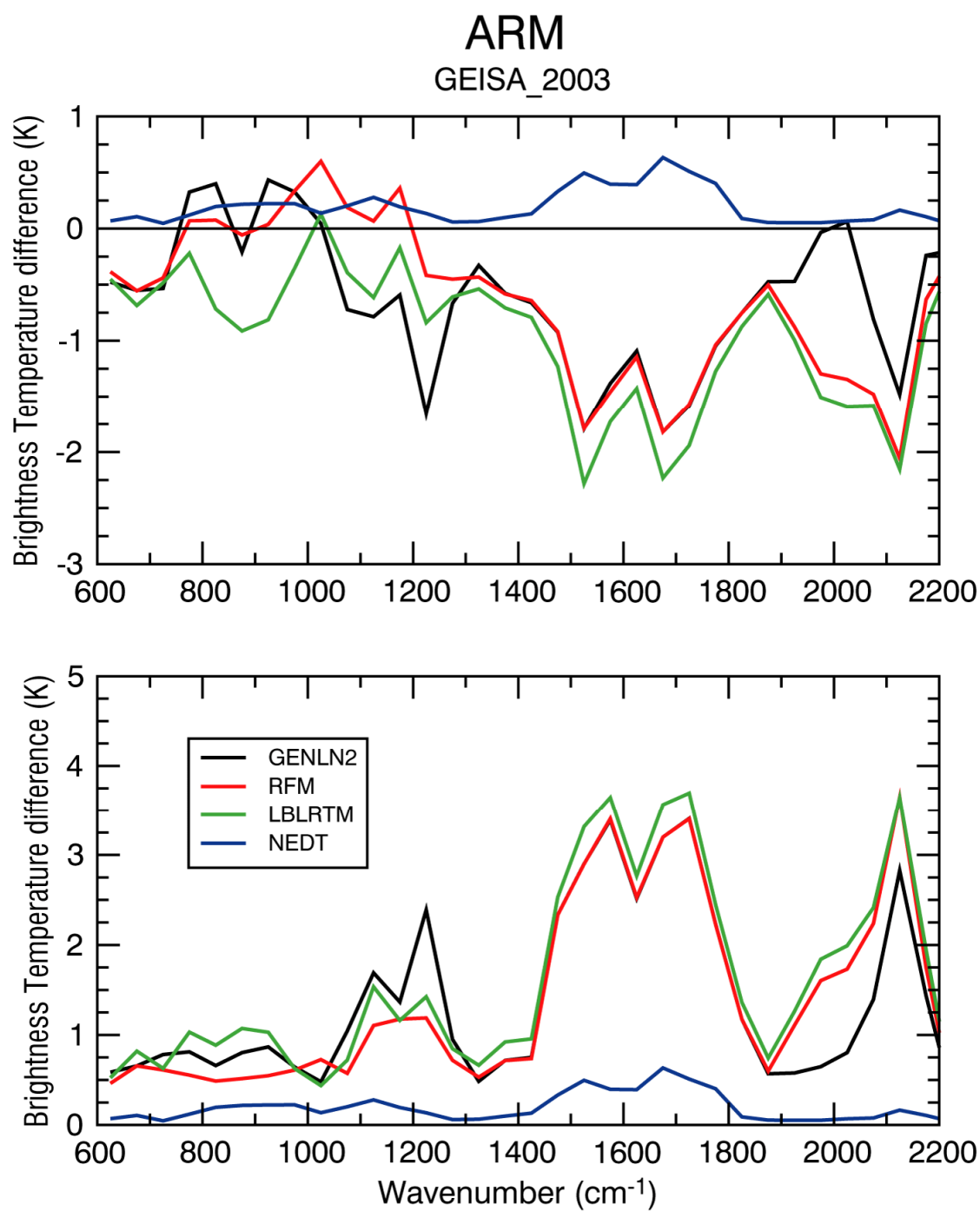


Figure 63: Bias (upper panel) and root-mean-square-error (lower panel) of the difference between simulated and measured spectra for the ARM case. Values for AERI band 1 and band 2 are computed over intervals of 50 cm<sup>-1</sup> using the GEISA2003 molecular database.

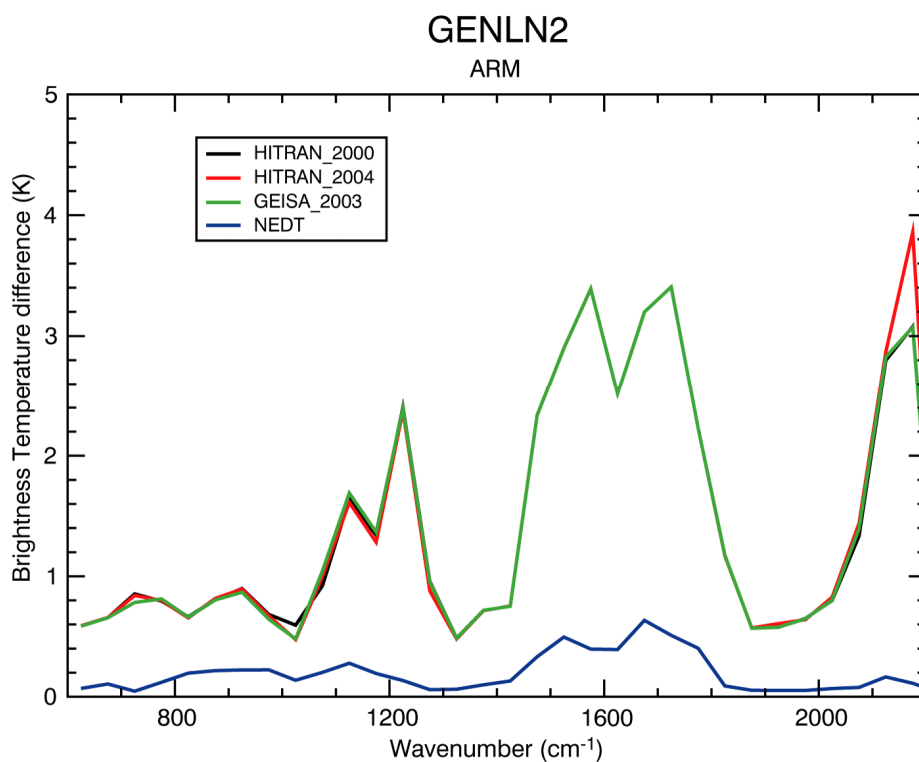


Figure 64: Root-mean-square-error of the difference between simulated and measured spectra for the ARM case. Spectra are computed using the GENLN2 model utilizing the HITRAN2000, HITRAN2004 and GEISA2003 molecular databases.

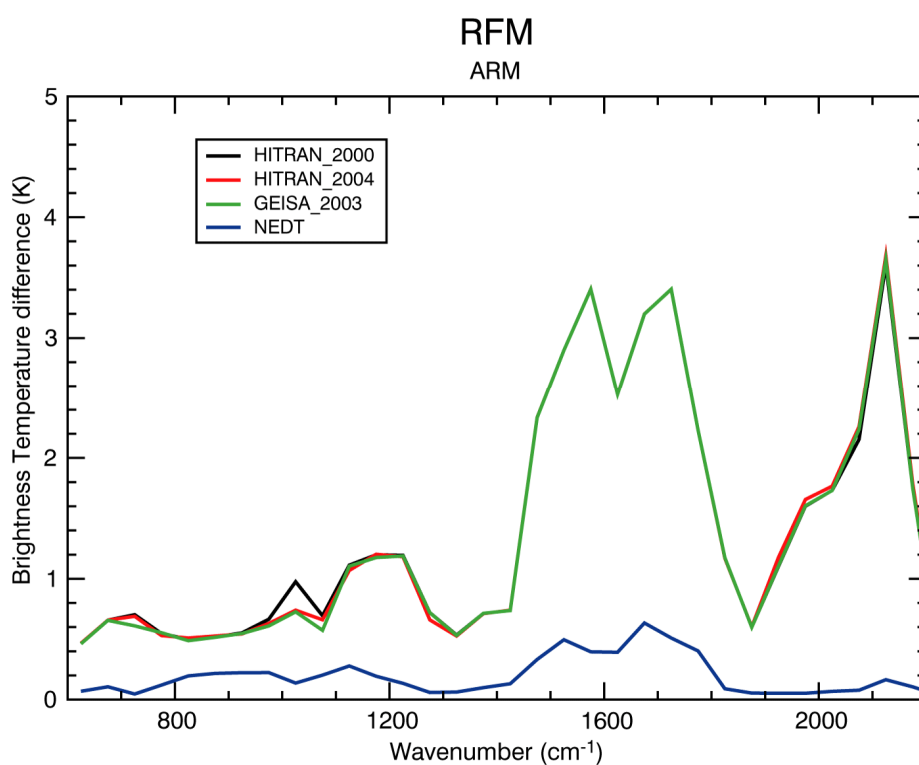


Figure 65: Root-mean-square-error of the difference between simulated and measured spectra for the ARM case. Spectra are computed using the RFM model utilizing the HITRAN2000, HITRAN2004 and GEISA2003 molecular databases.

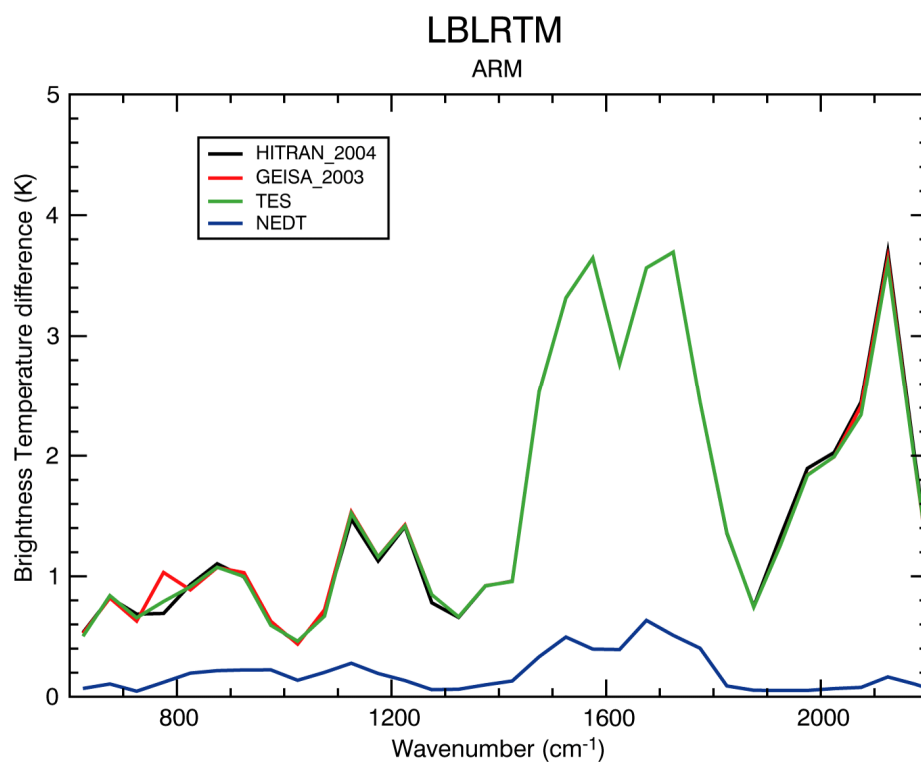


Figure 66: Root-mean-square-error of the difference between simulated and measured spectra for the MOTH case. Spectra are computed using the LBLRTM model utilizing the HITRAN2000, HITRAN2004 and GEISA2003 molecular databases.

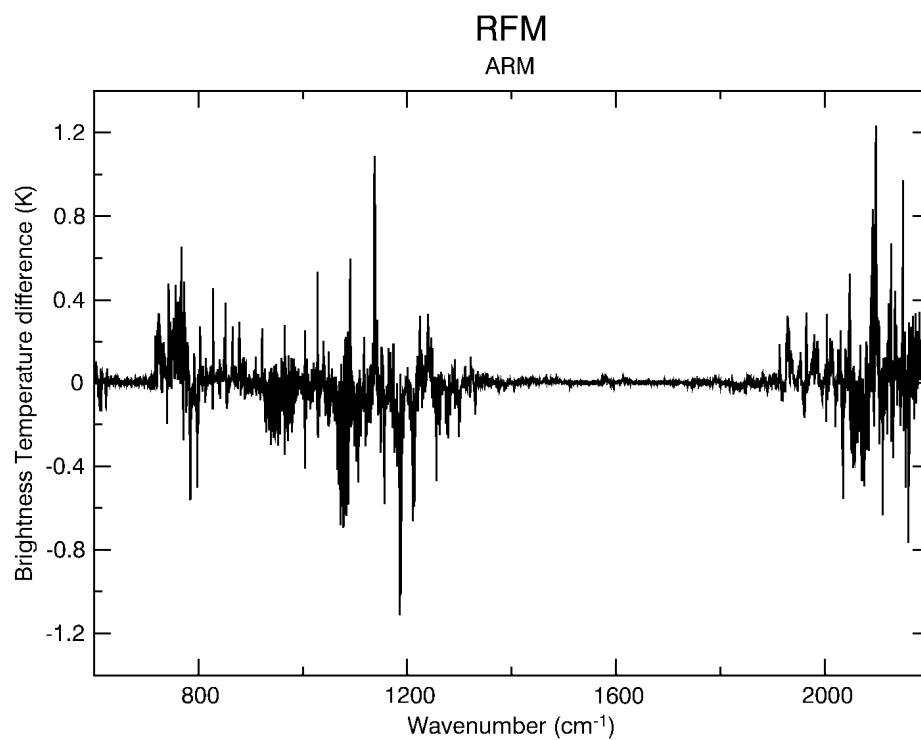


Figure 67: Radiance residuals between radiances calculated using the GEISA2003 database and radiances calculated using the HITRAN2004 model. Spectra are computed using the RFM model.

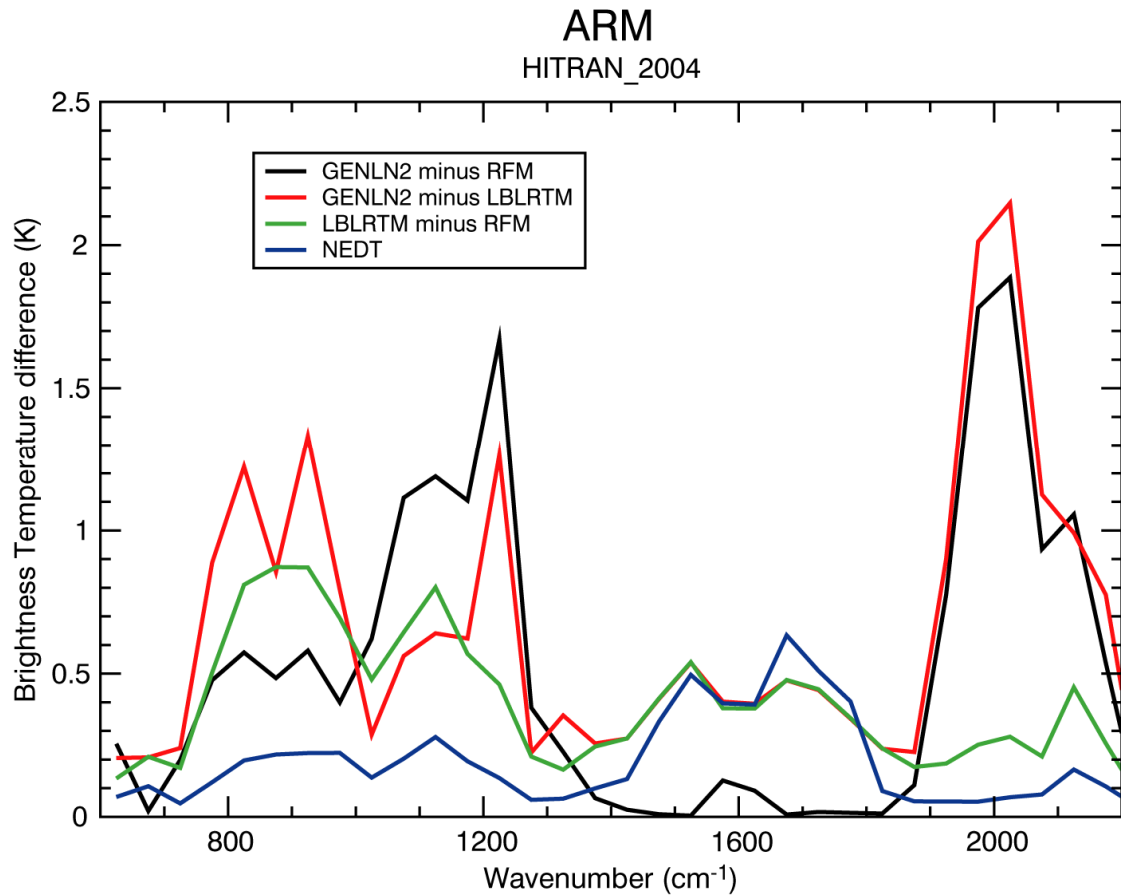


Figure 68: Root-mean-square-error of the difference between simulated spectra for the ARM case.

### Sensitivity to changes in temperature and humidity profiles

An exercise similar to that described in the CAMEX-I section was carried out for the ARM case as well. The dataset contains estimates of the water vapor and temperature uncertainties. A major difference to the CAMEX-1 case is that the uncertainty values are not an upper limit but random errors (1 standard deviation) derived from statistical variability of the various measurements during the averaging period. Radiosonde uncertainties were derived from the inter-batch variability observed in dual-sonde launches over the course of the IOP. The temperature and water vapor mixing ratio error profiles are shown in Figure 69. Errors in mixing ratio are typically between 10 and 20% in the 980 to 300 hPa range, while the error can be as great as 30% at lower pressures. For temperature, errors are less than 0.2%. As for the CAMEX-1 case, we computed GENLN2 spectra by increasing and decreasing the average temperature and water vapor profiles by the error profile. Results are shown in Fig. 70(a) for temperature and 70(b) for water vapor, where the relative bias for the perturbed case is plotted with the relative bias and the relative rms for the reference case. These results suggest that uncertainties in the characterization of the temperature profiles are likely not to have resulted in any significant impact on the accuracy of the calculations. As for the humidity profile, part of the bias in the 700 to 1400 cm<sup>-1</sup> range could be explained in terms of uncertainties in the water vapor profile, but the large differences seen across the water vapor vibro-rotational band cannot be attributed to profiling uncertainties. Again, the close match between bias and rms (not shown) suggests that one of the effects of having perturbed the atmospheric profiles is to impart an offset to the radiances.

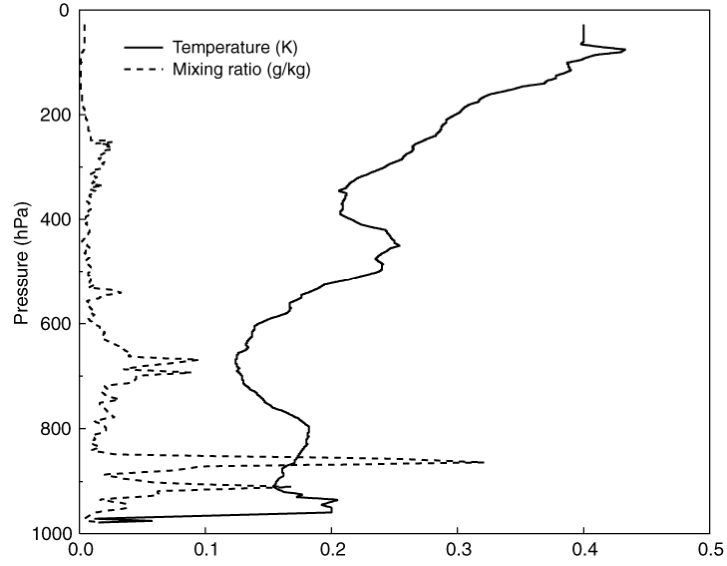


Figure 69. The ARM-WVIOP case error profile for temperature and water vapour mixing ratio.

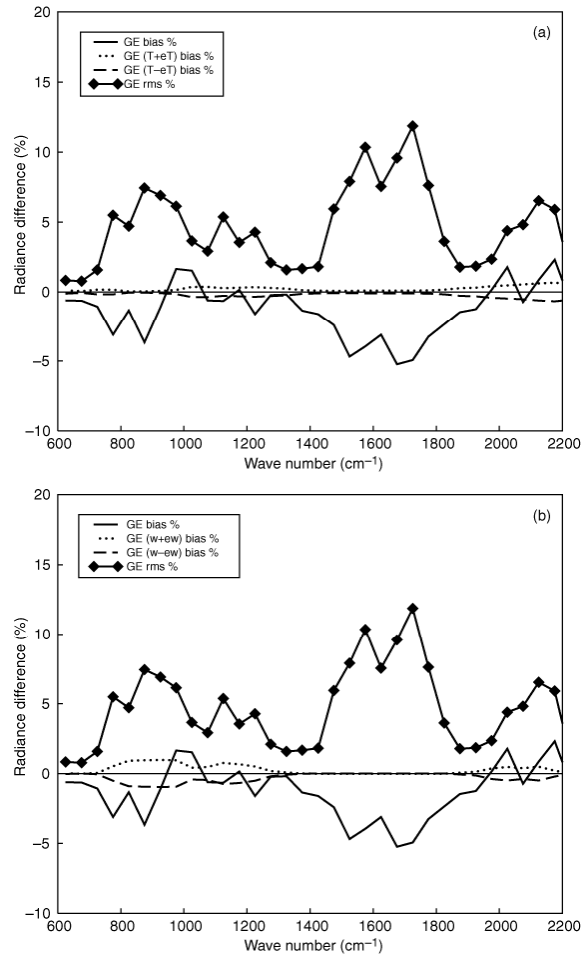


Figure 70: The relative bias of the difference between the reference GENLN2 spectra and those computed by: (a) increasing (GE (T+eT)) and decreasing (GE (T-eT)) the temperature profile by the error profile; (b) increasing (GE (w+ew)) and decreasing (GE (w-ew)) the water vapor profile by the error profile, are shown for the ARM-WVIOP case. The relative bias and root-mean-square-error of the difference between the reference GENLN2 spectra and the measured spectra is also shown as solid and solid-diamond line (GE). Values are computed over intervals of  $50 \text{ cm}^{-1}$  width.

## General discussion and conclusions

Five test cases are examined where simulated spectra are compared to spectra measured during the first Convection and Moisture Experiment (CAMEX-1) campaign, the third Convection and Moisture Experiment (CAMEX-3), the EAQUATE campaign, the MOTH-Tropic campaign and the Water Vapor Intensive Observing Period (WVIOP) at the Atmospheric Radiation Measurement (ARM) site. A special emphasis is given to the up-welling radiance spectra because of the similarity in viewing geometry with the atmospheric sounders AIRS and IASI. The primary objective of the paper is to quantify differences due to different forward model mechanics and to the quality of the spectroscopic databases used in the forward model computations and identify spectral regions where forward model errors are smallest.

The simulations are performed using three different LBL codes, HARTCODE, GENLN2 and RFM in very controlled conditions, with a pre-defined atmospheric layering and surface conditions.

The data measured during the CAMEX-1 and ARM cases is the result of averaging of individual spectra: during the CAMEX-1 case the signal is averaged over an atmospheric path of about 50 km, while in the ARM case 15 individual spectra are averaged, covering a period of about two hours. In both cases therefore the estimated measurement standard deviation incorporates the spectral variations induced by true atmospheric variability during the measuring period. The data measured during the MOTH campaign is the result of averaging 10 individual spectra. Since the averaging was performed during a very limited period of time, spectral variations induced by the atmospheric variability during the measuring period are negligible. Consequently the measurement noise is almost entirely made of the radiometric noise. In the case of the CAMEX-III and EAQUATE campaigns we have used single NAST-I spectra and the measurement noise coincides with the instrument noise.

In most spectral regions the difference between simulations and measurement is much larger than the difference between the three codes, which are highly correlated. This result suggests that most of the discrepancies with measurements are not due to the particular computational procedures adopted by the three codes but rather to insufficient knowledge in basic spectroscopy. Results show that in the important temperature sounding region  $730\text{--}770\text{ cm}^{-1}$  the  $\text{CO}_2$  line has a fairly regular spacing and the largest (negative) deviations are very close, but not coincident, with line centers; between the main lines however systematically positive deviations are observed with a magnitude about half the maximum (negative) local “errors”. In presence of isolated water vapor lines these positive deviations are of larger magnitude. In the window region the deviations are largest in presence of single or a small group of water vapor lines. The largest differences are in general seen in correspondence with groups of tightly spaced lines, a far from uncommon situation since one cannot speak of wings between lines in most part of the range under consideration. These results indicate however that it is possible to identify spectral regions, that have been pointed out and discussed in the previous sections, where the simulations are closer to the measurements.

In the CAMEX-I case LBLRTM is closer to measurements in the longwave window region and in the water vapour band whereas RFM is closer to measurements in the  $\text{CO}_2$   $\nu_2$  band and in the ozone band. The GENLN2 fails to capture the water continuum absorption in the  $1600\text{ cm}^{-1}$  region and the  $2050\text{ cm}^{-1}$  region. The rms of the difference between the models computed over intervals of  $50\text{ cm}^{-1}$  oscillates between 0.1K and 0.4K in the  $\text{CO}_2$   $\nu_2$  band and is less than 0.1 K in the longwave window region and in the ozone band. In the water vapour band it can reach a maximum of 0.4K at  $1600\text{ cm}^{-1}$ . In the shortwave region differences are typically below 0.4K in the  $2000\text{ cm}^{-1}$  region. We can not comment beyond  $2200\text{ cm}^{-1}$  since the measurement noise is too high. If we look at the differences between simulation and observations then the rms oscillates between 0.7K and 0.1K in the  $\text{CO}_2$   $\nu_2$

band and is less than 0.3 K in the longwave window region. In the ozone band the rms can reach 1.4K and in the water vapour band it increases steadily from 0.8 to 2K.

The CAMEX-III case is characterized by larger departures than the CAMEX-I case. If we look at the differences between simulation and observations then the rms oscillates between 1.2K and 0.25K in the CO<sub>2</sub> u2 band and is less than 0.3 K in the longwave window region. In the ozone band the rms is less than 0.5K and in the water vapour band it increases steadily from 0.5 to 4.5K. The rms of the difference between the models is greatest at a number of local maxima in the water vapour band around 1350, 1600 and 2000 cm<sup>-1</sup>. A maximum value of 0.7K is attained at 2000 cm<sup>-1</sup>. In the CO<sub>2</sub> u2 band the largest differences are observed between LBLRTM and RFM and the rms can be as large as 0.5K. In the CO<sub>2</sub> u2 band and in the longwave window region LBLRTM is closer to observations than GENLN2 and RFM. RFM is still performing better than LBLRTM and GENLN2 in the ozone band. The behaviour in the water vapour band is different from that observed in the CAMEX-I case above all in the 2000 cm<sup>-1</sup> region. In fact in this region GENLN2 is now performing significantly better than RFM and LBLRTM most likely as a result of the different continuum model. LBLRTM perform better from 1600 to 1700 cm<sup>-1</sup> whereas in the region between 1200 and 1400 cm<sup>-1</sup> different models perform better in different regions.

For the EAQUATE case differences are smaller than those observed in the CAMEX-III case. In particular inter-model differences in the water vapour band at 2000 cm<sup>-1</sup>. A local rms maximum of 0.5K is observed at 1600 cm<sup>-1</sup>. Differences in the window region are below 0.05K whereas in the CO<sub>2</sub> u2 band a maximum value of 0.36K is attained for the LBLRTM versus RFM case. The rms of the difference between models and observations ranges from a maximum of 2K in the CO<sub>2</sub> u2 band, a minimum of 0.2K in the window region, and increases steadily from 0.5K to 3.5K in the water vapor band. In the CO<sub>2</sub> u2 band LBLRTM is still closer to observations than RFM and GENLN2 and in the ozone band RFM is still performing better than GENLN2 and RFM. In the water vapour band results for RFM and LBLRTM are very close whereas GENLN2 exhibits a worse performance around 1600 cm<sup>-1</sup>.

For the MOTH case inter-model results show that LBLRTM and RFM are very close across the whole spectrum. Differences in rms are typically below 0.1 K. The largest differences are obtained for the GENLN2 versus LBLRTM and GENLN2 versus RFM cases at 2000 cm<sup>-1</sup> where the rms reaches 0.8K. In terms of model versus observation we note that LBLRTM is closer to observations in the 600 to 1000 cm<sup>-1</sup> region and in the 1300 to 1600 cm<sup>-1</sup> region where the rms reaches a maximum of 1K. In the region between 1800 and 2200 cm<sup>-1</sup> GENLN2 is performing better than RFM and LBLRTM around 1930 cm<sup>-1</sup> whereas it is performing significantly worse at 2000 cm<sup>-1</sup>. In these regions rms values are smaller than 0.5K

For the ARM case, the rms of the difference between models is typically below 2K. This maximum value is once again attained at 2000 cm<sup>-1</sup>. All the models are in close agreement between 1300 and 1800 cm<sup>-1</sup>. LBLRTM and RFM exhibit in general the closest results with the exception of the CO<sub>2</sub> u2 band and the window region where RFM and GENLN2 are the closest models. The rms of the difference between models and observations is maximum at 1600 and 2100 cm<sup>-1</sup> where a maximum of 4K is attained. In the remaining regions of the spectrum values are typically below 1K. It is interesting to note how RFM is performing consistently better than GENLN2 and LBLRTM across the whole spectrum with the exception of the region around 2000 cm<sup>-1</sup> where GENLN2 is significantly closer to observations than RFM and LBLRTM.

During the course of this study we have used line parameters from various databases to test the impact of different spectroscopic data on the accuracy of the line-by-line calculations. Results for the CAMEX-I

case show that the use of the HITRAN2004 database results in a closer fit to observations in the 1250 to 1600  $\text{cm}^{-1}$  region whereas the use of the HITRAN database results in a closer fit to observations in the ozone band. For LBLRTM the use of the TES database in conjunction with the  $\text{CO}_2$  u2 P-R branch line mixing results in closer fit to observations in the 640 to 670  $\text{cm}^{-1}$ . Another observed feature is that when using the GEISA2003 database with LBLRTM we see an increase of the rms values in the 700 to 800  $\text{cm}^{-1}$  region probably because of a mismatch between line parameters and Q branch line mixing coefficients. In the CAMEX-III case the HITRAN2004 database appears to give a better agreement with observations in the 1300  $\text{cm}^{-1}$  and 1550  $\text{cm}^{-1}$  region whereas GEISA2003 is closer to observations in the 1800 to 2000  $\text{cm}^{-1}$  region. We still note that the use of HITRAN2000 results in a better fit to observations in the ozone band. For the EAQUATE case we can draw similar conclusions. In addition we can note that the use of GEISA2003 results in a better fit to observations in the  $\text{CO}_2$  u2 band. Results for the MOTH case are mixed. It appears that when used with RFM and LBLRTM, GEISA2003 results in a better fit to observations in the 1800 to 2300  $\text{cm}^{-1}$  region. However, if we look at the GENLN2 results we see that in the 1800 to 2000  $\text{cm}^{-1}$  region HITRAN2004 is closer to observations than GEISA2003.

Although a detailed assessment of the errors resulting from uncertainties in the temperature and humidity profiles is outside the scope of the present paper, the “extreme” relative humidity values contained in the CAMEX-1 dataset, and the standard deviation estimates in the ARM dataset, were used to investigate the sensitivity to changes in humidity. For the CAMEX-1 case, the difference between the simulations in HIS band 2 is well above the differences with measurements, at least in the spectral regions whose weighting functions peak in the mid to upper troposphere. In the ARM case part of the bias in the 700 to 1400  $\text{cm}^{-1}$  range can be explained in terms of uncertainties in the water vapor profile, but no sensitivity is seen across the vibro-rotational band of water vapor. In the ARM case an estimate of temperature error is also provided. The results suggest that uncertainties in the characterization the temperature profiles are likely not to have resulted in any sensible impact on the accuracy of the calculations. The close match between bias and rms suggests than one of the effects of having perturbed the atmospheric profiles is to impart an offset to the radiances.

## Acknowledgements

We want to thank R. Knuteson, P. Van Delst and D. Tobin, CIMSS, that provided the data sets and the information required to adequately process the simulated HIS and AERI data and S. Newman, Met Office, that provided the ARIES data sets and the information required to process the simulated and measured radiances. The work of Marco Matricardi was supported by EUMETSAT (EUMETSAT Contract EUM/CO/06/1504/PS).

## References

- B.H. Armstrong: 1967: Spectrum line profiles: the Voigt function. *J. Quant. Spectrosc. Radiat. Transfer*, **7**, 66-88.
- A., Carissimo, I. De Feis, and C., Serio, 2005: The physical retrieval methodology for IASI: the  $\delta$ -IASI code. *Environmental Modelling & Software*, **20-9**, pp. 1111-1126.
- F., Cayla, 1993: IASI infrared interferometer for operations and research. In “*High Spectral Resolution Infrared Remote Sensing for Earth’s Weather and Climate Studies*”, NATO ASI Series 1, Ed. A. Chedin, M. Chaine and N. Scott.

- S.A. Clough, F.X. Kneizys, L.S., Rothman and W.O. Gallery, 1981: Atmospheric transmittance and radiance: FASCOD1B. *Proc. Soc. Photo Opt. Instrum. Eng.*, **277**, pp. 152-166.
- S.A. Clough, F.X. Kneizys and R.W. Davis, 1989: Line shape and the water vapour continuum. *Atmospheric Research*, **23**, 229-241.
- S.A., Clough, M.J., Iacono and J.-L., Moncet, 1992: Line by line calculation of atmospheric fluxes and cooling rates: application to water vapor. *J. Geophys. Res.*, **98**, pp. 15761-15785.
- Cousin, C., R. le Doucen, C. Boulet and H. Henry, 1985: Temperature dependence of the absorption in the region beyond the 4.3  $\mu\text{m}$  band head of  $\text{CO}_2$ . Part 2:  $\text{N}_2$  and  $\text{O}_2$  broadening, *Applied Optics* **24**, 3899-3907.
- D., Cousin and M.J., Gazarick, 1999: NAST Interferometer Design and Characterization. *Final Report, MIT Lincoln Laboratory, Project Report NOAA-26, July 13*.
- V., Cuomo, A., Amodeo, P., Antonelli, A., Boselli, A., Bozzo, C., Cornacchia, G., D'Amico, M., Di Bisceglie, F., Esposito, P., Di Girolamo, G., Grieco, A., Larar, L., Leone, F., Madonna, T., Maestri, R., Marchese, G., Masiello, G., Meoli, L., Mona, M., Pandolfi, G., Pappalardo, G., Pavese, G., Pisani, R., Restieri, R., Rizzi, F., Romano, E., Rossi, F., Rossi, D., Sabatino, C., Serio, W., Smith, N., Spinelli, D., Summa, G., Todini, D., Villacci, X., Wang, D., Zhou, 2005: The Italian phase of the EAQUATE measurement campaign. *Proc. SPIE volume 59791E Nov. 2005*, 14 pg. (SPIE Conference "Remote Sensing of Clouds and Atmosphere X, Brugge, Belgium, 22 August 2005), doi: 10.1117/12.628279
- D.P. Edwards, 1992: GENLN2. A general Line-by-Line Atmospheric Transmittance and Radiance Model, NCAR Technical note NCAR/TN-367+STR, National Center for Atmospheric Research, Boulder, Co.
- J.R. Eyre, G.A. Kelly, A.P. McNally, E. Anderson and A. Persson, 1993: Assimilation of TOVS radiance information through one-dimensional variational analysis. *Q.J.Roy. Meteor. Soc.*, **119**, 1427-1463.
- FASCOD 3, 1989: Spectral simulation. Proceedings of the International Radiation Symposium. IRS'88 Eds. J. Lenoble and J.F. Geleyn. Deepak Publishing Co.
- D. Friedman, 1969: Infrared characteristics of ocean water (1.5-15  $\mu\text{m}$ ). *Appl. Opt.*, **8**, 2073-2078.
- V.L. Griffin, A.R. Guillory, M. Susko and J.E. Arnold, 1994: Operations Summary for the Convection and Moisture Experiment (CAMEX-1), NASA Technical memorandum, NASA TM-108445.
- G.M. Hale and M.R. Querry, 1973: Optical constants of water in the 200- $\text{nm}$  to 200- $\mu\text{m}$  wavelength region. *Appl. Opt.* **12**, 555-563.
- M.L., Hoke, S.A. Clough, W.J. Lafferty, and B.W. Olson, 1989: Line coupling in oxygen and carbon dioxide. In J. Lenoble and J.F. Geleyn, editors, IRS 88: Current Problems in Atmospheric Radiation, 368-371. A. Deepak Hampton, VA.
- N. Jacquinet-Husson, N.A. Scott, A. Chedin, K. Garceran, R. Armante, A.A. Chursin, A. Barbe, M. Birk, L.R. Brown, C. Camy-Peyret, C. Claveau, C. Clerbaux, P.F. Coheur, V. Dana, L. Daumont, M.R. Debacker-Barilly, J.M. Flaud, A. Goldman, A. Hamdouni, M. Hess, D. Jacquemart, P. Kopke, J.Y. Mandin, S. Massie, S. Mikhailenko, V. Nemtchinov, A. Nikitin, D. Newnham, A. Perrin, V.I. Perevalov, L. Regalia-Jarlot, A. Rublev, F. Schreier, I. Schult, K.M. Smith, S.A. Tashkun, J.L. Teffo, R.A. Toth, V.I.G. Tyuterev, J. Vander Auwera, P. Varanasi, G. Wagner, 2005: The 2003 edition of the GEISA/IASI spectroscopic database. *J. Quant. Spectrosc. Radiat. Transfer*, **95**, 429-467.

- K.D., Klaes, Y., Buhler, H., Wilson., and F., Wollenweber, 2000: The EUMETSAT Polar System: mission and products. *Proceeding of the 2000 EUMETSAT Meteorological Satellite Data User's Conference*, Bologna, Italy, 29 May-2 June 2000.
- Robert Knuteson, CIMSS, personal communication.
- W.J, Lafferty, A.M. Solodov, A. Weber, W.B. Olson and J.-M. Hartmann, 1996: Infrared collision-induced absorption by N<sub>2</sub> near 4.3  $\mu$ m for atmospheric applications: measurements and empirical modelling. *Applied Optics*, **35**, 5911-5917.
- G. Masiello, G. Grieco, C. Serio, and V. Cuomo, 1996: Canopy emissivity characterization from hyper spectral infrared observations. *Proceeding of the 12<sup>th</sup> Conference on Atmospheric Radiation*, 9-14 July 2006, Madison., WI, USA.
- K. Masuda, T. Takashima and T. Takayama, 1988: Emissivity of pure sea waters for the model of sea surface in the infrared window regions. *Remote Sens. Environ.*, **24**, 313-329.
- M. Matricardi, F. Chevallier, G. Kelly and J.-N. Thepaut, 2004: "An improved general fast radiative transfer model for the assimilation of radiance observations". *Q. J. Roy. Meteorol. Soc.*, **130**, 153-173.
- V. Menoux, R. Le Doucen, C. Boulet, A. Roblin and A.M. Bouchardy, 1993: Collision induced absorption in the fundamental Band of N<sub>2</sub>. *Applied Optics*, **32**, 263-268.
- F. Miskolczi, R. Rizzi, R. Guzzi, M. Bonzagni, 1989: A new high resolution transmittance code and its application in the field of remote sensing. In: *IRS'88: Current Problems in Atmospheric Radiation*, A. Deepak Publishing, pp. 388-391.
- F. Miskolczi, M. Bonzagni, R. Guzzi, 1990: High Resolution Atmospheric Radiance-Transmittance Code (HARTCODE). *Meteorology and Environmental Sciences*, World Scientific Pub. Co., pp. 743-790.
- E.J., Mlawer, D.C. Tobin, and S.A. Clough, A Revised Perspective on the Water Vapor Continuum: The MT\_CKD Model, in preparation, 2004.
- F. Niro, K. Jucks and J.-M. Hartmann, 2005: Spectra calculations in central and wing regions of CO<sub>2</sub> IR bands. IV: software and database for the computation of atmospheric spectra. *Journal of Quantitative Spectroscopy and Radiative Transfer*, Volume 95, Issue 4, Pages 469-481
- F. Rabier, J. Thépaut and P. Courtier, 1998: Extended assimilation and forecast experiments with a four dimensional variational assimilation system. *Q.J.Roy. Meteor. Soc.*, **124**, 1861-1887.
- H.F. Revercomb, F.A. Best, R.G. Dedecker, R.P. Dirks, A. Herbsleb, R.O. Knuteson, J.F. Short, and W.L. Smith, 1993: Atmospheric Emitted Radiance Interferometer (AERI) for ARM. In *Fourth Symposium on Global Change Studies*, Anaheim, CA, January 17-22 1993, Published by the American Meteorological Society, Boston, Mass.
- C.P. Rinsland, J.S. Zander, J.S. Namkung, C.B. Farmer and R.H. Norton, 1989: Stratospheric infrared continuum absorption observed by the ATMOS instrument. *J. Geophys. Res.*, **94**, 16303-16322.
- R., Rodriguez, KW Jukus, N Lacome, G Blanquest, J Valrand, WA Traub, B Khalil, R LeDoucent, A Valentin, C Camy-Peyret, L Bonamy and JM Hartmann, 1999: Model, software and data base for computation of line mixing effects in infrared Q branches of atmospheric CO<sub>2</sub>. I. Symmetric isotopomers. *J. Quant. Spectrosc. Radiat. Transfer*, **61**, 153-184.
- L.S. Rothman, C.P. Rinsland, A. Goldman, S.T. Massie, D.P. Edwards, J.-M. Flaud, A. Perrin, C. Camy-Peyret, V. Dana, J.-Y. Mandin, J. Schroeder, A. McCann, R.R. Gamache, R.B. Watson,

K. Yoshino, K.V. Chance, K. W. Jucks, L.R. Brown, V. Nemtchinov, and P. Varanasi, 1998: The HITRAN molecular spectroscopic database and HAWKS (HITRAN Atmospheric Workstation): 1996 edition. *J. Quant. Spectrosc. Radiat. Transfer*, **60**, 665-710.

L.S. Rothman, A. Barbe, D. Chris Benner, L.R. Brown, C. Camy-Peyret, M.R. Carleer, K. Chance, C. Clerbaux, V. Dana, V.M. Devi, A. Fayt, J.-M. Flaud, R.R. Gamache, A. Goldman, D. Jacquemart, K.W. Jucks, W.J. Lafferty, J.-Y. Mandin, S.T. Massie, V. Nemtchinov, D.A. Newnham, A. Perrin, C.P. Rinsland, J. Schroeder, K.M. Smith, M.A.H. Smith, K. Tang, R.A. Toth, J. Vander Auwera, P. Varanasi, K. Yoshino, 2003: The HITRAN molecular spectroscopic database: edition of 2000 including updates through 2001. *J. Quant. Spectrosc. Radiat. Transfer*, **82**, pp.5-44.

L.S. Rothman, D. Jacquemart, A. Barbe, D. Chris Benner, M. Birk, L.R. Brown, M.R. Carleer, C. Chackerian Jr., K. Chance, L.H. Coudert, V. Dana, V.M. Devi, J.-M. Flaud, R.R. Gamache, A. Goldman, J.-M. Hartmann, K.W. Jucks, A.G. Maki, J.-Y. Mandin, S.T. Massie, J. Orphal, A. Perrin, C.P. Rinsland, M.A.H. Smith, J. Tennyson, R.N. Tolchenov, R.A. Toth, J. Vander Auwera, P. Varanasi, G. Wagner, 2005: The HITRAN 2004 molecular spectroscopic database. *J. Quant. Spectrosc. Radiat. Transfer*, **96**, pp.139-204.

W.L. Smith, H. E. Revercomb, H.B. Howell, and H.M. Wolf, 1983: HIS- A satellite instrument to observe temperature and moisture profiles with high resolution. In *Fifth Conference on Atmospheric Radiation*, American Meteorological Society, Boston.

G.M., Stokes and S.E., Schwartz, 1994: The Atmospheric Radiation Measurement (ARM) Program: programmatic background and design of the cloud and radiation test bed. *Bull. Am. Meteor. Soc.*, **75**, 1201-1221.

L.L. Strow, D.C. Tobin and S.E. Hannon, 1994: A compilation of First-Order Line-Mixing coefficients for CO<sub>2</sub> Q-branches. *J. Quant. Spectrosc. Radiat. Transfer*, **52**, 281.

J.P., Taylor, S.M. Newman, T.J. Hewison and A. McGrath, 2003: Water vapour line and continuum absorption in the thermal infrared-reconciling models and observations. *Q. J. Roy. Meteorol. Soc.*, **129**, 2949-2969.

F. Thibault, V. Menoux, R. Le Doucen, L. Rosenman, J.-M. Hartmann, and Ch. Boulet, 1996: Infrared collision-induced absorption by O<sub>2</sub> near 6.4 microns for atmospheric applications: measurements and empirical modeling, *Appl. Optics*, **35**, 5911-5917.

F. Thibault, V. Menoux, R. Le Doucen, L. Rosenmann, J.-M. Hartmann and Ch. Boulet, 1997: Infrared collision-induced absorption by O<sub>2</sub> near 6.4  $\mu$ m for atmospheric applications: measurements and empirical modelling. *Applied Optics*, **36**, 563-567.

Y.M. Timofeyev and M.V. Tonkov, 1978: Effect of the induced Oxygen absorption band on the transformation of radiation in the 6  $\mu$ m region of the Earth's atmosphere. *Atmos. Ocean Phys.*, **14**, 437-441.

R. A. Toth, 1998: Water vapour measurements between 590 and 2582 cm<sup>-1</sup>: Line Positions and Strengths. *J. Molecular Spectroscopy*, **190**, 379-396.